UAB
Universitat Autònoma de Barcelona

DEVELOPMENT OF NOVEL MATERIALS AND LOW-COST DEVICES FOR MECHANICAL ENERGY HARVESTING

Marcos Duque Duque

ADVERTIMENT. L'accés als continguts d'aquesta tesi doctoral i la seva utilització ha de respectar els drets de la persona autora. Pot ser utilitzada per a consulta o estudi personal, així com en activitats o materials d'investigació i docència en els termes establerts a l'art. 32 del Text Refós de la Llei de Propietat Intel·lectual (RDL 1/1996). Per altres utilitzacions es requereix l'autorització prèvia i expressa de la persona autora. En qualsevol cas, en la utilització dels seus continguts caldrà indicar de forma clara el nom i cognoms de la persona autora i el títol de la tesi doctoral. No s'autoritza la seva reproducció o altres formes d'explotació efectuades amb finalitats de lucre ni la seva comunicació pública des d'un lloc aliè al servei TDX. Tampoc s'autoritza la presentació del seu contingut en una finestra o marc aliè a TDX (framing). Aquesta reserva de drets afecta tant als continguts de la tesi com als seus resums i índexs.

ADVERTENCIA. El acceso a los contenidos de esta tesis doctoral y su utilización debe respetar los derechos de la persona autora. Puede ser utilizada para consulta o estudio personal, así como en actividades o materiales de investigación y docencia en los términos establecidos en el art. 32 del Texto Refundido de la Ley de Propiedad Intelectual (RDL 1/1996). Para otros usos se requiere la autorización previa y expresa de la persona autora. En cualquier caso, en la utilización de sus contenidos se deberá indicar de forma clara el nombre y apellidos de la persona autora y el título de la tesis doctoral. No se autoriza su reproducción u otras formas de explotación efectuadas con fines lucrativos ni su comunicación pública desde un sitio ajeno al servicio TDR. Tampoco se autoriza la presentación de su contenido en una ventana o marco ajeno a TDR (framing). Esta reserva de derechos afecta tanto al contenido de la tesis como a sus resúmenes e índices.

WARNING. The access to the contents of this doctoral thesis and its use must respect the rights of the author. It can be used for reference or private study, as well as research and learning activities or materials in the terms established by the 32nd article of the Spanish Consolidated Copyright Act (RDL 1/1996). Express and previous authorization of the author is required for any other uses. In any case, when using its content, full name of the author and title of the thesis must be clearly indicated. Reproduction or other forms of for profit use or public communication from outside TDX service is not allowed. Presentation of its content in a window or frame external to TDX (framing) is not authorized either. These rights affect both the content of the thesis and its abstracts and indexes.

Universitat Autònoma de Barcelona

Departamento de Ingeniería Electrónica

DEVELOPMENT OF NOVEL MATERIALS AND LOW-COST DEVICES FOR MECHANICAL ENERGY HARVESTING

Marcos Duque Duque

DIRECTOR

Gonzalo Murillo Rodríguez

TUTOR

Gabriel Abadal Berini

Memoria de Tesis en el programa de doctorado en

Ingeniería Electrónica y de Telecomunicación

Abril 2024

La presente tesis doctoral titulada **'Development of novel materials and low-cost devices for mechanical energy harvesting'** es presentada por Marcos Duque Duque como cumplimiento parcial de los requisitos para obtener el título de Doctor por la Universidad Autónoma de Barcelona en el Programa de doctorado en Ingeniería Electrónica y de Telecomunicación.

Esta tesis fue realizada en el Instituto de Microelectrónica de Barcelona (IMB-CNM, CSIC), bajo la supervisión del **Dr. Gonzalo Murillo Rodríguez** y tutelada por **Dr. Gabriel Abadal Berini**.

Con la aprobación de:

Dr. Gonzalo Murillo	Dr. Gabriel Abadal
(Director)	(Tutor)

Marcos Duque Duque

(Autor)

A mi hijo Julen.

TABLE OF CONTENTS

ABBREVIATIONS AND ACRONYMS 9
ABSTRACT 11
RESUMEN 13
1. INTRODUCTION 15
1.1 INTERNET OF THINGS 17
1.1.1 Evolution and Applications of the IoT 18
1.1.2 Development of the IoT 18
1.1.3 Challenges and Ethical Considerations 19
1.1.4 Future Trends and Research Directions 20
1.2 ENERGY HARVESTING 20
1.2.1 Benefits and challenges of EH in the IoT 21
1.3 PIEZOELECTRICITY 22
1.3.1 Piezoelectric effect 22
1.3.2 Properties and Piezoelectric Materials: 24
1.3.3 Structure Design 28
1.4 TRIBOELECTRICITY 30
1.4.1 Triboelectric effect 30
1.4.2 Quantification of triboelectrification 31
1.4.3 Triboelectric series 32
1.4.4 Operation principle 34
1.5 TECHNOLOGIES 35
1.5.1 Rapid prototyping techniques 35
1.5.2 Printed electronics 38
1.5.3 Microelectromechanical systems 39
1.5.4 Nanomaterials 40
1.6 STATE OF THE ART 41
1.6.1 EH with 3D printing 41
1.6.2 MEMS technology for EH 42
1.6.3 Triboelectricity 44
2. THESIS OBJECTIVES 49
2.1 Thesis Framework 52

3 RESULTS 53
3.1 Tapping-actuated triboelectric nanogenerator with surface charge density optimization for human motion energy harvesting 55
3.2 Low-cost manufacturing of monolithic resonant piezoelectric devices for energy harvesting using 3D printing 71
3.3 Piezoelectric MEMS resonator with magnetic tip mass for energy harvesting from ultra-low intensity magnetic field 95
3.4 Integration of ZnO nanostructures in MEMS devices using inkjet printing for energy harvesting 111
4 DISCUSSION 131
4.1 Triboelectric materials 133
4.2 Piezoelectric materials 134
4.3 Estimated cost of harvesting devices 137
5 CONCLUSIONS 139
6 ANNEX 143
6.1 Design and manufacture of measurement setups 145
6.1.1 Design and manufacture of a triboelectric material measurement setup 145
6.1.2 Design and manufacture of Helmholtz coils for MFs 147
6.2 Array of nickel mass cantilevers 149
6.2.1 Manufacturing process 149
6.2.2 Mask design 150
6.2.3 Fabrication process simulation 152
6.3 Patent: monolithic functional structures and method for their production 154
7 REFERENCES 199

ABBREVIATIONS AND ACRONYMS

AC	Alternate current
AM	Additive manufacturing
CAD	Computer-aided design
CMOS	Complementary metal-oxide-semiconductor
DS	Drop spacing
DRIE	Deep reactive ion etching
DUT	Device under test
EH	Energy harvesting
EM	Electromagnetic
FDM	Fused deposition modeling
FEM	Finite element modeling
HF	Hydrofluoric acid
IJP	Inkjet printing
IoT	Internet of things
ME	Magnetoelectric
MF	Magnetic field
MEMS	Microelectromechanical systems
NM	Nanomaterial
PE	Printed Electronics
PLA	Polylactic acid
PZT	Lead zirconate titanate
PVDF	Polyvinylidene fluoride

RPT	Rapid prototyping techniques
RF	Radiofrequency
TENG	Triboelectric nanogenerator
ZnO	Zinc oxide

ABSTRACT

The doctoral thesis addresses the critical challenge of the energy dependence of the Internet of Things (IoT). As it expands, its ability to improve efficiency, productivity and convenience in sectors such as industry, health, agriculture, and smart cities is undeniable. However, this growth has increased the demand for new energy sources to power the IoT wireless sensors, posing significant sustainability and energy efficiency challenges. In response to this problem, the research of the thesis focuses on developing innovative solutions to make IoT sensors energetically self-sufficient through the concept of "energy harvesting" (EH), which involves the capture and conversion of environmental energy into usable electricity. This approach is based on the use of piezoelectric and triboelectric materials to generate energy from mechanical vibrations, magnetic fields and human movement.

The thesis is divided into two main areas of research: triboelectric and piezoelectric materials. In the first case, a comprehensive research is being carried out on the principles of contact electrification to develop efficient energy collectors, capable of powering sensors with the simple pulse of the palm of the hand. On the other hand, in the field of piezoelectric materials, two different approaches are being explored. On the one hand, 3D printing is used to integrate piezoelectric materials into structures designed to capture vibrational energy, while on the other hand, the potential of MEMS devices (Microelectromechanical systems) for energy capture is investigated. Within the scope of MEMS, a study focused on the capture of energy from ultra-low-intensity magnetic fields is carried out. Furthermore, the possibility of combining MEMS technology with printed electronics, especially through the ink injection printing process, is being explored in order to merge these technologies and create innovative devices for collecting vibrational energy.

In addition to research, economic, environmental and sustainability considerations are addressed, with particular emphasis on the use of lead-free materials and the optimization of manufacturing processes through quick prototyping techniques. In short, the thesis offers a perspective on how to address the challenge of energy dependence in

the context of the IoT, proposing innovative solutions that promise to pave the way towards a more sustainable and energy efficient future.

RESUMEN

La tesis de doctorado aborda el desafío crítico de la dependencia energética de la Internet de las Cosas (IoT). A medida que se expande, su capacidad para mejorar la eficiencia, la productividad y la conveniencia en sectores como la industria, la salud, la agricultura y las ciudades inteligentes es innegable. Sin embargo, este crecimiento ha aumentado la demanda de nuevas fuentes de energía para alimentar los sensores inalámbricos de IoT, lo que plantea importantes desafíos en materia de sostenibilidad y eficiencia energética. En respuesta a este problema, la investigación de la tesis se centra en el desarrollo de soluciones innovadoras para hacer que los sensores IoT sean energéticamente autosuficientes a través del concepto de "recolección de energía" (EH), que implica la captura y conversión de la energía ambiental en electricidad usable. Este enfoque se basa en el uso de materiales piezoeléctricos y triboelétricos para generar energía a partir de vibraciones mecánicas, campos magnéticos y movimiento humano

La tesis se divide en dos áreas principales de investigación: los materiales triboeléctricos y los materiales piezoeléctricos. En el primer caso, se lleva a cabo una investigación exhaustiva sobre los principios de la electrificación por contacto para desarrollar recolectores de energía eficientes, capaces de alimentar sensores con la simple pulsación de la palma de la mano. Por otro lado, en el ámbito de los materiales piezoeléctricos, se exploran dos enfoques distintos. Por un lado, se utiliza la impresión 3D para integrar materiales piezoeléctricos en estructuras diseñadas para capturar energía vibracional, mientras que, por otro lado, se investiga el potencial de los dispositivos MEMS (Sistemas microelectromecánicos) para la captación de energía. Dentro del ámbito de los MEMS, se realiza un estudio centrado en la captación de energía a partir de campos magnéticos de ultra baja intensidad. Además, se explora la posibilidad de combinar la tecnología MEMS con la electrónica impresa, especialmente a través del proceso de impresión por inyección de tinta, con el fin de fusionar estas tecnologías y crear dispositivos innovadores de recolección de energía vibracional.

Además de la investigación, se abordan consideraciones económicas, medioambientales y de sostenibilidad, con un énfasis particular en el uso de materiales libres de plomo y en la optimización de los procesos de fabricación mediante técnicas de prototipado rápido.

En resumen, la tesis ofrece una perspectiva sobre cómo abordar el desafío de la dependencia energética en el contexto del IoT, proponiendo soluciones innovadoras que prometen allanar el camino hacia un futuro más sostenible y eficiente en términos energéticos.

1. INTRODUCTION

This chapter will introduce concepts, basic principles, and key definitions, which are essential for a deep understanding of the thesis topic. The necessary foundations will be laid here to enable us to understand the arguments and conclusions presented in this work.

1.1 INTERNET OF THINGS

In the last decade, the Internet of Things (IoT) has experienced rapid growth and has established itself as a disruptive technology with a significant impact in various fields. The IoT is a concept that refers to the interconnection of physical objects or people through multifunctional nodes via the internet, enabling the collection, exchange, and real-time analysis of data [1, 2].



Figure 1: *Illustration depicting the concept of the IoT, showing interconnected devices and data exchange over the internet.*

The possibility of connecting daily objects to the Internet has opened up new opportunities and challenges in terms of efficiency, convenience, security, and sustainability. Due to the rapid increase in smartphones and tablets in 2010, the number of devices connected to the internet exceeded the world's population for the first time in history, reaching an average of 1.84 internet-connected devices per person [3]. By 2030, more than 29.4 billion IoT devices are expected to be on the internet [4].

These objects, also known as smart devices or sensors, can range from household appliances and wearable devices to urban infrastructure and industrial systems. Since its

emergence, the IoT has evolved in various areas and has found applications in multiple sectors, such as computing, engineering, medicine, agriculture, and industry [5]. The advancement of IoT has been driven by the continuous development of key technologies such as wireless connectivity, embedded systems, artificial intelligence (AI), and the cloud. These advances have enabled the creation of robust and secure networks, as well as, the efficient processing and analysis of large volumes of data generated by connected devices.

The IoT has the potential to transform our lives by enabling automation, remote monitoring, and intelligent decision-making across a wide range of applications.

1.1.1 Evolution and Applications of the IoT

Since its emergence, the IoT has evolved in several areas and found applications in multiple sectors. In the household domain, smart devices enable home automation, energy monitoring, security, and user comfort. For instance, intelligent lighting and climate control systems can be automatically adjusted according to user preferences and needs.

In the industry, IoT has driven the Industry 4.0 revolution, where factories and production systems become more efficient, flexible, and interconnected. Sensors embedded in machines and equipment enable real-time monitoring of variables such as temperature, pressure, and humidity, which facilitates early detection of faults and optimizes production processes [6, 7]. In the healthcare field, IoT has led to the development of smart medical devices that enable remote patient monitoring, chronic disease tracking, and personalized medical care. These devices range from bracelets and smart watches that monitor physical activity to implantable devices that monitor vital signs and send alerts in case of abnormalities [8, 9]. In the urban environment, IoT has led to the creation of smart cities, where sensors and devices collect data to optimize traffic management, energy efficiency, and air quality [10–13].

1.1.2 Development of the IoT

The development of IoT has been driven by key advances in different technological areas. Firstly, advances in the miniaturization of electronic components, such as sensors and

actuators, have enabled the integration of smart functionalities into common objects. In addition, the development of high-speed wireless communication networks, such as 5G, has provided a robust infrastructure for connectivity and data transmission between devices [14, 15].

Another crucial factor in the development of IoT has been the increase in data storage and processing capacity through the cloud. The ability to store large amounts of information and access it from any location has driven the growth of the IoT and enabled the implementation of more complex applications.

1.1.3 Challenges and Ethical Considerations

Despite the benefits and advances provided by the IoT, a number of ethical challenges and considerations also arise. Data security and privacy are crucial aspects that must be tackled rigorously to prevent unauthorized access and misuse of personal information. Moreover, interoperability between different devices and systems remains a challenge, as the lack of common standards can make communication and integration of technologies difficult.

As the number of connected devices increases exponentially, the challenge of efficiently managing and managing large volumes of data generated by these devices also arises. Scalable data storage, processing, and analysis solutions are required to maximize the potential of the IoT [6].

One of the key constraints facing the deployment and widespread adoption of IoT is the reliance on conventional batteries to power connected devices. Batteries have limited capacity and require periodic replacement or recharging, which can be costly, inconvenient, and unsustainable in environments where devices are dispersed or difficult to access.

The issue of ethics is also relevant in the IoT. The misuse of personal data, automated decision-making, and possible excessive reliance on technology raise ethical questions that must be considered and regulated [16].

1.1.4 Future Trends and Research Directions

The field of IoT continues to evolve and presents several promising areas for research and development. Some of the future trends and directions include:

Edge computing is becoming increasingly relevant in reducing latency and relieving the burden on the cloud infrastructure. Distributed computing enables data processing on the devices themselves, which provides benefits in terms of response speed and efficiency in the use of network resources [17, 18].

The integration of artificial intelligence and machine learning techniques into the IoT enables the creation of autonomous and predictive systems. Intelligent analysis of data generated by connected devices can provide valuable information for decision-making and process optimization [19].

The IoT can play an important role in building sustainable cities and communities. Intelligent monitoring of energy resources, efficient transportation and intelligent waste management are areas that can benefit from IoT to greater efficiency and reduce environmental impact [13].

1.2 ENERGY HARVESTING

As global energy demand continues to increase and concerns about fossil fuel depletion and greenhouse gas emissions intensify, the need to find alternative, environmentally friendly energy sources has become more urgent than ever. In this context, Energy Harvesting (EH), also known as environmental energy collection, offers a promising solution to overcome battery dependence and extend the life of IoT devices. This technique consists of capturing and exploiting sources of energy present in the environment for their subsequent conversion into usable energy, generally in the form of electricity to power electronic devices. There are various fields of energy available to collect energy, which include radiation (light, solar, and electromagnetic (EM) radiation), thermal (temperature gradient), mechanics (potential, kinetics), chemistry (battery, fuel cell), nuclear, magnetic and electrical. Although among all these options, the most common are thermal, solar and vibrational.

Vibrational mechanical energy is a source of kinetic energy that is available virtually everywhere, such as in urban and industrial environments, but is often overlooked as an energy source that can be exploited. The main methods of collecting vibrational energy for its conversion into electrical energy are EM, electrostatic or piezoelectric. Piezoelectric energy harvesting (PEH) is one of the most promising technologies for leveraging vibrations or motion, in isolated applications where there are enough vibrations but lack access to energy sources.

Piezoelectric collectors are devices designed to transform mechanical energy intoo electrical energy using the piezoelectrical effect. This principle is based on the ability of some materials to generate an electric charge when they are subjected to mechanical stresses or deformations.

The piezoelectric effect occurs due to the asymmetrical distribution of charges in the crystalline structure of a material. When a mechanical stress is applied to the material, it causes a charge separation resulting in the generation of an electric potential. This load imbalance can be picked up by a conductor to generate an electric current.

Piezoelectric collectors are used in a wide variety of applications, from wireless sensors to medical devices and structural monitoring systems. For example, they are used in vibration and acceleration sensors that adhere to machines and structures to detect movements and changes in environmental conditions.

1.2.1 Benefits and challenges of EH in the IoT

One of the most significant benefits of EH in the IoT is the possibility of achieving energy autonomy for devices. By capturing and converting energy from the environment, devices can remain operational without the need to change batteries or connect them to external power sources. This is especially valuable in remote or difficult-to-reach applications. Using environmental energy sources such as sunlight, motion and vibrations also contributes to environmental sustainability by reducing reliance on disposable batteries and conventional energy sources. In addition, this can help reduce the carbon footprint and minimize resource waste [20–23].

EH-powered IoT devices tend to require much less maintenance compared to those that rely on conventional batteries. Eliminating the need to replace batteries often reduces operating costs and time spent managing and maintaining devices. It also allows for greater flexibility in the location and distribution of IoT devices. By eliminating the need for cable connections or voluminous batteries, devices can be located in hard-to-reach areas or incorporated into everyday objects more easily.

Although the EH is promising, efficiency in energy capture and conversion remains a challenge. The amount of energy that can be collected and stored may be limited in certain environments or situations, which could affect the continuous operation of IoT devices. Environmental energy sources, such as sunlight or motion, can be variable at different locations and times. This can affect the amount and consistency of energy that can be captured, which requires adaptive designs and systems.

Effective integration of EH into IoT devices requires careful design and component optimization. Devices must be energy-efficient and capable of managing energy effectively. Implementation may involve higher initial costs due to the need for specialized technologies and components. In addition, the complexity of energy capture, conversion and storage systems may require increased investment in research and development.

1.3 PIEZOELECTRICITY

1.3.1 Piezoelectric effect

The piezoelectric effect is a fundamental electromechanical phenomenon that was first discovered in 1880, thanks to studies by the brothers Pierre and Jacques Curie. It is manifested in certain materials that exhibit the ability to generate an electric charge when subjected to mechanical stresses or deformations. These materials, known as piezoelectric, comprise a variety of substances, including crystals such as quartz, barium titanium, topaz, Rochelle salt and tourmaline, as well as organic materials such as cane sugar [24, 25].

The piezoelectric effect can be classified into two main modalities: the direct effect and the reverse effect. In the direct effect, the application of a mechanical force or

deformation to the piezoelectric material results in the generation of an electric charge. In contrast, in the opposite effect, the application of an electrical field to piezoelectric material induces mechanical deformation.

Both effects have applications of great relevance in various technological areas. The direct effect is exploited in the manufacture of sensors and energy collector devices, allowing the conversion of mechanical energy into usable electric energy. On the other hand, the reverse effect is used in piezoelectric actuators for precision motion control in mechanical systems, as well as in micro and nanotechnology applications, where precision and miniaturization are essential.

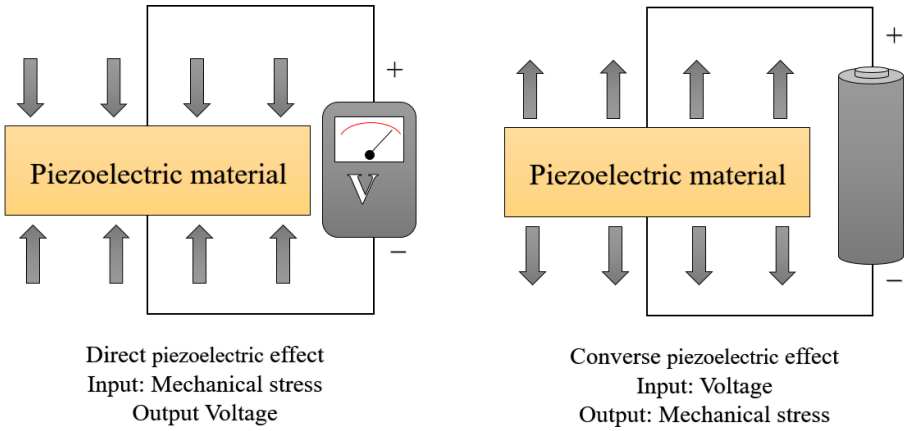


Figure 2: *Comparative illustration of the Direct and Inverse piezoelectric effects in piezoelectric materials.*

Constitutive Equations of the Piezoelectric Effect are shown below:

Direct Effect:

$$D = dT + \varepsilon E \quad (1)$$

Inverse Effect:

$$X = sT + dE \quad (2)$$

Where D is the electric displacement, d is the piezoelectric coefficient, T is the stress, ε is the material's permittivity, E is the electric field, X is the strain, and s is the mechanical strain.

1.3.2 Properties and Piezoelectric Materials:

1.3.2.1 Properties of Piezoelectric Materials

The choice of material for PHE plays a crucial role in its performance. The most important properties of piezoelectric materials for EH applications are as follows [25]:

Piezoelectric Coefficient (d)

This coefficient measures the relationship between the induced electric polarization (electric charge) and the mechanical stress applied to the material. It is an essential indicator of the material's ability to convert mechanical energy into electrical energy and vice versa. Piezoelectric materials typically have relatively high d values.

Voltage-Strain Coefficient (g)

This coefficient measures the relationship between the induced electric field and the mechanical stress applied to the material. It indicates the material's ability to generate an electric voltage when subjected to a mechanical force. Piezoelectric materials with a high g value are efficient for energy generation.

Electromechanical Coupling Factor (k)

This factor describes the efficiency with which a piezoelectric material can convert mechanical energy into electrical energy or vice versa. Higher values of k indicate higher efficiency in energy conversion. Piezoelectric ceramic materials typically have high k values.

Dielectric Constant (ε)

This property indicates the material's ability to store electric charge in response to an applied electric field. Piezoelectric materials with a high dielectric constant can store more charge, which is beneficial in energy storage applications.

Mechanical Quality Factor (Q):

This factor refers to the ratio of stored energy to dissipated energy in the material during a charging and discharging cycle. A higher Q value indicates lower energy loss and higher efficiency in energy conversion.

Stiffness and Density

These mechanical properties are important in applications where the stiffness and density of the material affect the device's performance. Piezoelectric materials must be stiff enough to withstand applied mechanical forces but also as lightweight as possible to avoid excessive loading on structures.

Thermal Stability

Thermal stability refers to the material's ability to maintain its piezoelectric properties over a wide range of temperatures. It is crucial in applications where the device will be exposed to different environmental conditions.

Chemical Resistance

The chemical resistance of the material is important in environments where it may be exposed to corrosive substances or hostile conditions.

Resonance Frequency

Indicates the frequency at which the piezoelectric material will resonate most efficiently. This is relevant in energy generation and sensor applications where maximum response at a specific frequency is desired.

1.3.2.2 Piezoelectric Materials

Each piezoelectric material has its own advantages and disadvantages in terms of these properties, so the selection is based on the needs and constraints of the design [26, 27].

They are classified into six main categories:

Ceramics

Lead zirconate titanate (PZT) is a very common material in piezoelectric ceramics. The PZT has a higher performance compared to the rest of the piezoelectric materials. Its high manufacturability enables large-scale production with different dimensions and shapes relatively easily and at a reasonable cost.

Polymers

Polyvinylidene fluoride (PVDF) and copolymers of Polyvinylidene fluoride and trifluoroethylene (P(VDF-TrFE)) are the most popular piezoelectric polymer materials. Unlike ceramics, they provide lower piezoelectric coefficients, but polymers offer greater mechanical flexibility, lower stiffness, and higher chemical resistance, preventing fatigue and increasing the device's lifespan.

Lead-Free Materials

The search for lead-free piezoelectric materials has gained increasing importance in recent decades due to environmental and public health concerns associated with lead. Although traditional materials like PZT have been widely used in piezoelectric applications, their lead content makes them less desirable from an environmental perspective. In response to this concern, research and development of new piezoelectric materials have intensified.

These lead-free materials are classified into organic and inorganic categories. Organic materials include PVDF and copolymers. On the other hand, inorganic materials are divided into various families, such as tungsten bronze, aurivillius, and perovskite. These materials show promising potential to replace traditional materials in piezoelectric applications, thus mitigating issues associated with lead content.

Despite lead-free materials beginning to show some advantages, overall, their properties remain inferior to those of PZT ceramics, such as lower piezoelectric properties, lower thermal stability, and processing difficulties, among others.

Piezoelectric Materials

In recent years, interest in nanostructures and piezoelectric nanomaterials (NMs) has increased. Among them, zinc oxide (ZnO) stands out as a characteristic example. This compound, a natural metal oxide, is widely available, low-cost, chemically stable in atmospheric environments, and considered safe from a biological perspective. ZnO is not ferroelectric, and nanostructures can be formed relatively easily on various flexible and rigid substrates at low temperatures without the need for a polarization process.

Single crystals

Single crystals exhibit a continuous and uninterrupted crystalline structure in their network, giving them exceptional piezoelectric and dielectric properties compared to bulk materials due to the absence of defects at grain boundaries and the presence of inherent anisotropy. However, they are limited by their low Curie temperature and phase transition temperature, as well as their weaker coercive field and inferior quality factor. Additionally, maintaining polarization requires the application of an additional electric field.

Composites

Composites can combine the advantages of different materials but have more complex processing requirements. Overall, each material has its own strengths and weaknesses and is suitable for specific applications.

1.3.2.3 Material Orientation

The orientation of piezoelectric materials is a crucial factor that influences their performance in specific applications. The direction in which stress or electric field is applied relative to the crystal axes of a piezoelectric material can determine its response and piezoelectric properties. These orientations are especially relevant in piezoelectric devices, such as energy harvesters, sensors, and actuators, where choosing the appropriate orientation can optimize device performance.

According to the standard notation in piezoelectricity by IEEE [28], numbers 1, 2, and 3 are defined to denote the X, Y, and Z axes, respectively, and numbers 4, 5, and 6 for the rotation directions around X, Y, and Z axes, respectively.

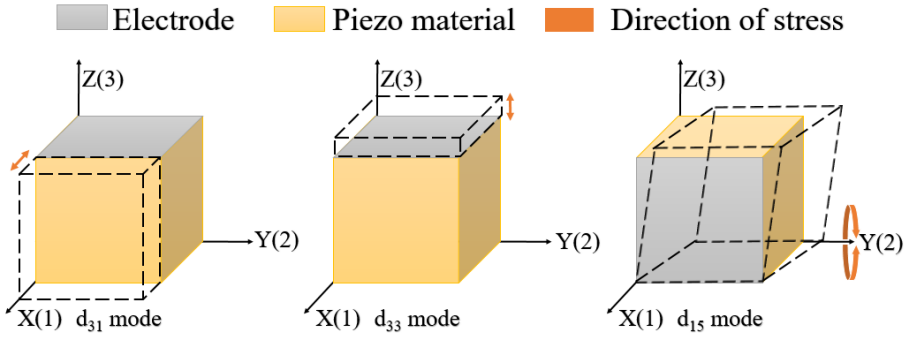


Figure 3: *Most Common Orientations for Piezoelectric Materials in EH: d_{31} Mode, d_{33} Mode, and d_{15} Mode.*

The piezoelectric coefficient d is characterized by two subscripts, i and p, where i denotes the direction of the electric field, and p signifies the orientation of stress. Herein lies a general description of the most common orientations in piezoelectric materials [29]:

d_{31} Mode

In this orientation, stress is applied in a direction perpendicular to the third crystal axis, generating tension in the direction of the first crystal axis. This is used in applications where high output current is needed.

d_{33} Mode

In this orientation, stress or electric field is applied in the direction of the material's principal third crystal axis. It is commonly used in applications requiring high output voltage, as this orientation produces the highest piezoelectric strain.

d_{15} Mode

It is a shear or bending mode used when high deformation in piezoelectric materials is required. The interest in mode d_{15} lies in the fact that, usually, in materials like PZT, the piezoelectric coefficient d_{15} is higher than d_{33} and d_{31}. However, manufacturing a device in mode d_{15} presents a challenge, as electrodes do not capture charges easily. This approach is frequently employed in applications requiring high energy conversion efficiency [30].

1.3.3 Structure Design

There are many structural configurations available for PEH devices, with the cantilever, circular diaphragm, cymbal, and stacked piezoelectric configurations being the most common, each with its own characteristics and advantages [31, 32].

Cantilever

The cantilever structure, a type of beam fixed at one end and extending outward with a piezoelectric material placed on top, is the most widely used due to its simple structural geometry and its ability to generate the maximum amount of deformation for a given amount of mechanical vibration. When subjected to vibrations or bending due to external forces, the cantilever bends, generating tension and compression in the piezoelectric material. Cantilever designs can be unimorph (with a single piezoelectric layer) or

bimorph (with two piezoelectric layers). The bimorph structure is preferred in PEH devices because it increases electrical energy production without significantly altering the size of the device. The cantilever design offers notable advantages in terms of simplicity and reduced costs, making it especially suitable for applications involving low to moderate frequency vibrations. Additionally, its ease of fabrication and ability to be miniaturized make it an attractive option. However, it has limitations in terms of efficiency in high-frequency applications.

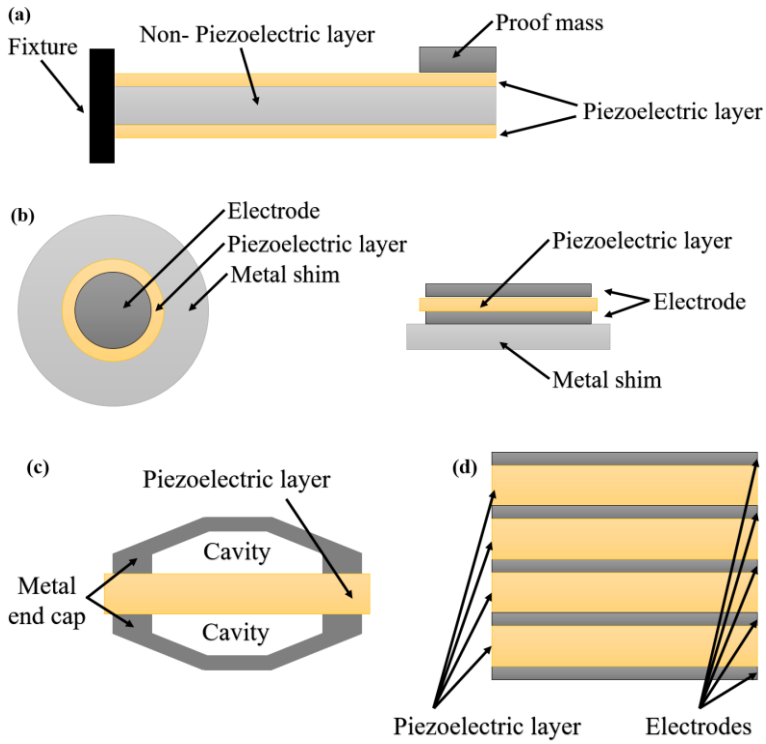


Figure 4: *Common Structures for Piezoelectric EH: (a) Cantilever, (b) Circular Diaphragm, (c) Cymbal, and (d) Piezoelectric Transducer Stack.*

Circular Diaphragm

These transducers have a thin disk-shaped structure connected to a clamping ring at the edges. They often feature additional mass in the center to enhance performance in low-frequency operations and energy generation. They can be used to operate in pressure mode. The diaphragm-like structure facilitates the capture of energy from slowly varying pressure fields, periodic acoustic waves, and mechanical vibrations. In contrast to the cantilever structure, this configuration is notably stiffer, resulting in a higher resonance frequency in vibration operation mode.

Cymbal

Cymbal devices have a shape similar to a cymbal or musical cymbal. They consist of a configuration where a layer of piezoelectric material is sandwiched between two metallic layers, forming a conical structure. When a force or vibration is applied to the cymbal structure, the deformation of the conical structure causes tension and compression in the piezoelectric material. Cymbal devices stand out for their higher efficiency in energy capture, especially in high-frequency applications, their ability to adapt to various vibration frequencies through design adjustments, and their greater robustness and durability. They are useful in applications involving higher impact forces, as they can amplify tension and generate a higher piezoelectric charge. However, these advantages come with challenges, such as increased complexity and manufacturing costs, as well as the potential for a larger size due to their conical structure.

Stacked Piezoelectric Transducers

These devices consist of multiple piezoelectric layers stacked on top of each other, with the polarization direction aligned with the applied force. They are used in applications that require high pressure. They offer several significant advantages, such as higher energy generation capacity due to their layered design, resistance to high pressures, durability in adverse environments, and the ability to control polarization for precise response.

The choice of piezoelectric transducer shape depends on the specific needs of the application and operating conditions, such as vibration frequency, magnitude of the applied force, and available space. Each transducer shape has its own advantages and limitations in terms of efficiency and energy generation capacity.

1.4 TRIBOELECTRICITY

1.4.1 Triboelectric effect

Triboelectricity, a phenomenon recognized and studied for millennia, refers to the electrification induced by contact and friction between two different materials. Although ancient, its underlying mechanism remains a subject of research and discussion,

highlighting its continued relevance in modern science and technology. This phenomenon, derived from the Greek word "tribo" meaning rubbing and "electron" in reference to electric charge, has intrigued scientists and technologists throughout history.

Since ancient times, the interaction of diverse materials upon contact and separation has been observed, generating a transfer of electric charges due to the breaking of chemical bonds on their surfaces, resulting in the accumulation of a positive charge on one material and a negative charge on the other. Despite its long history, the triboelectric effect remains the subject of active research today. Comprehensive studies are being conducted to understand in detail the underlying mechanisms of triboelectrification, as well as to explore its practical applications in areas such as energy generation, force detection, and the creation of autonomous sensors.

This phenomenon presents challenges and risks in daily life, industrial manufacturing, and transportation. For example, electrostatic charges can interfere with radio frequency communication in aircraft or even cause explosions and ignite flammable vapors [33, 34]. However, more recently, it has been discovered that triboelectricity can be harnessed positively and has begun to be used to convert mechanical energy into electrical energy in self-powered mechanical sensors.

1.4.2 Quantification of triboelectrification

Triboelectric quantification refers to the process of measuring and precisely expressing the amount of electric charge generated through the phenomenon of triboelectrification. This process is essential for understanding and applying triboelectricity in various applications and for classifying materials in a triboelectric series.

Triboelectric quantification is not only important from a scientific perspective but also has significant practical applications. Understanding how electric charges are generated and accumulated in materials enables the development of technologies that harness this phenomenon for mechanical-to-electrical energy generation, the creation of autonomous sensors, and force detection at the microscopic level. Additionally, precise

quantification of triboelectrification can also have implications for risk mitigation, such as static charge buildup in sensitive environments [35, 36].

One approach to quantifying triboelectrification is through advanced experimental methods such as atomic force microscopy (AFM) and scanning Kelvin probe microscopy (SKPM). These methods allow for the in-situ observation and measurement of electric charges generated on material surfaces during the friction and separation processes. The combination of AFM and SKPM has been particularly effective in investigating triboelectric charge transfer at the nanoscale [37–39]. These approaches enable not only the visualization of charge accumulation and saturation on the surface but also the quantification of key parameters such as surface charge density before and after the triboelectric process, as well as the electric field generated near the surface.

1.4.3 Triboelectric series

The triboelectric series categorizes materials based on their ability to produce electric charges through triboelectricity. Those at the top exhibit a higher tendency to acquire positive charges, while those at the bottom tend to acquire negative charges more easily. Over time, this series has undergone changes and has been the subject of continuous research

Historically, triboelectric series were based on qualitative data. However, in 2019, a method was developed that allows for the quantification of the triboelectric charge density of different materials based on their triboelectrification [40]. It operates using liquid mercury as a reference and is operated by coupling contact electrification and electrostatic induction. Once a material comes into contact with mercury, the charge density values are recorded. Thanks to this method, a more accurate and reliable triboelectric series has been constructed, taking into account the measured charge density after the triboelectrification process.

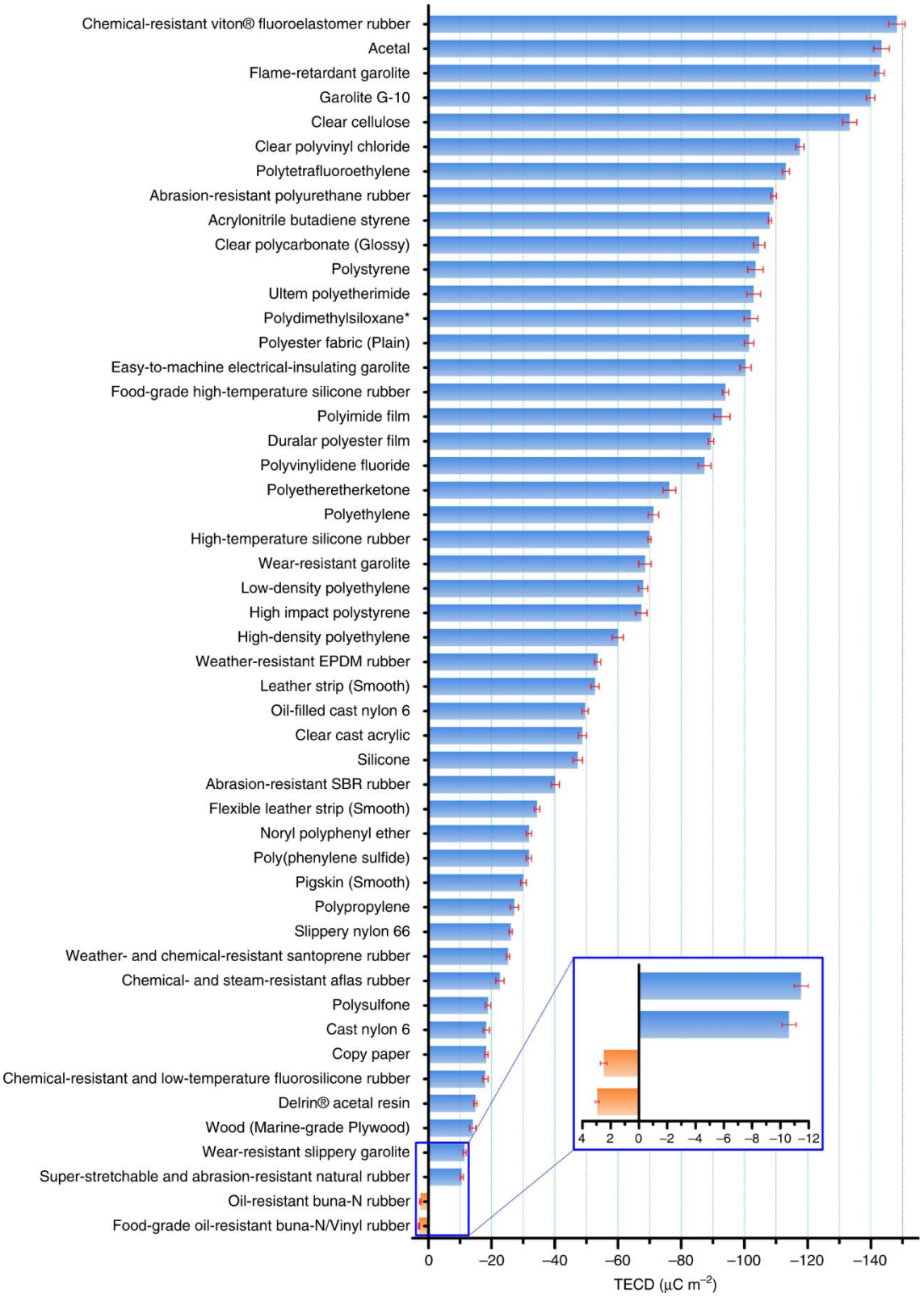


Figure 5: *The quantified triboelectric series. Source [40].*

1.4.4 Operation principle

Despite its long history, triboelectricity was not widely used until 2012, when the first Triboelectric Nanogenerator (TENG) was developed [41]. Since then, different types of TENG have been invented and have been categorized into four fundamental operating mode [42]:

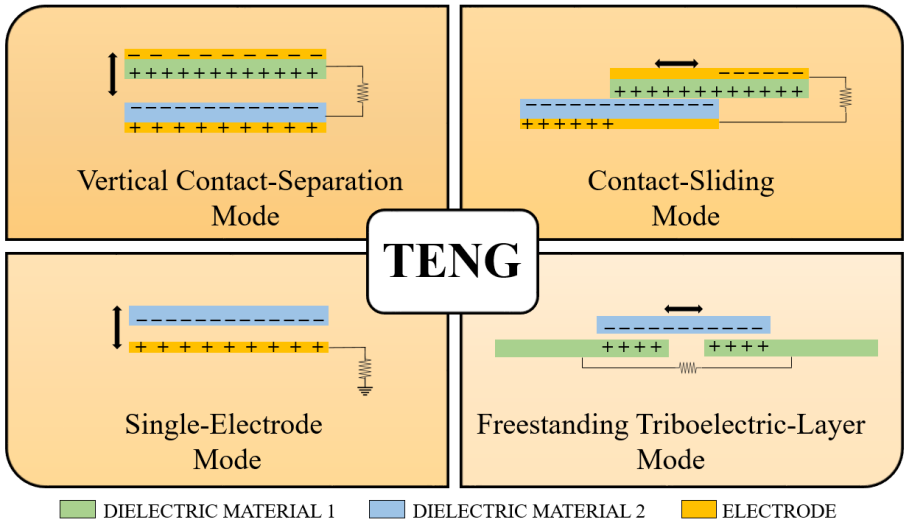


Figure 6: *Schematic of the four fundamental operating modes of TENGs.*

Vertical Contact-Separation Mode

Two electrodes are deposited on the upper and lower surfaces of two different dielectric films. Opposite charge surfaces are formed when the two dielectric films come into physical contact. A potential fall occurs when an external force causes the two surfaces to separate. To balance the electrostatic field, the free electrons in one electrode would flow to the other electrode if the two electrodes were electrically connected by a charge. The triboelectric charge generated by the potential disappears when the gap is closed and the electrons return to flow.

Lateral Sliding Mode

The initial structure is equal to that of the vertical contact separation mode. Triboelectric charges occur on both surfaces when two dielectric films come into contact due to a relative slide parallel to the surface. Along the sliding direction, a lateral polarization is added, causing electrons to flow from the upper and lower electrodes to completely balance the field created by triboelectric charges. A periodic slide produces an alternating

current output. This is the sliding TENG mode. The slide can be flat, disk rotation or cylindrical.

Single-Electrode Mode

There are situations where the object that forms part of the TENG cannot electrically connect to the charge because it is a moving object. To obtain energy in this case, a single TENG electrode is inserted, with the electrodes at the bottom of the TENG connected to the ground. If the TENG is small, a separation of the upper object from the lower object would change the local distribution of the electrical field, so there are exchanges of electrons between the lower electrode and the ground to maintain the potential change of the electrodes. This energy capture technique can be used in vertical contact-separation or Lateral Sliding Mode.

Freestanding Triboelectric-Layer Mode

Due to contact with air or another object, a moving object is naturally loaded. Because the load density reaches its peak while the loads remain on the surface for hours, contact or friction is not necessary. If we place a pair of symmetrical electrodes underneath a dielectric layer and the size of the electrons and the distances between them are of the same order as the dimension of the moving object, the approximation of the object to and/or the separation of electrons creates an asymmetric charge distribution in the medium, which causes electrons to flow between the two electrons in order to balance the local potential distribution. Energy is produced when electrons move between electrodes. In rotation mode, the moving object does not have to directly touch the upper dielectric layer of the electrodes, allowing free rotation without direct mechanical contact, which significantly reduces surface wear.

1.5 TECHNOLOGIES

1.5.1 Rapid prototyping techniques

Rapid prototyping techniques (RPTs) is an essential methodology in the fields of engineering and industrial design that has revolutionized the way we conceive, develop, and refine products and systems. This discipline has radically transformed the product development cycle by offering an efficient and agile way to create functional prototypes

and conceptual models. The primary goal of RPT is to enable designers and developers to experiment, evaluate, and refine their ideas quickly and cost-effectively before proceeding to mass production.

Historically, prototyping used to be a laborious and expensive process involving manual fabrication of scale models and custom component construction. However, with the advent of modern technology, RPT has emerged as a disruptive approach that leverages advanced manufacturing technologies such as milling, laser cutting, blade cutting, hot pressing, and 3D printing to significantly accelerate the process.

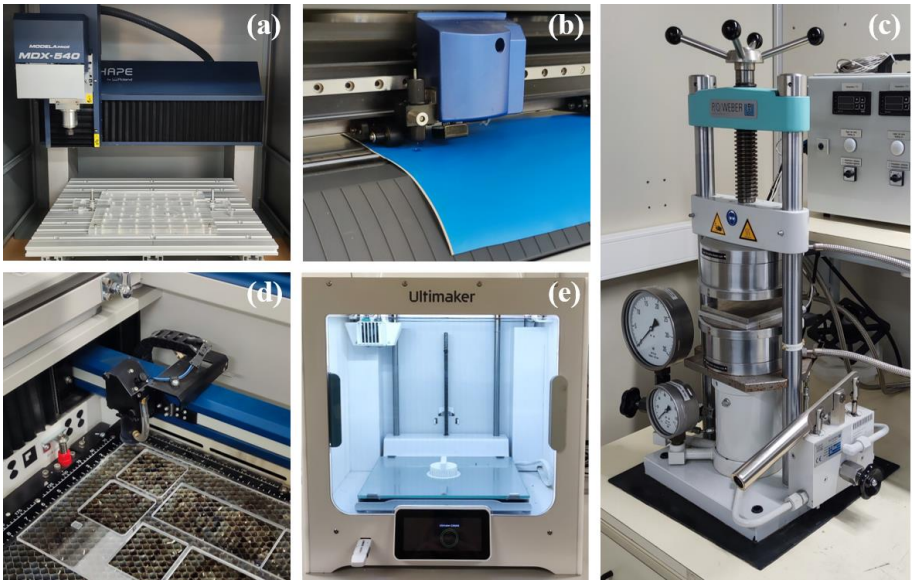


Figure 7: *RPTs: (a) Milling, (b) Blade Cutting, (c) Hot Pressing, (d) Laser Cutting and (e)3D Printing.*

RPT has become a key catalyst for innovation in a wide range of industries, from automotive and aerospace to consumer electronics and healthcare. It allows designers and developers to quickly test ideas, identify potential issues, and iteratively adjust designs. This constant and rapid iteration not only shortens development times but also improves the quality and effectiveness of the final products.

Below are some of the key techniques used in RPT:

Milling

Milling has been a fundamental technique in prototyping and functional part production for decades. Using Computer Numerical Control (CNC) machines, this technique allows for the removal of material from a solid piece, shaping precise and detailed components.

Milling is widely used in the aerospace, automotive, and medical industries for the creation of high-precision prototypes.

Laser Cutting

Laser cutting is another technology that has changed the face of RPT. It utilizes a high-intensity laser beam to cut and engrave materials with astonishing precision. From metal sheets to acrylic and wood, laser cutting is versatile and enables the creation of detailed prototypes and custom parts in a wide variety of materials. Additionally, it has become an essential tool in the fashion and jewelry industries, as well as in electronic device manufacturing.

Blade Cutting

Blade cutting is a technique that uses sharp blades to cut and shape flexible materials such as fabric, paper, and cardboard. It is particularly valuable in prototyping textile products and packaging. The precision and speed of this technique make it an effective choice for prototyping garments, patterns, and custom packaging.

Hot Pressing

Hot pressing is a method that involves the application of heat and pressure to bond thermoplastic and thermoset materials. This technique is crucial in prototyping composite products, such as carbon fiber composites in the aerospace industry or fiberglass-reinforced plastic components in the automotive industry.

3D Printing

3D printing is perhaps the most revolutionary technology in the field of RPT. Using a variety of materials, from plastics to metals and ceramics, 3D printing allows for the creation of three-dimensional objects layer by layer, from digital designs. This technique has democratized manufacturing, enabling companies and individuals to create prototypes quickly and affordably. Additionally, it has been applied in medicine to print customized prosthetics and in the aerospace industry to produce lightweight and complex components.

1.5.2 Printed electronics

The concept of Printed Electronics (PE) is not new; it has been in development since the 1940s. However, in recent decades, it has experienced exponential growth thanks to significant advances in conductive materials, printing techniques, and circuit design [43].

PE is a revolutionary branch of technology that has redefined the way we conceive and manufacture electronic devices. Representing a convergence of traditional electronics and printing techniques, PE has emerged as a powerful discipline with applications ranging from consumer electronics to healthcare and renewable energy. At its core, PE is divided into two fundamental groups: analog printing and digital printing, each with its own characteristics and unique applications.

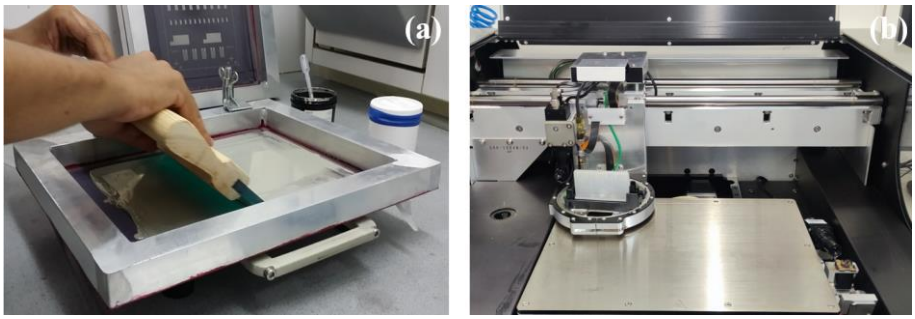


Figure 8: *Examples of PE: (a) Analog (SP) and (b) Digital (IJP).*

Analog Printing

Analog printing in PE encompasses technologies that rely on the transfer of conductive ink or semiconductor materials through a physical template, such as a mesh or a roller, onto a substrate. Examples of these techniques include screen printing (SP), flexography, offset printing, and gravure printing [44, 45]. Analog printing is highly efficient and scalable for the mass production of electronic devices. It is used in the manufacturing of solar panels, printed circuits, and high-volume electronic components.

Digital Printing

Digital printing in PE is an approach that utilizes digitally controlled material deposition techniques through patterns created by a computer to manufacture electronic components on a wide variety of substrates. There are several digital printing techniques, each tailored for different applications and needs. Inkjet printing (IJP) is one of the most common, versatile, and widely used [46, 47]. Digital printing enables the manufacturing

of customized and flexible electronic devices with exceptional precision, making it ideal for the production of sensors, electronic tags, flexible displays, and other electronic devices that require customization and adaptability [48–51].

1.5.3 Microelectromechanical systems

Microelectromechanical systems (MEMS) are a technique for producing structures and devices of microscopic size. In Europe, they are sometimes known as microsystem technology (MST), while in Asia, they are called micromachines [52–54]. In its development, standard integrated circuit (IC) microelectronic procedures such as oxidation, ion diffusion and doping implantation, rotating coating, chemical vapor deposition (CVD), physical vapor deposition, and epitaxy are used. It is easy to incorporate into complex systems as it is manufactured with standard semiconductor processing techniques and is Complementary metal–oxide–semiconductor (CMOS) compatible.

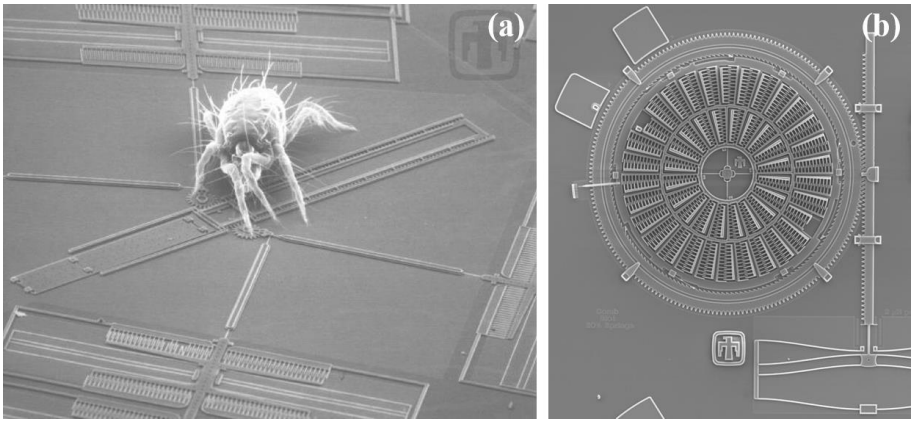


Figure 9: *Examples of MEMS (a) Spider mite on mirror assembly. (b) General view of a torsional ratcheting actuator. Source* [*55*].

MEMS covers a wide range of technologies, such as actuators, sensors and passive devices [*56*]. For various applications in RF electronics and communications, passive components such as filters and resonators are crucial [*57–59*]. MEMS sensors are crucial parts of a wide range of applications, from medical and portable devices to inertial navigation and environmental surveillance systems, as these small devices leverage their ability to detect and quantify changes in their environment [*60–62*]. MEMS actuators are essential in applications that require precise micromovements, such as ink injection

printing, optical device production and micromotor technology, as they convert electrical impulses into mechanical motion [*63*, *64*].

The range and diversity of MEMS applications are unparalleled. In the automotive sector, they are used in vehicle control systems, including airbags and anti-lock brake systems [65]. Drug delivery devices, biosensors and other diagnostic equipment are heavily dependent on MEMS [66]. They are used in monitoring the structure and state of the environment, as well as in aviation navigation and control systems [67]. MEMS have proven to be adaptable and effective instruments for EH in the field of energy use. MEMS sensors, for example, are ideal for monitoring dynamic environments and infrastructures, such as the automotive sector, as they can transform mechanical vibrations into electricity [68, 69].

1.5.4 Nanomaterials

Nanotechnology is a research area that enables the production of materials, including particulate materials, with at least one dimension smaller than 100 nanometers (nm). These NMs, including nanoparticles (NPs), exhibit unique properties due to their reduced size, which affects their chemical, electrical, mechanical, and optical characteristics. NMs have applications in various areas, from water treatment to medical diagnostics. Various production methods are employed, such as condensation, attrition, chemical precipitation, and ion implantation [70].

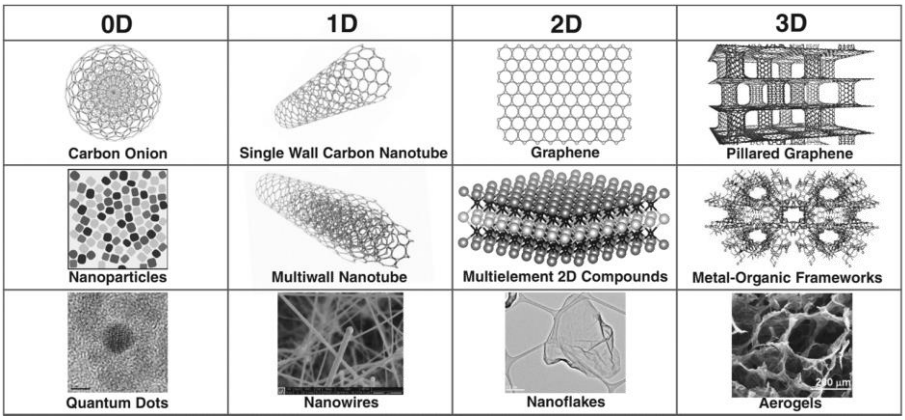


Figure 10: Illustration of Chemical, Structural, and Morphological Diversity in Nanoscale Building Blocks for Next-Generation Energy Storage Devices. Source [*71*].

NMs can be classified into various categories based on their dimensional characteristics.

Zero-Dimensional NMs (0D)

Zero-dimensional NMs are characterized by having all three dimensions in the nanometer range. They possess a well-defined and confined structure. A common example is NPs, often referred to as quantum dots. These materials exhibit quantum confinement effects, leading to unique optical, electronic, and magnetic properties.

One-Dimensional NMs (1D)

One-dimensional NMs are characterized by having one dimension in the nanometer range, while the other two dimensions are significantly larger. NWs and nanotubes are typical examples of 1D NMs.

Two-Dimensional NMs (2D)

Two-dimensional NMs are characterized by having two dimensions in the nanometer range and one significantly larger dimension. Graphene is one of the most well known 2D NMs.

Three-Dimensional NMs (3D)

Although the term "NMs" generally refers to materials with at least one dimension in the nanometer range, some complex structures exhibit three-dimensional nanoscale characteristics. These 3D NMs may include metal-organic frameworks (MOFs) and aerogels, which offer advantages in applications such as catalysis and energy storage.

1.6 STATE OF THE ART

1.6.1 EH with 3D printing

In most cases of 3D printing applications in the field of EH, this technology is primarily used to manufacture support structures instead of the devices themselves. The literature showcases a wide range of examples in various domains. For instance, in wind EH, the generator blades are 3D printed to rotate a magnet inside a coil and generate energy [72]. Similarly, 3D printed structures have been designed for gripper sensing, allowing a three-finger gripper to register the force applied when gripping an object and precisely adjust the exerted pressure based on the measured data [73]. In this latter case, PVDF is

used as the piezoelectric material and subsequently assembled alongside the printed parts.

Another notable example includes the creation of a PLA-printed resonator, to which a ferroelectric film is subsequently attached between the cantilever base and the structure's mass, aiming to harvest energy from vibrations [74].

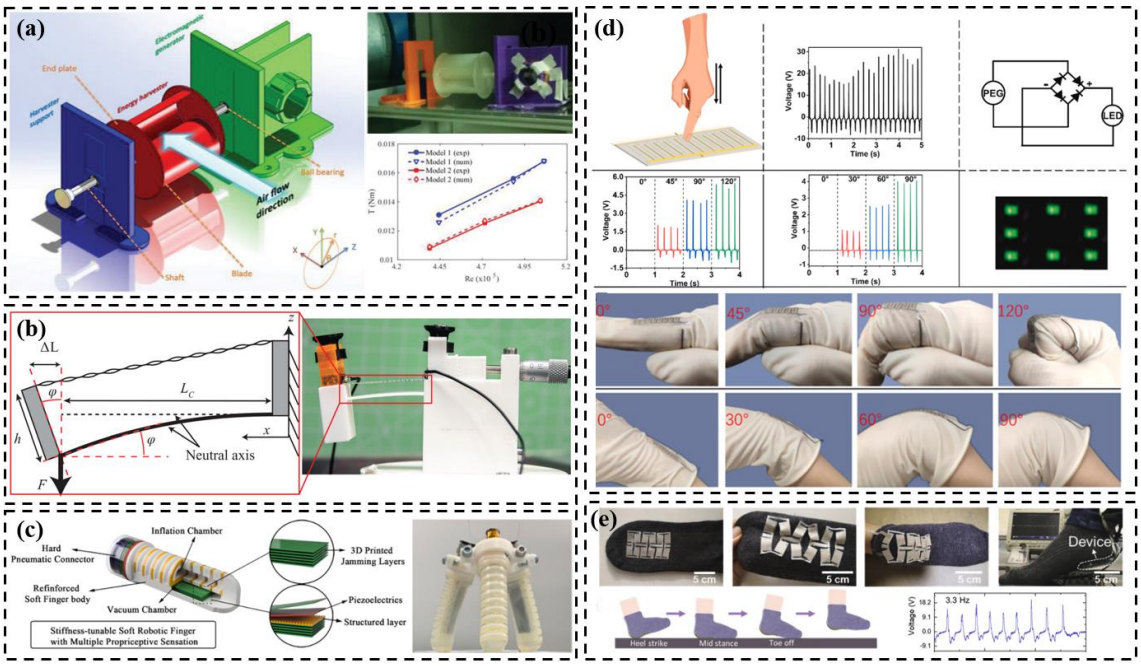


Figure 11: *Examples of applications utilizing 3D printing to create structures (a-c) [72–74], as well as the use of 3D printing to manufacture the piezoelectric material itself (d-e) [75, 76].*

Moreover, instances have been identified where the 3D printed material constitutes the generator itself, such as in the case of a material that, when impacted by a hammer, generates energy using PZT as the piezoelectric material [*77*]. In situations where the printed materials are lead-free, they typically serve as sensory components that must be subsequently integrated into other structures to fulfill their function in specific applications, such as foot pressure sensors or finger and hand motion sensors [*75*, *76*].

1.6.2 MEMS technology for EH

Various sources in the literature discuss EH and piezoelectric devices utilizing MEMS technology. For example, the use of PDMS as the piezoelectric material in a zigzag-shaped resonator has been explored, strategically designed to reduce its resonant frequency to ultra-low levels of 3 and 23 Hz, generating a significant power of 52 pW [78]. Similarly, a

spiral-shaped resonator device with PZT as the piezoelectric material has been studied, achieving a maximum output power of 23.3 nW through a five-turn spiral, excited at an acceleration of 0.25 G and a resonance frequency of 68 Hz [79]. Another example involves a microcantilever utilizing a junction between a bulk PZT wafer and phosphor bronze, created using MEMS technology. This generator has a resonance frequency of 100.8 Hz and achieves an output power of 13.5 µW under a 0.5 G acceleration [80].

Furthermore, a process has been described for manufacturing PZT-based MEMS energy harvesters on silicon and stainless steel substrates. The aerosol deposition method is employed to deposit PZT layers, allowing the creation of devices capable of generating a maximum power of 21 µW (on a silicon substrate) and 34 µW (on a stainless steel substrate), operating at vibration frequencies of 215 Hz and 202 Hz, respectively, with an acceleration of 1.5 G [81]. Additionally, a piezoelectric S-shaped microcantilever designed to operate at low frequencies has been introduced. This device employs the piezoelectric material PZT and managed to generate 1.117 nW at a frequency of 27.4 Hz [82].

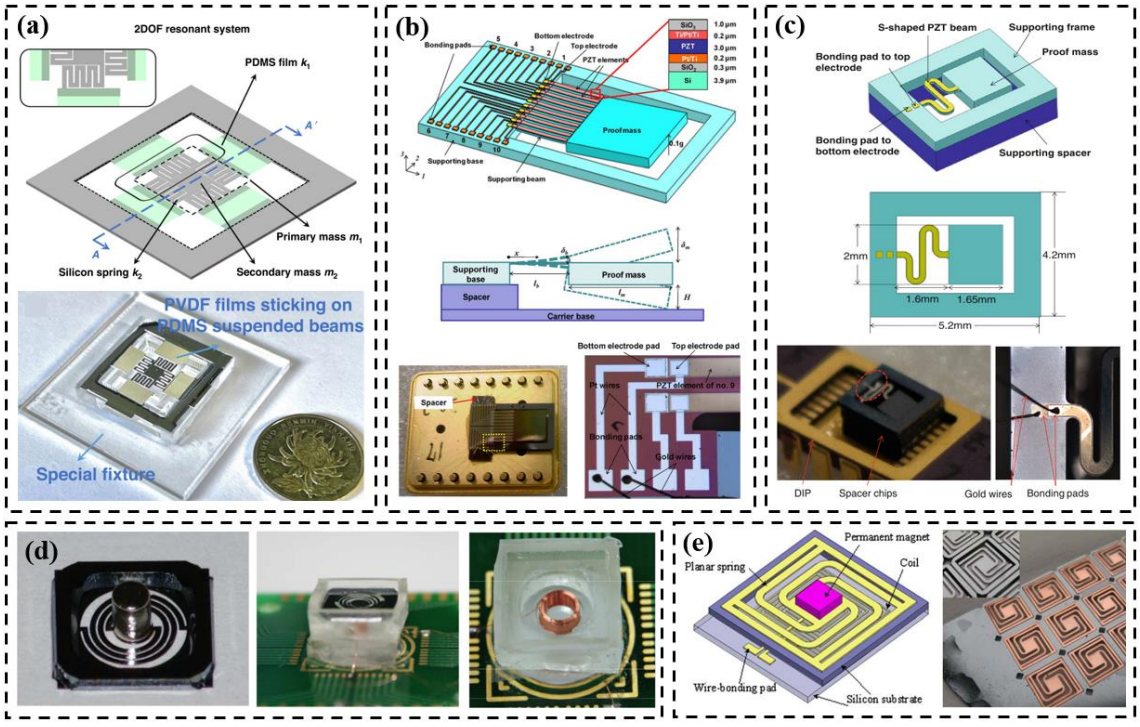


Figure 12: *Examples of EH devices (a-c) using MEMS technology through piezoelectric materials for use in vibrations [78, 82, 83] and (d-e) MEMS technologies through coils and magnets for magnetic fields [84, 85].*

On the other hand, a low-resonance-frequency energy harvester with a bandwidth of up to 17 Hz has been developed using a metal cap and PZT as the material, achieving power

outputs ranging from 19.4 nW to 51.3 nW in a frequency range from 30 Hz to 47 Hz, with a 1.0 G acceleration [*83*]. Furthermore, a piezoelectric MEMS energy harvester employing an intermediate layer of $PbTiO_3$ between thin films of ZrO_2 and PZT has been fabricated, reaching a resonance frequency of 528 Hz and producing electrical power of 1.1 µW with a 0.39 G acceleration [*86*].

In some cases, instead of using piezoelectric MEMS devices, MEMS technology along with coils is employed for EH, harnessing magnetic fields (MF) generated by accelerations. A notable example is a device that managed to generate an output power of 115.1 µW and a charging voltage of 68.2 mV with a load resistance of 18.1 Ω from a 54 Hz vibration with a 0.57 G acceleration [*84*]. Conversely, an optimized EM vibration energy harvester can generate a maximum power of 0.7 µW with a peak-to-peak voltage of 42.6 mV at an input vibration frequency of 94.5 Hz and an input acceleration of 0.503 G [*85*].

The following summary Table 2 provides an overview of the current state of the utilization of MEMS technology for the aforementioned energy harvesting.

Table 1. *Summary table of the state of the art of different types of EH harvesters for MEMS technology.*

Ref.	Material	Frequency (Hz)	Power (µW)	Acceleration (G)	Year
78	PDMS	3 , 23	0.00052	0.05	2023
79	PZT	68	0.233	0.25	2017
80	PZT	100.8	13.1	0.5	2016
81	PZT	215 , 202	21, 34	1.5	2013
82	PZT	27.4	0.00117	0.06	2012
83	PZT	30-47	0.0194 – 0.0513	1	2011
86	PZT	528	1.1	0.39	2010
84	Coil	54	115.1	0.57	2008
85	Coil	94.5	0.7	0.503	2009

1.6.3 Triboelectricity

Since their introduction in 2012, TENGs have attracted growing interest in the scientific and technological community due to their potential to efficiently and sustainably convert mechanical energy into electrical energy [41]. This increase in research has focused on

improving the output performance of TENGs and exploring their applications in a wide variety of fields.

Initially, different operating modes of TENGs were established, including vertical contact-separation mode [87], lateral sliding mode [88, 89], single-electrode mode [90], and freestanding triboelectric-layer mode [91], adapted according to the specific application of the device. Proper material selection is crucial for maximizing the energy efficiency of TENGs, and numerous studies have demonstrated the significant influence of materials on device performance [40, 92–94].

To increase the energy generated by TENGs, various strategies have been identified and developed, such as modification of the morphology of the dielectric material, surface activation, introduction of dielectric additives, and forced injection of external charge.

Modification of the morphology of the dielectric material involves a variety of techniques aimed at improving the surface and structural characteristics of the material to increase charge generation. These techniques include templating, which encompasses the creation of different types of three-dimensional patterns [95–98], nanopillars, [98, 99] NWs, and nanosheets on the material surface [99, 100]. Additionally, appending involves the addition of additional materials such as nanostructures [101], NPs [102, 103], electrospinning [104–106], and block copolymer (BCP) self-assembly [107–109] to enhance the roughness and contact capacity of the material. Etching includes methods such as direct laser writing [110–112], dry etching [113–116], and wet etching [117, 118], which are used to sculpt specific patterns on the material surface and thus optimize its triboelectric efficiency. Finally, crumpling is used to increase surface roughness [119, 120]. These techniques offer a wide range of possibilities for modifying the morphology of dielectric materials and enhancing their application in energy generation devices.

On the other hand, surface activation is achieved by attaching functional groups to the material surface, which can alter its triboelectric behavior and improve charge generation capacity [121–123]. The introduction of dielectric additives aims to improve material properties through the formation of nanocomposites, which can increase their ability to generate charge during interaction with another material [124–126].

Finally, forced injection of external charge utilizes methods such as ion injection to directly modulate surface charge density, which can result in a significant increase in TENG output performance [127–129]. These strategies have allowed a considerable improvement in TENG performance and have expanded their application in areas such as body motion energy generation, vibration EH, wind energy generation, and the exploitation of blue energy.

In the field of body motion energy generation, TENGs can be integrated into portable and wearable devices to collect kinetic energy during physical activity and convert it into electricity, which could power personal electronic devices or implantable medical devices [130–133]. In vibration EH applications, TENGs can be used to harness ambient vibration energy, such as that produced by industrial machinery or vehicular traffic, and convert it into electrical energy for use in remote monitoring systems or wireless sensors [134–138].

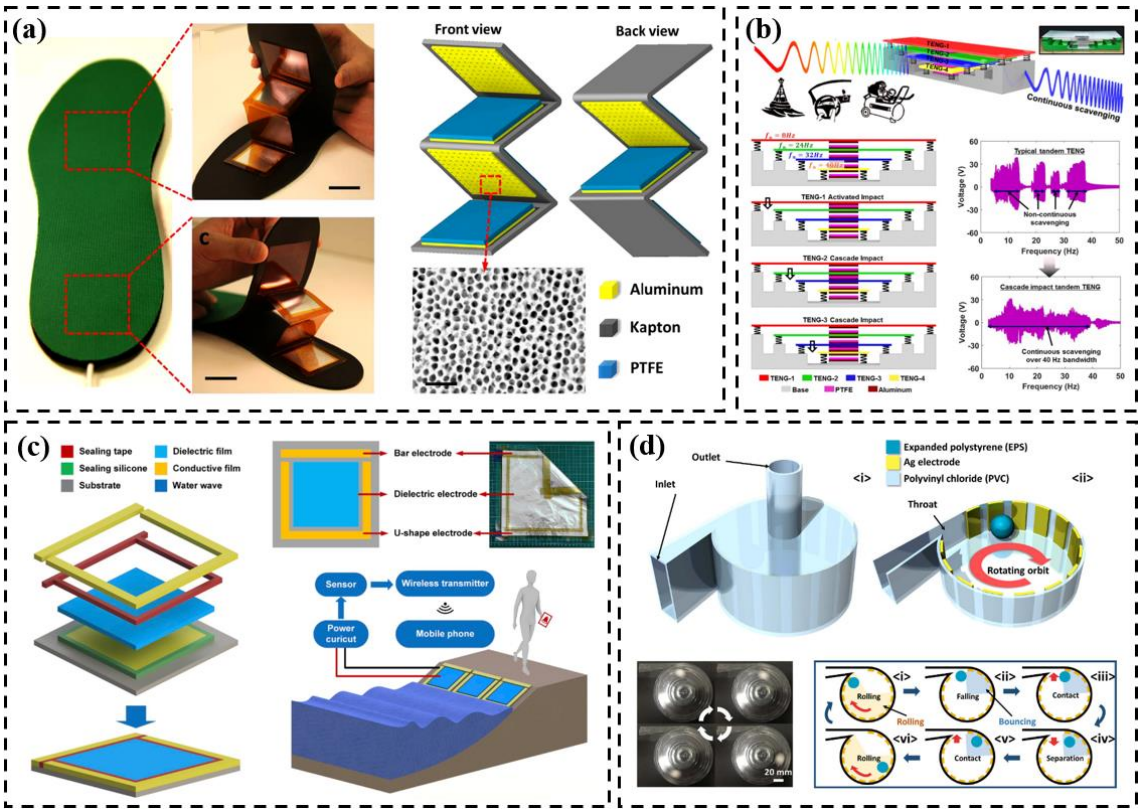


Figure 13: *Examples of TENG devices in different application sectors: (a) human motion [130], (b) vibrations [136], (c) blue energy [139], and (d) wind [140].*

In the wind energy generation sector, TENGs can be integrated into EH devices in structures exposed to wind, such as tall buildings or bridges, to capture kinetic wind energy and convert it into electricity [*140–144*]. Lastly, in the field of blue energy exploitation, TENGs can be used in devices submerged in marine environments, such as buoys or oceanic buoys, to collect energy generated by wave motion or ocean currents and convert it into electrical energy for remote offshore applications or to power oceanic sensors [*139*, *145–148*]. These application areas represent only some of the many possibilities for implementing TENGs in various fields, demonstrating their versatility and potential to contribute to innovative solutions in sustainable energy generation.

2.THESIS OBJECTIVES

The primary objective of this doctoral thesis is to advance the field of EH by focusing on the exploration and comparison of optimal materials and novel devices for the generation of power from environmental sources, such as vibrations and magnetic fields. The research is structured around two principal areas in relationship with the transduction method used. Specifically, it examines triboelectric and piezoelectric materials and devices to determine their suitability and performance in harvesting mechanical energy efficiently and cost-effectively.

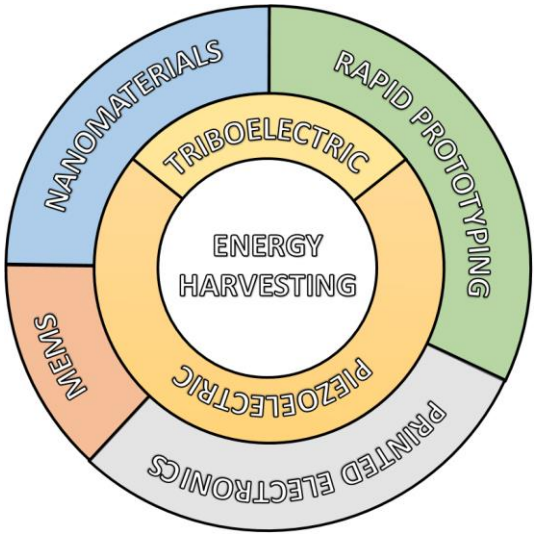


Figure 14: *Graphical diagram of the objectives of the doctoral thesis, starting from the concept of EH and extending towards the proposed materials and techniques for its utilization (from the inside out).*

In the first research block, an in-depth investigation is conducted on triboelectric materials, which harness friction and material separation phenomena to generate electricity. An analysis of the feasibility of these materials in various contexts and applications will be carried out, evaluating their efficiency, performance, and cost in energy generation. Advanced RPTs such as laser cutting, plotting, and 3D printing are employed to facilitate the rapid fabrication and evaluation of EH devices.

In the second research block, piezoelectric materials are studied, which convert mechanical energy into electricity due to the material deformation. Various technologies and techniques are explored to optimize EH, including the use of MEMS, PE applications, and the utilization of NMs to improve the efficiency and adaptability of piezoelectric devices.

Both research blocks aim to harness residual sources of energy, such as vibrations, MFs, and body movement, to generate electricity sustainably and autonomously.

The objectives are summarized as follows:

- Investigate and compare materials for EH, both triboelectric and piezoelectric.
- Evaluate the feasibility, efficiency, and associated costs of these materials.
- Utilize RPT for the fabrication of EH devices based on these materials.
- Implement technologies such as MEMS, PE, and NMs to enhance the efficiency of piezoelectric devices.
- Harness residual sources of energy, such as vibrations, MFs, and body movement, to generate electricity sustainably and autonomously.
- Carry out the fabrication and characterization of different collectors in specific applications.

2.1 Thesis Framework

The work of this thesis has been carried out at the facilities of the Institute of Microelectronics of Barcelona (IMB-CNM, CSIC), within the "Nano and Microsystems" department supervised by Dr. Gonzalo Murillo. Throughout this thesis, Marcos Duque conducted his research, producing the four scientific articles presented in this thesis (two already published, one accepted for publication and one under review), the filling of a European patent application, and several contributions to scientific conferences.

3 RESULTS

3.1 Tapping-actuated triboelectric nanogenerator with surface charge density optimization for human motion energy harvesting

Tapping-actuated triboelectric nanogenerator with surface charge density optimization for human motion energy harvesting

Marcos Duque and Gonzalo Murillo

Department of Nano and Microsystems, Instituto de Microelectrónica de Barcelona (IMB-CNM, CSIC), Bellaterra 08193, Spain;

Abstract

In this article, triboelectric effect has been used to harvest mechanical energy from human motion and convert it into electrical energy. To do so, different ways of optimizing the energy generated have been studied through the correct selection of materials, the design of new spacers to improve the contact surface area, and charge injection by high-voltage corona charging to increase the charge density of dielectric materials. Finally, a triboelectric nanogenerator (TENG) has been manufactured, which is capable of collecting the mechanical energy of the force applied by hand tapping and using it to power miniaturized electronic sensors in a self-sufficient and sustainable way. This work shows the theoretical concept and simulations of the proposed TENG device, as well as the experimental work carried out.

1. Introduction

The triboelectric effect, also called contact electrification, has been known for thousands of years and implies that when two different materials come into contact, charges will be transferred from one material to the other, depending on their respective electron affinity [149]. Due to its inherent characteristics, the triboelectric effect can cause extremely high voltages. Traditionally, it has been considered a negative effect, especially in the electronics industry, due to the damage that it can cause to integrated circuits. In 2012, triboelectric nanogenerators (TENGs) were invented to take advantage of this previously negative effect and use it for energy harvesting [150, 151].

Due to the great advancement of technology and telecommunications, the interest in the IoT is increasing rapidly [152]. This concept allows the interconnection of thousands of wireless sensors to capture environmental information and make decisions without human interaction. Nevertheless, these sensors must be powered, and this is a major drawback due to their dependence on batteries. An alternative to avoid the use of batteries is to harvest ambient energy and convert it into electricity.

A lot of attention has been dedicated to the use of TENGs for energy harvesting, as they have been shown to be an easy and low-cost way of converting mechanical energy into electricity. This mechanical energy is produced by many sources such as ambient vibrations [153–155], magnetic fields [156, 157], human motion [130, 158–164], wind [165–167], water [*143*], waves [168, 169], vibration by moving vehicles [170, 171] and time-limited and random vibrations [172–174]. This widely distributed and collected ambient mechanical energy can be used to supply low-power electronic sensors in a self-sufficient way and can be used for common IoT applications for predictive maintenance, system sensing, or the measurement of environmental parameters.

As shown in Figure 1, there are four basic working modes to operate a TENG [175]. Contact-separation mode uses polarization in the vertical direction, so the system energy is increased when the electrodes separate, which corresponds to the decrease in the capacitance in a parallel-plate capacitor. Lateral-sliding mode uses polarization in the lateral direction because of the relative slip between the two materials. The material

friction creates the charge separation, as well as a capacitance change. Single-electrode mode harvests energy from a freely moving surface without opposite electrode. Free-standing mode is designed for power generation by electrostatic induction between a pair of electrodes, due to the presence of a sliding charge structure. In many cases, two or more modes can work together.

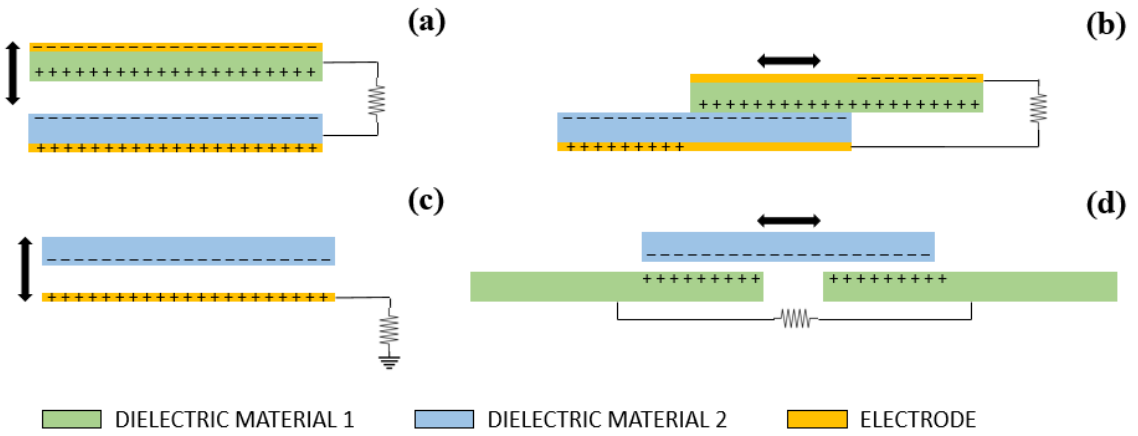


Figure 1. *Four basic modes of work of a TENG: (a) vertical contact-separation mode; (b) lateral-sliding mode; (c) single-electrode mode; (d) free-standing mode.*

Contact-separation mode is the one used in our work. This mode requires an external force for the triboelectric material and the electrode to come into contact, to later separate the contact surfaces. This subsequent separation is usually carried out by means of springs, a spacer, or the deformation of the material itself. The use of additional spacers, by means of gaskets [176, 177], sponges [131, 178], and springs [102, 179] or the general deformation of the substrate such as an arched shape [95, 180] or triangle prisms [181], increases the cost of the TENG due to greater manufacturing complexity. In addition, many spacers require a greater expansion of the deformation area.

Previous works have proposed a TENG with an etched pattern spacer [182]. This design etches different patterns into the substrate and folds them into small spacers that are evenly distributed on the contact surface. This system presents problems in the generation of energy, due to the fact that there is always a contact between the top electrode and the triboelectric material and, thus, a deficiency in the work area contact. Here, in this work, a system using an engraving pattern in the outer zone of the contact surface of the materials is presented.

Voltage and current outputs of TENGs are proportional to the triboelectric charge density on the contact surfaces. Therefore, a key approach to improve the TENG output performance is to increase the triboelectric charge density through the correct choice of utilized materials, e.g., [40, 183, 184]. That is, by choosing materials with a higher electron transfer capacity after contact electrification, a higher energy generation will be achieved. Surface modification enlarges the surface area, such as: nanoparticles self-assembly [102], pyramid patterns from photolithographic patterning [95], and surface dry-etched polymer nanowires [89, 113]. Structure optimization maximizes the contact area, such as: cylindrical rotating TENG with multiple-layer integration [185] or an advanced PCB composite disk-structure TENG with narrow gratings [186] and the use of a specific power management circuit named Bennet's doubler to maximize energy efficiency [187]. However, further improvements in performance are needed to be able to supply low-power electronic sensors in a self-sufficient and sustainable way.

Due to the intrinsic properties of dielectric materials to almost permanently retain large amounts of charge (known as electret), the surface charge density of dielectric films can be increased several times by charge injection. Charge injection methods include ionized-air injection, plasma polarization, high-voltage corona charging, and electron beam bombardment [127, 188]. High voltage corona charging is the simplest, cheapest, and most widely used process in industrial manufacturing.

In this work, research on the triboelectric materials with the highest intrinsic surface charge density and lowest cost is carried out. Furthermore, a study on the increase in charge injection of different triboelectric materials, by means of high-voltage corona charging, is performed. In addition, an adaptation of a triboelectric generator with engraved pattern spacers is proposed for the improvement of the contact area and its subsequent fabrication. In order to validate the measurements obtained after the injection of charge, a finite element modeling (FEM) has been carried out using COMSOL Multiphysics®. Finally, an example of an application is shown, where the mechanical energy from hand tapping is collected and used to power a group of 30 light emitting diodes (LEDs).

2. Experimental Section

2.1. Study of Triboelectric Materials

The selection process of the materials to be studied is based on numerous works reporting triboelectric series [40, 184]. For this case, materials with the highest intrinsic surface charge density have been chosen, also taking into account the material cost. These selected materials are polytetrafluoroethylene (PTFE), polyamide (Kapton), polyether ether ketone (PEEK), and biaxially oriented polyethylene terephthalate (BoPET, Mylar).

The open-circuit voltage V_{oc} of a TENG can be expressed as [189]:

$$V_{OC}(\mathrm{TENG}) = \frac{\sigma\, x(t)}{\varepsilon_0}, \qquad (1)$$

where σ is the surface triboelectric charge density between the electrification materials, ε_0 is the vacuum permittivity and is the separation distance.

For the characterization of these materials, we integrated different triboelectric materials in a test platform (10 cm × 10 cm) made of PMMA with four metal guides and four springs to retract both surfaces after touching. The triboelectric material and the copper layers are disposed of in between the PMMA structure faces. Different samples of the triboelectric material, 5 cm × 5 cm in size and 50 µm thick, have been used. As shown in Figure 2a, two copper electrodes and a single dielectric material are used (contact separation mode). Periodically, the top electrode separates after getting in contact with the dielectric surface to effect charge transfer. In order to carry out the electrical measurements, a characterization setup has been assembled (Figure 2b, c) consisting of a stepper motor (Zaber® LSQ075B-T3-MC03 and X-MCB1-KX13B), a dynamometer (Mark M5i and MR03-20 sensor for a maximum force of 100 N), a Sourcemeter (Keithley® 2470), and a LabVIEW® program that controls the entire electrical characterization setup.

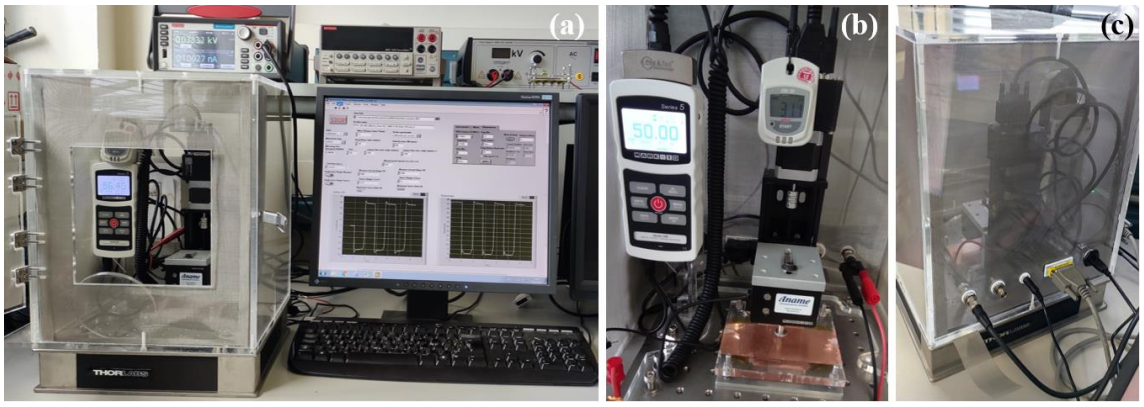


Figure 2. *(a) Schematic of material and electrode used for the characterization of the materials; (b, c) ad hoc setup for electromechanical characterization of triboelectric devices.*

For the characterization of the materials, the linear motor produces a vertical motion to make physical contact between the material and the top electrode. A force of 50 N, which is approximately the force generated by a human footstep, is applied. Figure 3 shows the different triboelectric materials and the average generated voltages. As observed, voltages ranging from −35 V to −57 V can be achieved with a single piece of material. All the measurements were performed with three samples of each type (n = 3). For all the tests, the measured ambient temperature and relative humidity were around 30 °C and 20%, respectively.

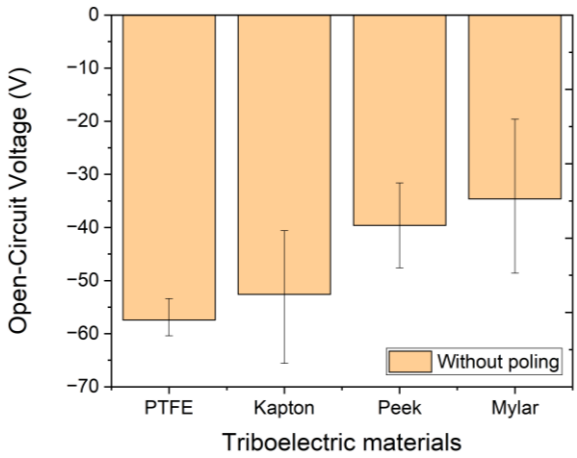


Figure 3*. Comparison of voltages generated for the different material samples.*

2.2. Surface Charging Process

To increase the surface charge density of dielectric films, as already mentioned above, charge injection is performed by high-voltage corona charging. To do so, as shown in

Figure 4a, a PCB with multiple metal tips was designed and manufactured. Using a high-voltage source (Frederiksen® 3670.60), a high voltage is applied to the multi-tip electrode. The current flows from the high-potential multi-tip electrode to the ground plane, through the air, by ionizing and creating a region of plasma around the needles. The ions eventually pass the charge to lower potential areas of the dielectric material. In order to clarify this process, Figure 4b shows the schematic of the injection process discussed above.

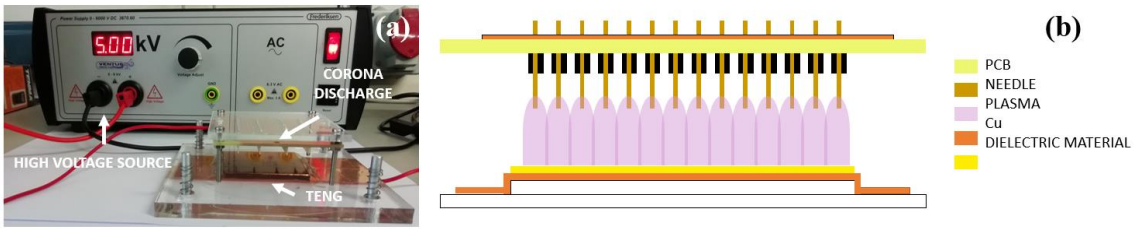


Figure 4. *(a) Charge injection setup using high voltage corona charging; (b) schematic of the process of charge injection by corona.*

Firstly, to study the optimum voltage and time to be applied to the corona, PTFE has been chosen as the material, since it is the material that generates the highest output voltage for an applied force. A voltage sweep is performed from 1000 V to 6000 V, with a gradual increase of 1000 V. Figure 5a shows the open-circuit voltage that the material can generate with an electrode separation of 5 mm. The greater the voltage applied to the corona, the greater the increase in charge density of the material.

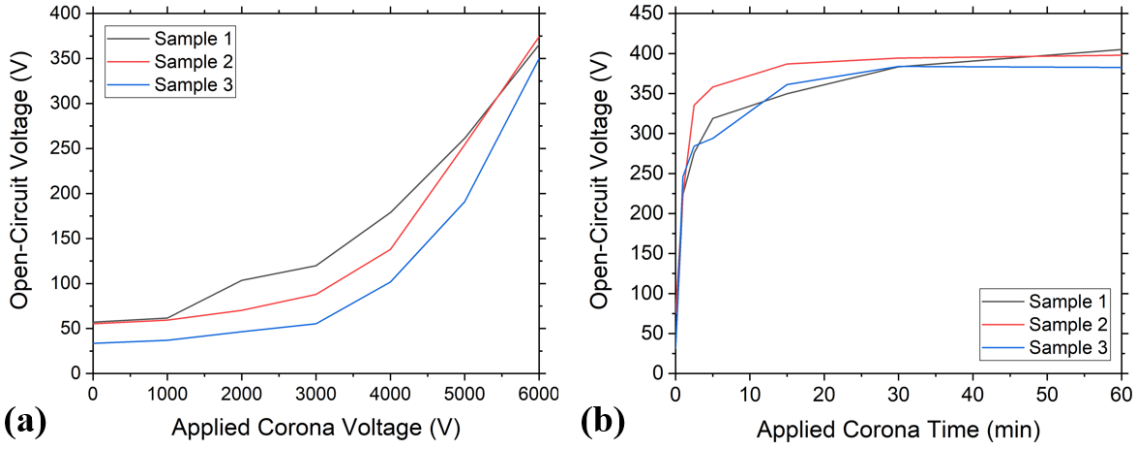


Figure 5*. (a) Graph of the generated open-circuit voltage as a function of the voltage applied to the corona discharge; (b) graph of the open-circuit voltage that can be generated by the material as a function of the injection time with a constant corona discharge voltage of 6000 V.*

For a constant voltage of 6000 V applied to the corona discharge, we performed a study on how long it takes to achieve the maximum surface charge. As can be seen in Figure 5b, after 15 min of application time, the maximum voltage generated stabilizes, and, therefore, the maximum surface charge density that the material can support is reached.

Although the humidity and temperature were monitored during the charging process, it can be very sensitive to tiny changes in these parameters, air pressure, or surface cleanness. All the parameters and samples were identical; however, a variability can be observed from one to another. The best future solution to increase reproducibility is to have a specific chamber with a specific gas at controlled pressure and temperature.

Finally, the charge injection is carried out by applying a constant voltage of 6000 V and a period of 15 min. In the Figure 6a, it can be seen how the materials with the lowest intrinsic charge density, such as PEEK and Mylar, are now the ones with the highest surface charge density and, therefore, the ones that generate the highest maximum voltage.

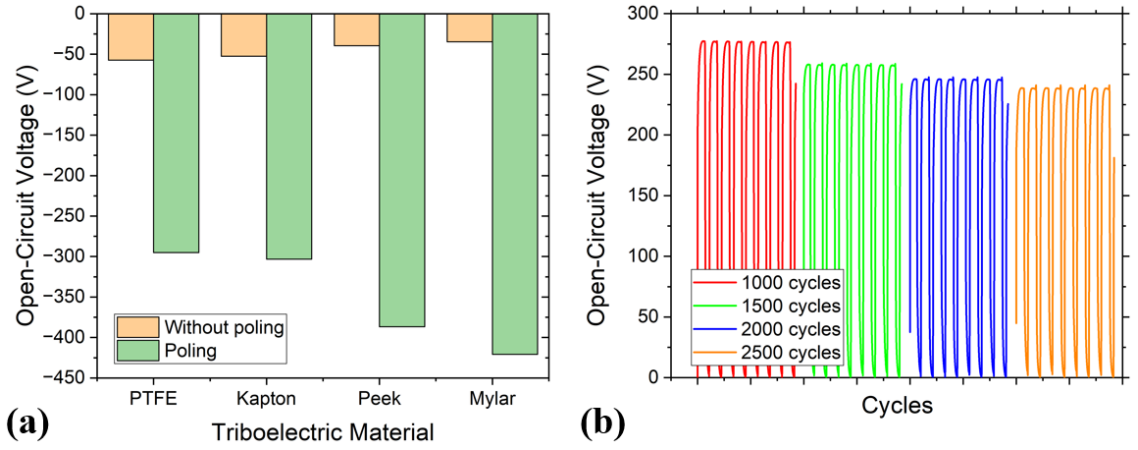


Figure 6. (a) Comparison of voltages generated with the different samples of polarized materials for 15 min and a voltage of 6000 V; (b) measurements of eight contact cycles for each material to validate the permanent effect of polarization.

Concerning the permanent effect of this polarization, the surface charge density is limited by the breakdown of the electric field in the air. This ion-injection method is an effective way to increase the output power by up to 25 times. This has been proven to be stable over 5 months and 400,000 continuous operation cycles [190]. In our case, as shown in

Figure 6b, after 1500 cycles, the voltage drops 6%, and, after 2500 cycles, it drops 12%. Finally, after 2500 cycles, the voltage remains stable.

2.3. Finite Element Modeling

TENG devices have been simulated with COMSOL Multiphysics® to compare the results of the electrical characterization with a theoretical model. The used module for this simulation is AC/DC Module (Electrostatics). The 2D model built in COMSOL Multiphysics® consists of a box air (20 cm × 20 cm), the triboelectric material, and the copper electrodes, one is defined as ground and the other as floating potential. A specific surface charge density calculated by using Equation 1 has been assigned to the surface of the triboelectric material.

The model is created using a fine triangular mesh. The mesh contains more than 50,000 elements. Figure 7a shows the electric potential generated by the Mylar sample, with distance of 5 mm between the electrodes. Figure 7b,c show the output open-circuit voltage for different triboelectric materials without and with corona charging respectively. As seen, the simulated results are in agreement with the electrical measurements.

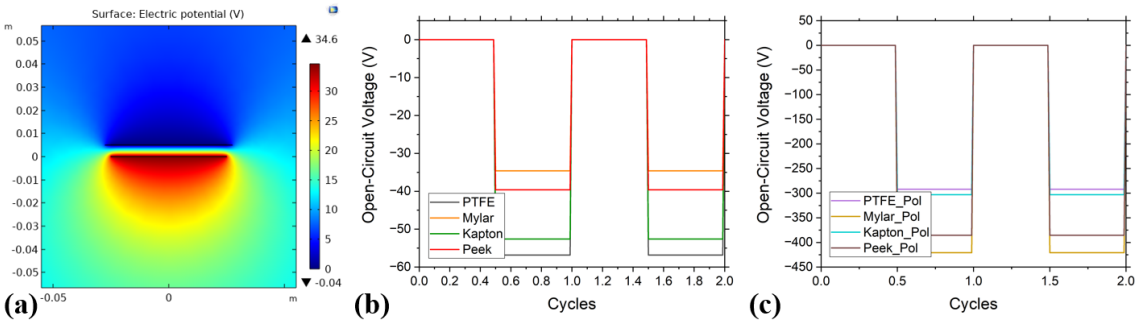


Figure 7. *(a) Electric potential (in volts) generated by the Mylar sample with an electrode separation of 5 mm. (b,c) Open-circuit voltage for different triboelectric materials without and with corona charging, respectively.*

2.4. Fabrication of the Prototype

Figure 8a,b show the schematic and operating scheme of the TENG device based on contact separation mode. The specific working process in divided into three steps. In the first step, the spacers are flattered by the impact force so that the copper electrode fully

contacts the dielectric film. Here, copper is used as the tribometallic material and top electrode. Due to the significant difference in the electronic affinity of the two materials, net positive charges are generated on the surface of the copper layer, and equal net negative charges are left on the surface of the dielectric film. Second, the spacers return to their original folded state due to their inherent elastic force, until the maximum vertical distance is reached. This conducts free electrons from the bottom copper electrode of the dielectric film to the top copper electrode through an external circuit to compensate for the potential difference between the two electrodes. Finally, the spacers are pressed again under another external mechanical impact, the top electrode and dielectric film are fully in contact again, and free electrons will flow from the top electrode through the external charge back to the bottom electrode. The previous three steps of the TENG formed a complete and repeatable cycle of electrical power generation.

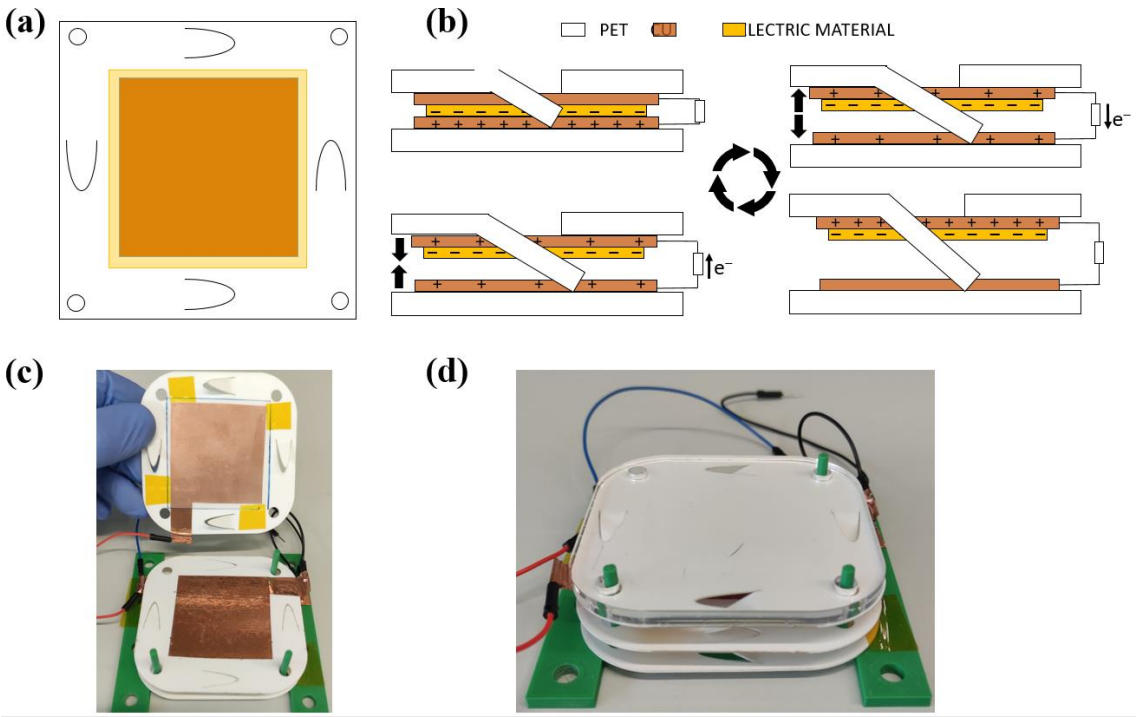


***Figure 8**. (a) Scheme of the TENG device; (b) scheme of operation of the TENG device; (c,d) image of the manufactured TENG device before and after assembling, respectively.*

For the manufacturing of the TENG device, a 70 mm × 70 mm × 0.5 mm PET (polyethylene terephthalate) substrate has been used for the bottom part. On the PET substrate, a piece of adhesive copper of 45 mm × 45 mm × 0.05 mm is adhered. This electrode will be smaller than the dielectric material to avoid possible shortcuts between electrodes.

Finally, a Mylar layer is adhered to the bottom copper electrode, 50 mm × 50 mm × 0.05 mm. For the top electrode, we use a PET sample of the same dimensions as the bottom one, but with the different spacers engraved by laser cutting at the ends of the structure. A 45 mm × 45 mm × 0.05 mm piece of adhesive copper is also attached as the top electrode.

To improve the energy generated by the TENG device, two of them have been manufactured in a stack (Figure 8c,d) and have been measured individually, connected in series and in parallel. For this stack manufacturing, the process is identical, but, in this case, the top PET substrate of the first TENG and the bottom one of the second are shared to minimize cost and volume.

2.5. Electrical Characterization

For the electrical characterization of this TENG device, as shown in Figure 8, two different measurements have been carried out. First, we measured the maximum voltage generated by contacting the device directly to the sourcemeter. Second, we connected the device to a diode bridge and a capacitor of 10 µF to rectify the signal and store the energy. Then, by means of a switch, the stored energy is connected to 30 LEDs. For these measurements, in order to show a real application, instead of applying 50 N of force with a stepper motor, the force was applied with the palm of the hand, obtaining an average of 8 N of force.

For the first measurement, each of the dielectrics was measured separately. As shown in Figure 9a, the maximum voltages are very similar, reaching a value of 170 V. By connecting the two materials in series, the voltage increases to 250 V. Ideally, the voltage should be doubled, but manually applying the force and not contacting each dielectric with its top electrode in phase do not reach this maximum voltage. An improvement of 50% improvement over a single individually connected device is obtained.

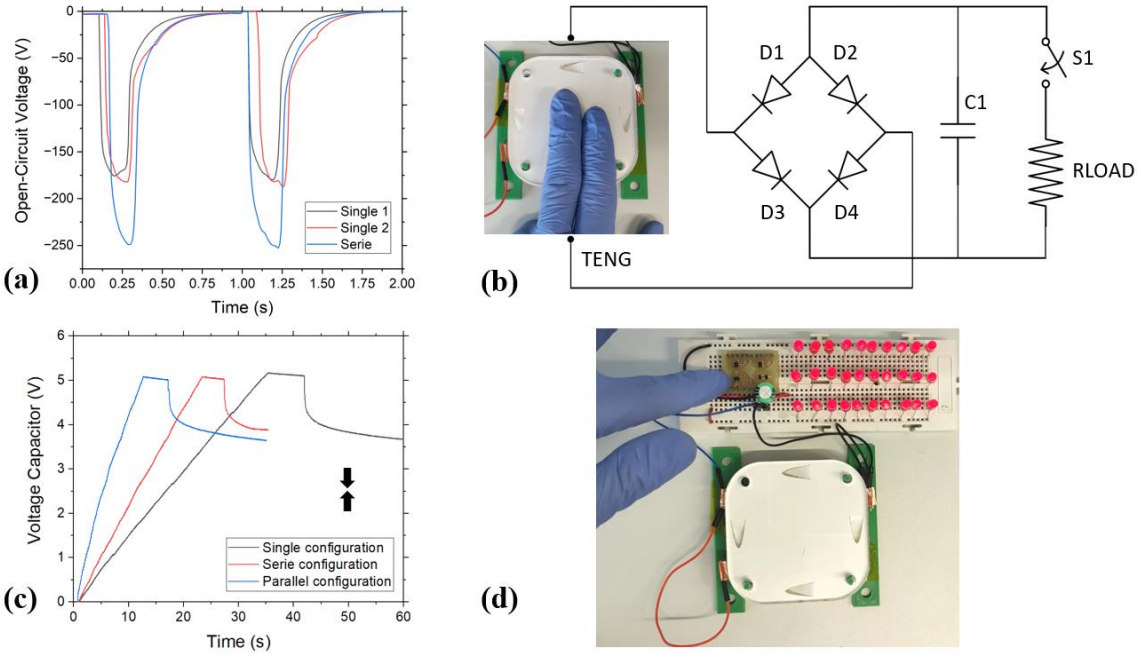


***Figure 9**. (a) Voltage generated by each device individually and connected in series; (b) circuit diagram and photograph of the TENG device powering the 30 LEDs; (c) process of charging and discharging the capacitor for a capacity of 10 µF; (d) TENG device used to light 30 LEDs up.*

In the second characterization, as previously mentioned and shown in the schematic of Figure 9b, the device output is connected to a diode bridge, together with a capacitor of 10 µF, and is charged up to 5 V. Once the 5 V is reached, which corresponds to a stored capacitor energy of 125 µJ, there are a few seconds without charging, and then the LEDs are connected through the switch to illuminate them for 150 ms (Figure 9d). Figure 9c shows the comparative graph of charge and discharge of the 10 µF capacitor when powering the 30 LEDs and applying force with the palm of the hand at an approximate frequency of 6 Hz. It can be observed that when using a single device, the charging process takes 35 s, while when connecting two devices in series, this time is reduced to 23 s. Decreasing the charging time of the capacitor by 35%. In the same way, if the two devices are connected in parallel, the charging time is reduced to 12 s. This decreases the time by 65%, compared to the single device. From these results, we can infer that a power of 10 µW can be generated by two devices connected in parallel.

3. Discussion and Conclusions

In this article, the fabrication of a TENG device has been carried out, which can collect the mechanical energy of the force applied by tapping with the palm of the hand. This energy could be used to power low-power electronic sensors in a self-sufficient way.

In order to manufacture the TENG devices, the most suitable materials (i.e., those with the highest surface charge transfer and most cost-effective) have been studied. In addition, the design of the spacers has been optimized to improve the contact surface and reduce the final costs of the device.

To increase the surface charge density, charge injection was carried out by means of high-voltage corona charging. The voltages to be applied and the optimal time for this charge injection were examined.

To validate the correct operation of the TENG device, electrical characterizations with different mounting configurations were carried out. By using a stack of only two devices connected in parallel, 30 LEDs were illuminated every 12 s, thanks to a power generation of 10 μW produced by hand tapping.

Supplementary Materials: The following supporting information can be downloaded at: www.mdpi.com/xxx/s1. Video S1: Device lighting 30 LEDs.

Author Contributions: Conceptualization, M.D. and G.M.; methodology, M.D. and G.M.; investigation, M.D. and G.M.; writing—original draft preparation, M.D.; writing—review and editing, G.M.; supervision, G.M. All authors have read and agreed to the published version of the manuscript.

Funding: This research was funded by the La Caixa Foundation under the Junior Leader Retaining program (LCF/BQ/PR19/11700010), EUR2020-112082 under the Dynamization Actions ”Europa Excelencia 2020” funded by the NextGenerationEU Instrument, and Ramon y Cajal Fellowship 2020 (RYC2020-030501-I).

Institutional Review Board Statement: Not applicable.

Informed Consent Statement: Not applicable.

Data Availability Statement: Data are contained within the article or Supplementary Material.

Acknowledgments: G.M. appreciates the financial support from the La Caixa Foundation under the Junior Leader Retaining Fellowship (LCF/BQ/PR19/11700010), project EUR2020-112082 under the Dynamization Actions “Europa Excelencia 2020” funded by the NextGenerationEU Instrument, and the Ramon y Cajal Fellowship 2020. This work has been carried out in collaboration with ENERGIOT DEVICES SL (www.energiot.com) and in the framework of the doctoral program in Electronic and Telecommunication Engineering of the Autonomous University of Barcelona.

Conflicts of Interest: The authors declare no conflicts of interest.

3.2 Low-cost manufacturing of monolithic resonant piezoelectric devices for energy harvesting using 3D printing

Low-cost manufacturing of monolithic resonant piezoelectric devices for energy harvesting using 3D printing

Marcos Duque and Gonzalo Murillo *

Department of Nano and Microsystems, Instituto de Microelectrónica de Barcelona – Centro Nacional de Microelectrónica (Consejo Superior de Investigaciones Científicas) (IMB-CNM, CSIC), 08193 Bellaterra, Spain.

Abstract

The rapid increase of the Internet of Things (IoT) has led to significant growth in the development of low-power sensors. However, the biggest challenge in the expansion of the IoT is the energy dependency of the sensors. A promising solution that provides power autonomy to the IoT sensor nodes is energy harvesting (EH) from ambient sources and its conversion into electricity. Through 3D printing, it is possible to create monolithic harvesters. This reduces costs as it eliminates the need for subsequent assembly tools. Thanks to computer-aided design (CAD), the harvester can be specifically adapted to the environmental conditions of the application. In this work, a piezoelectric resonant energy harvester has been designed, fabricated, and electrically characterized. Physical characterization of the piezoelectric material and the final resonator was also performed. In addition, a study and optimization of the device was carried out using finite element modeling. In terms of electrical characterization, it was determined that the device can achieve a maximum output power of 1.46 mW when operated with an optimal load impedance of 4 MΩ and subjected to an acceleration of 1 G. Finally, a proof-of-concept device was designed and fabricated with the goal of measuring the current passing through a wire.

1. Introduction

The large increase in the Internet of Things (IoT) has led to a huge growth in the development of very low-power sensors that communicate with each other and form a large wireless network [6, 21, 22, 152] . The greatest difficulty in the expansion of the IoT is the energy dependence of the sensors, limited by the use of their batteries. For this reason, we are facing a great barrier due to the high cost of replacing batteries and the environmental impact that it entails. A promising solution that provides autonomic energy to the IoT sensor nodes is the harvesting of residual environmental energy, such as movement, vibrations, magnetic fields, light or heat, and converting them into electrical energy (Energy Harvesting (EH)) [20–23]. Mechanical energy can be converted into electrical energy using piezoelectric transducers [31, 32, 191, 192].

In vibrational energy harvesting, piezoelectric materials are one of the most widely used transducers. For the last 20 years, piezoceramics, such as lead zirconate titanate (PZT), have been the dominating materials. After the classification of lead as a toxic material, restrictions on its use have increased, opening the opportunity to investigate new lead-free materials such as Polyvinylidene fluoride (PVDF) and its copolymers.

Three-dimensional printing or additive manufacturing (AM) is a process of making three-dimensional solid objects from a digital file [*143*, *193–195*]. It is increasingly used for the production of any type of custom design in the fields of agriculture, healthcare, automotive and aerospace.

AM technologies are based on three types: Synthesis, in which the temperature of the material is raised without liquefying it to create high-resolution prototypes, fusion, in which powders are fused by means of electron beams, and stereolithography, which uses a method called photopolymerization, which uses an associated ultraviolet laser [196].

According to the American Society for Testing and Materials (ASTM), AM has been divided into seven processes that include:

Blinder jetting (BJ), an additive manufacturing process in which a liquid bonding agent is selectively deposited to join powder materials; directed energy deposition, an additive manufacturing process in which focused thermal energy is used to fuse materials by

melting them as they are being deposited; material extrusion, an additive manufacturing process in which material is selectively dispensed through a nozzle or orifice; material jetting, an additive manufacturing process in which droplets of build material are selectively deposited; powder bed fusion (PBF), additive manufacturing process in which thermal energy selectively fuses regions of a powder bed; sheet lamination, an additive manufacturing process in which sheets of material are bonded to form an object; vat photopolymerization, an additive manufacturing process in which liquid photopolymer in a vat is selectively cured by light-activated polymerization.

Fused deposition modeling (FDM) is a material extrusion process used to make thermoplastic parts through heated extrusion and deposition of materials layer by layer. FDM is the most popular technology for 3D printing.

There are many 3D printing materials such as; PLA (polylactic acid), ABS (acrylonitrile butadiene styrene), PVA (polyvinyl alcohol), PP (polypropylene), PLA Tough, CPE (co-polyester), PET-G (glycol-modified polyethylene terephthalate), Nylon (polyamide) and PC (polycarbonate), but the most common material is PLA. PLA is a biodegradable and recyclable polymer that is a reliable and easy-to-print material that can be printed at low temperatures. It has a low shrinkage factor and does not require the use of a heated build plate. A special type of PLA, called Tough PLA, combines the ease of printing with increased mechanical performance. Specifically, tough PLA has increased impact resistance, avoiding the typical brittle failure of normal PLA. Tough PLA is used for functional prototyping tooling and manufacturing aids.

Through 3D printing, it is possible to create monolithic functional structures (i.e., resonators, sensors, energy harvesters, etc.). This reduces costs as it eliminates the need for subsequent assembly tools. It is a technology that does not require additional molds, allowing for quick design variations and the creation of more complex structures. Furthermore, thanks to computer-aided design (CAD), the devices can be specifically tailored to the environmental conditions of the application. Figure 1 illustrates the advantage of integrating piezoelectric materials by 3D printing to create monolithic 3D-printed piezoelectric devices. In this way, it is possible to adapt the harvester to our

needs, making it fully customizable, and the cost of the final device is reduced because subsequent assembly is not required.

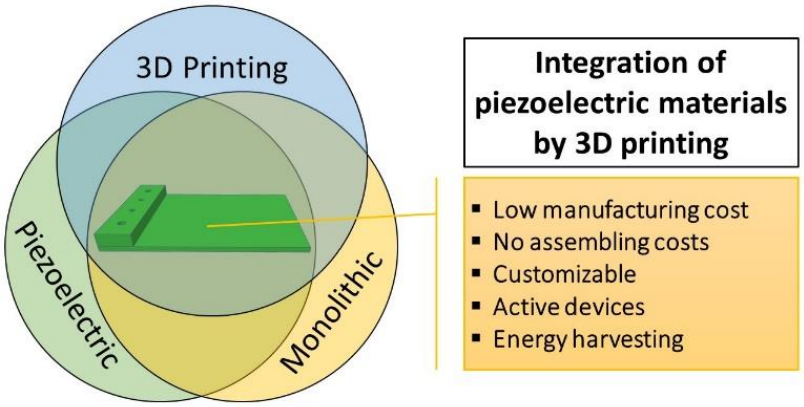


***Figure 1**. Advantages of using a hybrid solution of 3D printing and energy harvesting.*

In the literature, there are several studies on the use of 3D printing to create energy harvesters. In most of these works, the printed piece is used as a support and the harvester is assembled later [*197*, *198*, *207*, *199–206*]. In this work, a resonant piezoelectric energy harvester has been designed and manufactured, using 3D printing by hybridizing this technology with a piezoelectric material (PVDF) to achieve a monolithic energy harvester. In addition, a study and optimization of the device have been carried out by means of finite element modeling (COMSOL Multiphysics®). Finally, a use-case resonator was designed and fabricated with the goal of measuring the current carried by a wire.

2. Material and Methods

2.1. Structural and Functional Materials

The piezoelectric material used in the harvester is a commercially available PVDF film with two parallel electrodes, from TE Connectivity. According to the manufacturer's specification, the PVDF material has a thickness of 110 µm and 6 µm for each silver ink electrode. The piezoelectric coefficient of the commercial PVDF is -33×10^{-12} m/V, according to the datasheet. The selected material for the structural harvester is Ultimaker Tough PLA green from Ultimaker, with a Young's modulus of 2.8 ± 0.15 GPa and a density

of 1.22 g/cm^3. A neodymium (Nd) mass with a density of 7 g/cm^3, from Supermagnete, was used.

2.2. Finite Element Modelling

Finite element modeling (FEM) of the energy harvester was conducted using COMSOL Multiphysics® 6.0. The AC/DC (Electrostatics, Electrical Circuits and Piezoelectricity) and Structural Mechanics (Solid Mechanics and Piezoelectricity) modules were utilized for the simulation. The model was created using a fine triangular mesh, consisting of over 25,000 elements.

2.3. Manufacturing Process and Characterizations

The Ultimaker S3 printer with AA 0.25 mm nozzle was employed for the manufacturing process, allowing printing layers from 60 µm to 150 µm thick.

The initial characterization involved a stepper motor from Zaber® Technologies LSQ075B-T3-MC03 (Vancouver, BC, Canada), capable of performing movements from 1 mm to 6 mm on the Z-axis. Concurrently, the voltage generated by the harvester was measured using a Sourcemeter Keithley® 2470 (Cleveland, OH, USA). A force sensor Mark-10® (Copiague, NY, USA) MR03-20 fixed onto the stepper motor recorded the data with the assistance of a dynamometer Mark-10® M5I. An ad-hoc LabVIEW® program controlled the setup comprising the devices.

The second electrical characterization was conducted using an electrodynamic shaker VR9500 from Vibration Testing Controller (Jenison, MI, USA) to emulate environmental vibrations at different input acceleration magnitudes. This process was controlled by a customized MATLAB® program, enabling automation, acquisition, and processing of voltage measurements. All data were measured using an acquisition system from National Instruments (Austin, TX, USA) PCI-6132 and a BNC-2110 terminal block.

The piezoelectric coefficient of the material was measured using a Wide-Range d33 piezometer from APC International, Ltd (Mackey Ville, PA, USA).

3. Results

3.1. Design of the Harvester

3.1.1. Definition Fixed Parameters

There are different sources for energy harvesting, such as vibrations, human motion, residual magnetic field, etc. In this case, we have chosen the magnetic fields generated by a current-carrying conductor. For this reason, the resonance frequency is fixed at 50 Hz (European electric grid frequency).

In order to study structure optimization, an effective area and resonance frequency of the device must be set. In this case, the dimensions are 50 mm × 40 mm (length × width).

3.1.2. Device structure

There are different types of structures for vibrational harvesters, such as cantilevers, doubly supported beams or diaphragms. The cantilever results in the highest power output when used as a piezoelectric energy harvester. Furthermore, the cantilever structure leads to the lowest resonance frequency for a given size. For this reason, the cantilever structure has been chosen.

The resonance frequency of a spring-mass system can be expressed as [208–210]:

$$f_r = \frac{1}{2\pi}\sqrt{\frac{k_{eff}}{m_{eff}}}, \quad (1)$$

Here, *keff* and *meff* represent the effective suspension stiffness and the effective mass values, respectively.

The neutral axis of a beam is the layer in the cross-section of a beam that experiences no longitudinal strain under bending. For composite beam structures, the effect of the different materials of each layer must be summed up to find the neutral axis:

$$Z = \frac{\sum_{i=1}^{n} z_i Y_i h_i}{\sum_{i=1}^{n} Y_i h_i}, \quad (2)$$

Where *Z* is the neutral axis position of the composite beam, *Zi* is the height of the centroid of layer *i*, *hi* is the thickness of layer *i* and *Yi* is Young's modulus of layer *i*.

3.2. Shape Optimizations and Finite Elements Modeling

3.2.1. Obtaining Resonance Frequency

In addition to the reduction in the manufacturing cost, by having a monolithic device, anchor losses are avoided due to the improved resonator anchor structure. To achieve the desired resonance frequency, a mass with a very large thickness was required due to the low density of the PLA. Furthermore, to achieve actuation with magnetic fields by means of Lorentz's force, a ferromagnetic material is needed as a cantilever tip mass. For this reason, Nd magnets have been used as an inertial mass.

As shown in Figure 2a, our harvester consists of a PLA cantilever with a length composed of the length of the beam (Lb), the mass (Lm) and the length of the cantilever (Lc). Moreover, the thickness of the beam has been defined as (Tb), the thickness of the mass as (Tm) and the depth of the piezoelectric material with respect to the surface as (Pd).

The 3D model shown in Figure 2b consists of the energy harvester with the piezoelectric layer inside the structure and an external circuit with a load resistor to calculate the power.

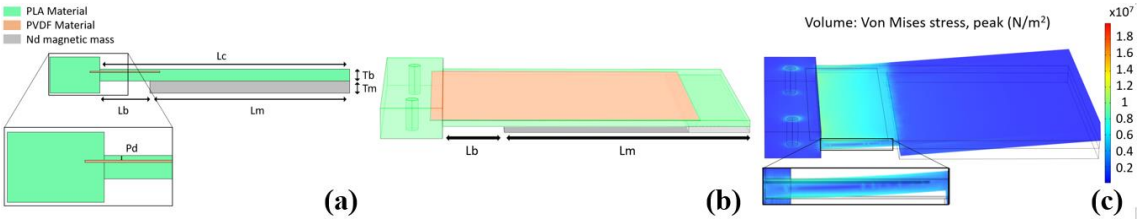


Figure 2. *(a) Schematic of the cross-section of the energy harvester with the dimensions; (b) 3D design used and (c) stress distribution when the harvester resonates at its resonance frequency and detail of the cross-section showing the neutral axis in COMSOL Multiphysics®.*

A piezoelectric material produces an electrical charge from mechanical stress. The d_{33} coefficient represents the piezoelectric charge coefficient along a specific direction, reflecting the material's response to applied stress. It can be expressed as:

$$d_{33} = \frac{\Delta Q}{\Delta S}, \quad (3)$$

Where ΔQ is the induced charge density and ΔS is the applied stress along a particular axis.

From Equation (2), it can be deduced that the highest stress resulting from a beam deformation in a cantilever is located on the surface. In Figure 2c, the stress distribution is shown when the device resonates at its resonance frequency. It can be observed that the stress on the surface of the material is at its maximum, while it is zero at the center of the beam. Consequently, during the manufacturing process, it is crucial to position the encapsulated piezoelectric material as close to the surface as feasible. However, there is a trade-off, if the piezoelectric layer is too close to the surface, it will not be properly embedded and can get delaminated.

A parametric simulation of Lb and Lm is performed, to find the different combinations to obtain a resonance frequency of 50 Hz. The dimensions of the magnets are more restrictive because they are defined by the manufacturer. A parametric study from 10 mm to 40 mm of Lm is performed. Table 1 shows the different dimension combinations obtained to achieve a resonance frequency of 50 Hz.

Table 1. Comparative with the different combinations of the parameters to obtain the fixed resonance frequency at 50Hz.

Lb (mm)	Lm (mm)	Lc (mm)	Ratio Lb/Lc (%)	Frequency (Hz)
41.20	10.00	51.20	80	50.04
33.10	15.00	48.10	69	49.95
26.80	20.00	46.80	57	50.02
21.60	25.00	46.60	46	50.00
17.15	30.00	47.15	36	50.01
13.35	35.00	45.35	29	50.05
10.20	40.00	50.20	20	49.99

3.2.2. Study of Generated Power

The voltage and power of the different dimensions are studied using an external circuit that includes a resistor. Performing a sweep of the external resistor, the optimal load resistor can be determined to achieve maximum power. As shown in Figure 3a, the lower ratio between Lb and Lc, the higher the power output. Furthermore, a smaller piezoelectric area is needed, leading to a decrease in device cost since PVDF is the most expensive material in the harvester.

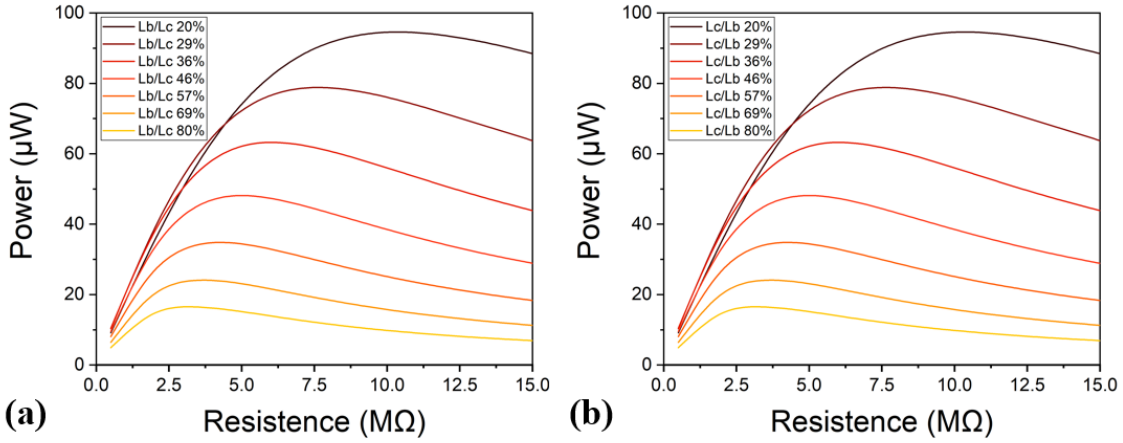


***Figure 3**. (a) Maximum power generated by the device with different Lc/Lb ratios; (b) Maximum power generated modifying the neutral axis of the beam increasing Tb and the density of the mass to maintain the same resonance frequency.*

A parametric thickness of the beam under the piezoelectric sheet was simulated to improve the power generated by the piezoelectric generator. Due to the increase in Lb, the natural frequency of the device increases. To compensate for this augment, the density or Tm must be raised. In this occasion, the density of the mass has been augmented to compensate for the frequency. In this way, the dimension of the mass is always the same and simplifies the meshing process during the simulation. As can be seen in Figure 3b, the greater Tb, the greater the power generated.

In the next Table 2, different Tm can be seen to compensate for the increased Tb. In addition, the data of the maximum generated power, volume and power density of each harvester obtained from the simulation are also shown.

Table 2. Comparative with the different thicknesses of mass to compensate for the increased thickness of the beam and data of the maximum power generated, volume and power density of each harvester.

Tb (mm)	Tm (mm)	Power (µW)	Volume (cm^3)	Power Density (µW/cm^3)
1.00	1.00	95	4.10	23.08
1.50	3.48	324	10.20	31.77
2.00	8.13	620	20.80	29.85
2.50	15.46	938	36.80	25.50
3.00	26.12	1261	59.60	21.15
3.50	40.40	1534	89.90	17.06

With the data obtained in the simulation shown in Table 2, the volume and cost of each harvester are calculated. As seen in Figure 4a, the cost and the volume of the harvester are closely related because most of the volume is mass. Furthermore, it can be seen how the highest power density is for a Tb of 1.5 mm.

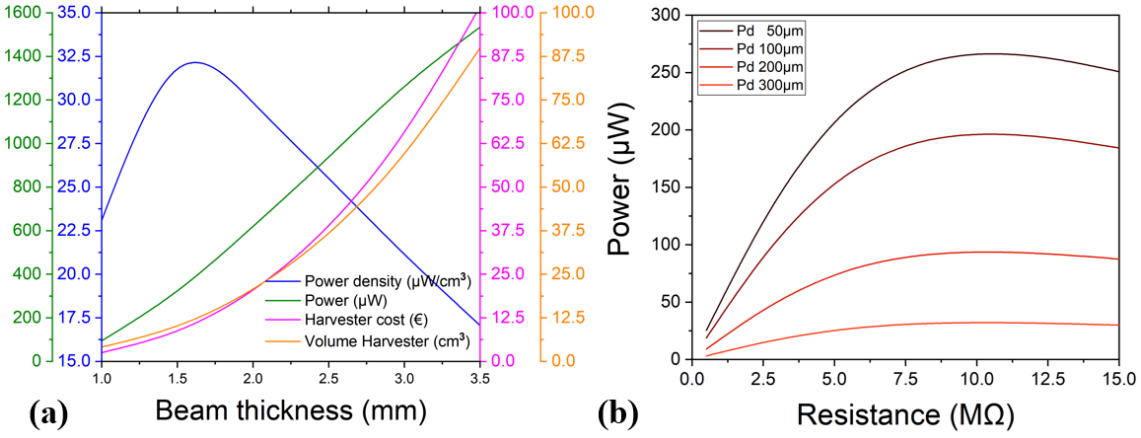


Figure 4. (a) Graphic of the maximum power generated, power density, harvester cost and volume of the harvester as a function of beam thickness; (b) Power curve generated by the harvester as a function of the depth of the piezoelectric material with respect to the surface.

Finally, a parametric simulation of the depth of the piezoelectric material regarding the surface has been performed. As can be seen in Figure 4b and as mentioned above in the design section. The closer the material is to the surface, the more power it generates since it is farther from the neutral line of the beam.

With the results obtained from the simulations, it can be concluded that the best specification for the harvester is the design with a dimension of 10.2 mm × 40 mm (Lc and Lm). In addition, to obtain a higher power density, the beam should be 1.5 mm thick and the piezoelectric material should be as close to the surface as possible.

3.3. Manufacturing Process

In 3D printing, as can be seen in Figure 5 the process begins with designing the desired piece using 3D design software (Tinkercard®, https://www.tinkercad.com), typically CAD software. Once the design is completed, the next step is exporting the file in STL (Stereolithography) format. The STL file contains all the necessary information about the 3D object. Subsequently, the CAD model is sliced into layers using slicing software Ultimaker Cura 4.13.1. Finally, the object is printed by transferring the file, positioning and printing the design layer-by-layer.

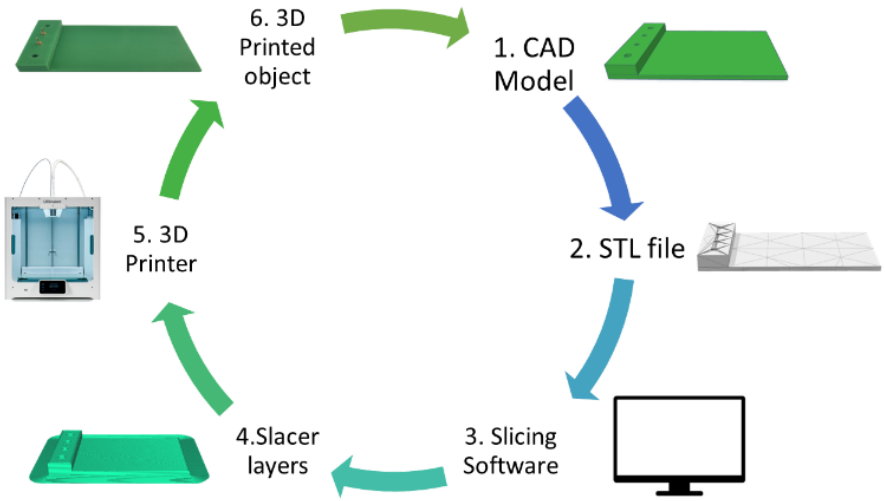


Figure 5*. Basic process of 3D printers to create 3D objects.*

Our manufacturing process is very similar to a typical 3D object; however, two additional steps are required to introduce the bottom electrode and the PVDF material. The first step, shown in Figure 6a, is the printing of the brim around the object to hold the edges of your piece and subsequently printing the layer that encapsulates the piezoelectric material within the structure. As previously mentioned in the generated power simulations, a thinner layer leads to greater power output. Since the minimum layer the nozzle can print is 60 µm, and to ensure good quality and avoid pushing the limits of the

printer head, it was decided to print two or three layers of 100 µm. It is crucial to maintain high quality in this layer because it contributes to the stress received by the piezoelectric material. Additionally, a hole is left on the material's surface to place the lower copper electrode.

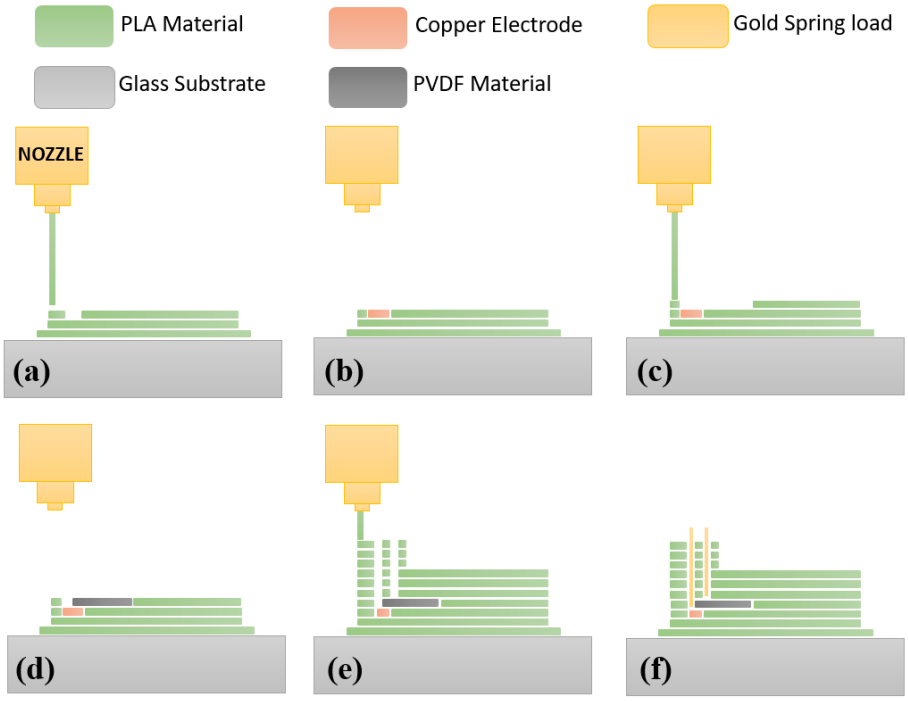


Figure 6. *(a) Schematic of our 3D printing process and the sequences of steps to create the device (a) PLA base layer printing for encapsulation of the piezoelectric material; (b) placement of copper material to make the connection of the bottom electrode; (c) PLA layer printing for later assembly of the piezoelectric material; (d) placement of the piezoelectric material (PVDF); (e) printing of the rest of the PLA structure leaving two holes for subsequent connections and (f) insertion of gold connectors for the connection of the two electrodes of the piezoelectric material.*

Subsequently, a copper piece is inserted to establish the connection with the bottom electrode, and the printing process continues depositing the piezoelectric material layer. At this point, the printing process is paused again to add the piezoelectric material, followed by the printing of the remaining structure. During this final stage of the printing, the rest of the beam and support with two holes to secure the harvester are created. Upon completing the print, gold connectors are inserted to facilitate the connection between the two electrodes of the piezoelectric material. In Figure 7, it can be seen the images of the steps of our 3D printing process to create the harvester. Three harvesters

were manufactured with the piezoelectric material at 200 µm from the surface and other three devices with 300 µm.

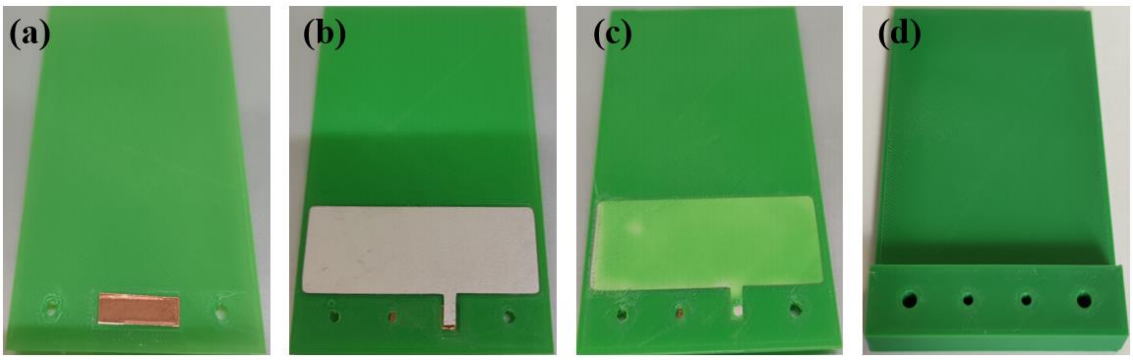


Figure 7. *Images of steps of our 3D printing process to create the harvester (a) PLA base layer printing for encapsulation of the piezoelectric material and placement of copper material to make the connection of the bottom electrode; (b) placement of the piezoelectric material; (c) next layer printed after the placement of the PVDF to see how it is encapsulated and (d) printing of the rest of the PLA structure leaving two holes for subsequent connections.*

3.4. Characterization

3.4.1. Electrical Characterization

Once the harvesters are manufactured, we proceed to the electrical characterization of our final devices. Two electrical characterizations have been conducted. The first characterization, shown in Figure 8a, involves a stepper motor that performs movements from 1 mm to 6 mm of distance on the Z-axis. Simultaneously, the voltage generated by the harvester is measured using a Sourcemeter. A force sensor, attached to the stepper motor, records these data through a dynamometer. An ad-hoc LabVIEW® program controls all the setup comprising these devices. As can be seen in Figure 8b, a displacement of 6 mm along the Z-axis results in an average voltage of 71.7 V for the harvester with the piezoelectric material positioned 300 µm far from the surface. Reducing the distance of the piezoelectric material from 300 µm to 200 µm increases the average voltage to 85.2 V, representing a 19% increment in the maximum voltage generated. According to the force data represented in Figure 8c, the depth of the piezoelectric material does not affect the force needed to achieve 6 mm of travel at the tip of the cantilever.

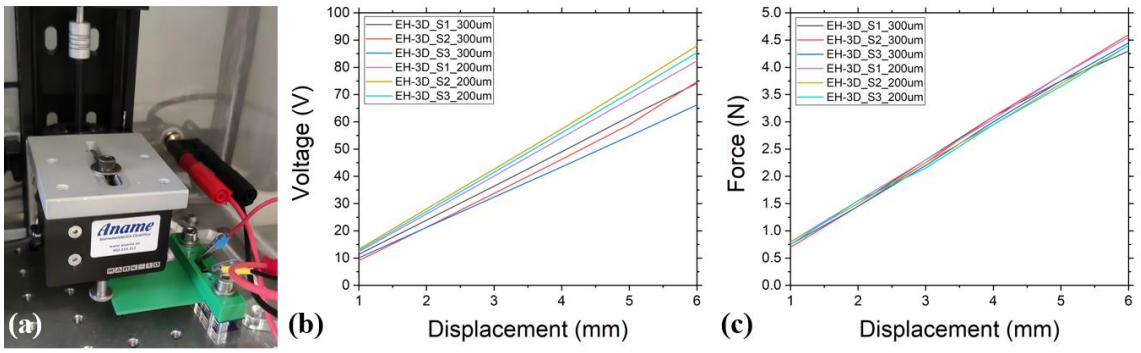


Figure 8. *(a) Setup for electrical characterization using a stepper motor, sourcemeter and dynamometer; (b) Maximum voltage achieved with a displacement of the stepper motor from 1 mm to 6 mm of distance on the Z-axis and (c) Force measured with a displacement of the stepper motor from 1 mm to 6 mm of distance on the Z-axis.*

For the second electrical characterization, as can be shown in Figure 9a, a magnetic mass is attached to adjust the resonance frequency to 50 Hz. An electrodynamic shaker is used to emulate environmental vibrations at different input acceleration levels. This is controlled through an ad-hoc MATLAB® program that allows automatizing, acquiring and processing the voltage measurements. All these data are captured by an acquisition system. Subsequently, fixing a certain acceleration magnitude, a sweep of load resistors values is performed. This allows us to determine the optimal load resistor value for the highest generated power.

Due to the voltage limitations of the acquisition system, which cannot measure voltages exceeding 10 V, the load resistance sweep is initially carried out with a small acceleration of 0.1 G, ensuring that it remains below 10 V. Figure 9b shows that the optimal load resistance for maximum power generation is 4 MΩ, resulting a maximum power of 4.4 µW.

Once the optimal load resistance is known, use a voltage divider, composed of a set of 500 KΩ and 3.5 MΩ resistors. It is possible to measure the voltages generated by harvesters with accelerations greater than 0.1 G.

The voltage generated by the piezoelectric generator was measured while performing an acceleration sweep ranging from 0.1 G to 1 G, as shown in Figure 9c. For an acceleration of 1 G, the harvester with the piezoelectric material positioned 300 µm from the surface

achieved an average voltage of 62.3 V. By reducing the distance of the piezoelectric material to 200 µm, an average voltage of 75.6 V is achieved, resulting in a 21.4% increase in the maximum voltage generated. Using the aforementioned voltage data, the maximum power for the different accelerations was calculated and plotted in Figure 9d. It can be observed that reducing the difference between the two depths of the piezoelectric material resulted in an increase of up to 47.3% in the maximum power generated. This led to a maximum output power of 1.46 mW.

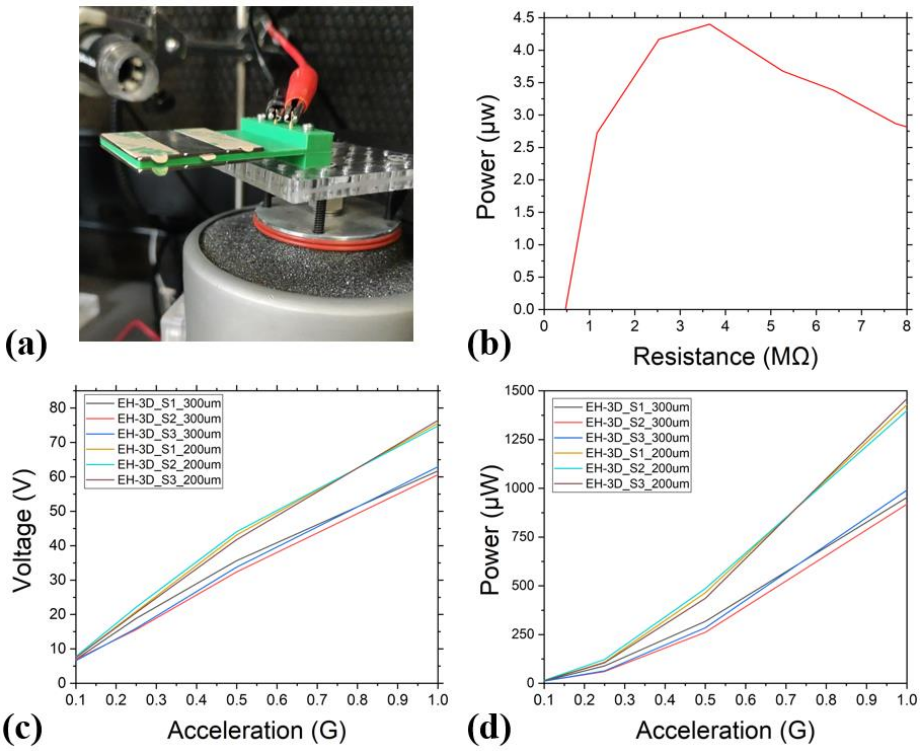


Figure 9. (a) Setup for electrical characterization using an electrodynamic shaker; (b) Optimal load resistance for maximum power generation with 0.1 G of acceleration; (c,d) Voltage and maximum power for an acceleration sweep from 0.1 G to 1 G and using a frequency of 50 Hz and an optimal load resistance of 4 MΩ.

3.4.2. Physical Characterization of PVDF Material

An inspection using a scanning electron microscope (SEM) was performed to validate the thickness of materials provided by the manufacturer and, as can be seen in Figure 10a, the measured thickness closely matches the specifications.

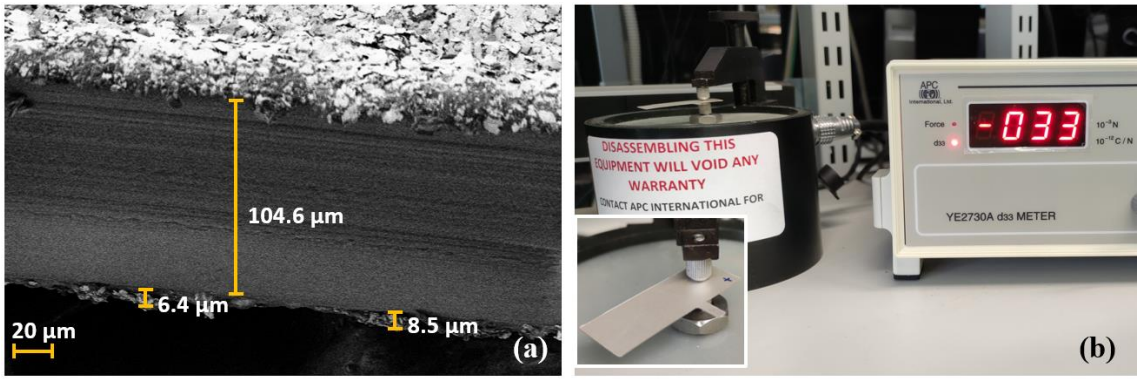


Figure 10. *(a) SEM image of the thicknesses of the layers of the piezoelectric material; (b) Image of the measurement of the piezoelectric coefficient.*

Using a piezometer, we can measure the exact coefficient of our PVDF piece. As shown in Figure 10b, the coefficient is the same as the manufacturer's specifications.

3.4.3. Material Measurement of Young's modulus of our Harvester

The Young's modulus of the used PLA is 2.8 ± 0.15 GPa, as stated in the technical datasheet. When introducing a material within the PLA, the overall effective Young's modulus can be changed. Therefore, the Young's modulus of the harvesters will be calculated based on the force data measured with a stepper motor displacement from the previous section.

A displacement of a cantilever beam δ is related to the applied load, *P* and the Young modulus, *E* by the next Equation (4):

$$\delta = \frac{1}{3}\frac{\mathrm{PL}^3}{\mathrm{EI}}, \tag{4}$$

where *L* is the length of the cantilever, and *I* the second moment of area (moment of inertia).

For a prismatic beam with a rectangular section (depth h and with w) the value of the second moment inertia of cantilever beam *I* is given by:

$$I = \frac{wh^3}{12} = \frac{0.04\ m\ x\ 0.0015\ m^3}{12} = 11.25x10^{-12}\ m^4, \quad (5)$$

From Equation (4) and using the force data measured with stepper motor displacement, the Young's modulus of harvesters is calculated:

$$E = \frac{1}{3}\frac{PL^3}{\delta I} = \frac{4.5\ N\ x\ 0.05\ m^3}{3\ x\ 0.006\ m\ x\ 11.25x10^{-12}\ m^4} = 2.78\ GPa, \quad (6)$$

From Young's modulus obtained from the above Equation (6), it can be seen that the modulus is within the manufacturer's specifications and that the piezoelectric material has little effect on the final Young's modulus of the harvesters.

3.5. Finite Elements Simulation

The energy harvesters were simulated again with COMSOL Multiphysics® to compare the results of the electrical characterization with a theoretical model. Physical parameters such as Young's modulus, thickness, coefficient of the piezoelectric material, and harvester dimensions were included in the simulation to achieve a realistic representation.

A parametric sweep ranging from 48 Hz to 54 Hz was performed to determine the resonance frequency of the resonators with an optimal load resistance of 4 MΩ. The acceleration used for this simulation was 0.5 G. It can be seen, in Figure 11a, the resonance frequency for the COMSOL Multiphysics® harvesters was approximately 50.5 Hz, while for the electrical characterization of the manufactured harvesters yielded a resonance frequency of 49.5 Hz. Initially, the harvesters were tuned to resonate at 50 Hz with an acceleration of 0.1 G. However, due to spring softening with increasing acceleration, the resonance frequency is shifted from 0.5 Hz to 49.5 Hz.

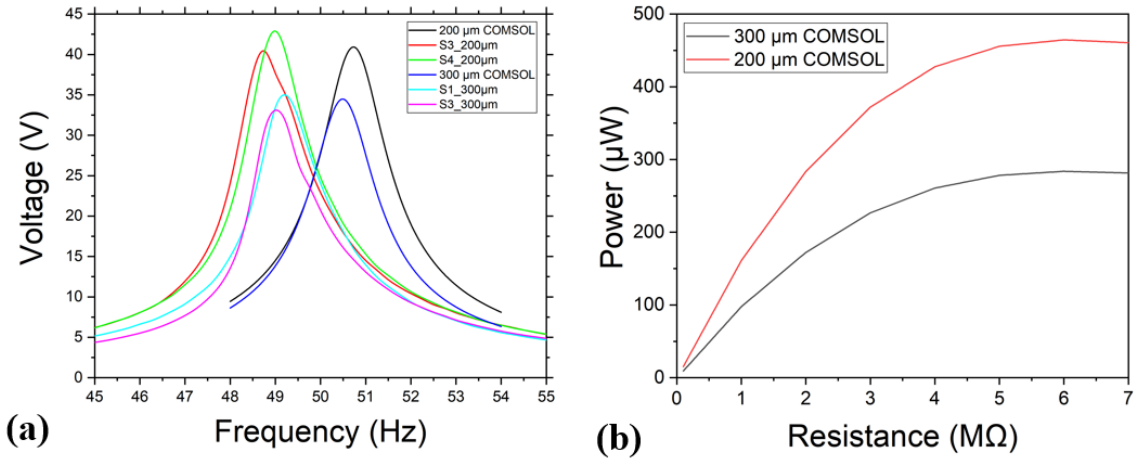


***Figure 11**. Simulated results of the piezoelectric device by using COMSOL Multiphysics®: (a) Comparative of simulation and electrical characterization of the maximum open-circuit voltage that can be generated by the piezoelectric generator submitted to a frequency sweep with an acceleration of 0.5 G; (b) A comparison of the maximum power generated in relation to the depth of the piezoelectric material and the load impedance.*

As in the electrical characterization with the shaker, a sweep of the load resistance is performed to calculate the maximum power. As shown in the Figure 11b, the maximum power generation is around 5 MΩ, with a maximum power of 283 µW for the harvester with a 300 µm distance of the piezoelectric material and 464 µW for the 200 µm distance. These values are very similar to the maximum powers measured in Figure 9c, with 288 µW and 462 µW, respectively.

3.6. Example of Application

As mentioned earlier, the energy harvester can be customized using CAD software (e.g. (Tinkercard®, https://www.tinkercad.com) to adapt its specifications for various application scenarios. An example application for our device would be its use as a sensor rather than an energy harvester. In this particular case, it can be employed to measure the current flowing through a wire in a high-voltage tower. When an electric current passes through the wires, it generates a magnetic field that is directly proportional to the current flowing through the wire. By using the magnetic mass, our device can be made to resonate, and depending on the current it passes, we can measure an instantaneous proportional voltage in our sensor.

In this example application, the maximum dimensions for the sensor are 30 mm × 20 mm with a height of 10 mm. The resonance frequency for this resonator is the same as the frequency of the current flowing through the wire being measured, which is 50 Hz. The magnets for the magnetic mass have dimensions of 10 mm × 10 mm and a thickness of 2.7 mm. The support will be fixed at dimensions of 20 mm × 10 mm and a height of 10 mm to ensure good anchoring and easy fastening. A simulation is performed to obtain the resonance frequency at 50 Hz. As shown in Figure 12a, measurements of 12 mm × 20 mm and a thickness of 700 µm for the cantilever beam are obtained. Two magnets will be required for the magnetic mass. Figure 12b shows the stress distribution in the beam when the cantilever is resonating at an acceleration of 0.1 G.

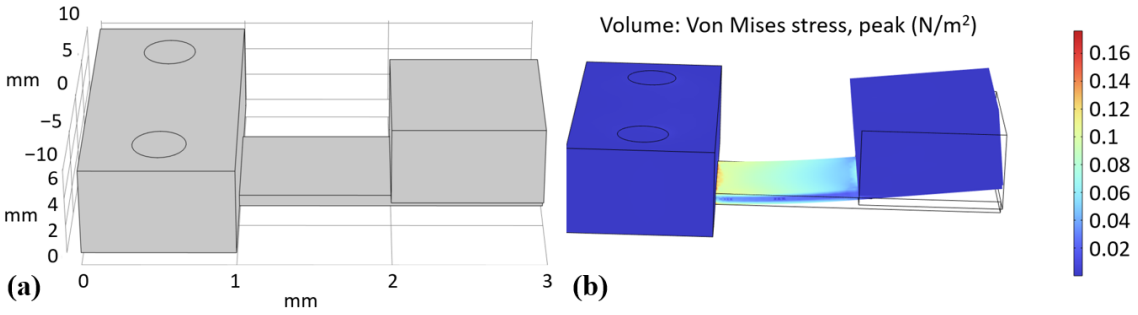


Figure 12*. Simulated results of the piezoelectric current sensor by using COMSOL Multiphysics®: (a) Structure and dimensions used in the simulation; (b) 3D FEM simulation of the stress distribution in the cantilever beam.*

As can be shown in Figure 13a,b, the simulated sensor is mounted inside a sensor node provided by the startup company Energiot Devices SL (www.energiot.com). To test the sensor in the laboratory, two heaters with two power selections have been connected. This setup allows for the generation of four different currents depending on the selected power: 1500 W (6.5 A), 3000 W (13 A), 4500 W (19.5 A) and 6000 W (26 A). As can be seen in Figure 13c, the different current cases passing through the cable can be measured using the corresponding voltage readings, demonstrating a linear response.

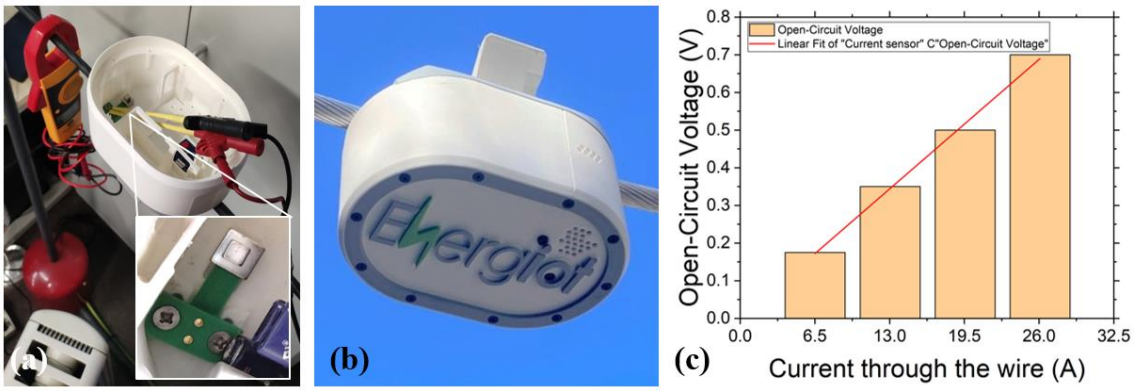


Figure 13. *(a,b) Piezoelectric current sensor manufactured using 3D printing technology mounted inside a sensor node from the start-up Energiot; (c) Open circuit voltage generated by the piezoelectric sensor, depending on the selected power of two heaters, which can obtain up to four different currents (1500 W, 3000 W, 4500 W and 6000 W).*

Furthermore, the magnetic field can also be used to power wireless sensors that measure various parameters such as magnetic field, ambient and line temperature, acceleration, tilt, humidity and light intensity and transmit the gathered information to the cloud.

4. Conclusions

In this article, we designed, manufactured and electrically characterized a resonant piezoelectric energy harvester by exploiting 3D printing technology and encapsulating PVDF within the structure, resulting in a monolithic harvester. With this, an economically viable energy harvester was achieved that mechanically improves the anchoring of the resonator thanks to its structure attached to the fixing support. The device was optimized through the finite element simulation software COMSOL Multiphysics® 6.0.

Furthermore, we demonstrated an example of the practical application of our resonator by designing and fabricating a specific use case for measuring the current passing through a wire using magnetic fields. Through 3D printing, not only did it enable the manufacturing of a compact and monolithic harvester but also facilitated the customization and optimization of the device for specific requirements.

Overall, this work contributes to the advancement of piezoelectric energy harvesting technology by providing a practical approach to designing and manufacturing resonant

harvesters using 3D printing. The demonstrated use case application shows the potential to use such devices in a myriad of real-world scenarios.

Finally, this article represents a small contribution to the ongoing trends and future sustainability of self-powered sensors. By harvesting ambient energy, self-powered sensors have the potential to reduce the environmental impact associated with batteries. Furthermore, current advancements are paving the way for more efficient and reliable self-powered sensors. However, further research and development are needed to overcome challenges such as energy conversion efficiency and long-term reliability improvement.

Author Contributions: Conceptualization, M.D. and G.M.; methodology, M.D. and G.M.; investigation, M.D. and G.M.; writing—original draft preparation, M.D.; writing—review and editing, G.M.; supervision, G.M. All authors have read and agreed to the published version of the manuscript.

Funding: This research was funded by La Caixa Foundation under the Junior Leader Retaining program (LCF/BQ/PR19/11700010), and EUR2020-112082 under the Dynamization Actions "Europa Excelencia 2020" funded by the NextGenerationEU Instrument.

Institutional Review Board Statement: Not applicable.

Informed Consent Statement: Not applicable.

Data Availability Statement: Data are contained within the article or Supplementary Material.

Acknowledgments: G. Murillo thanks the financial support from the La Caixa Foundation under the Junior Leader Retaining Fellowship (LCF/BQ/PR19/11700010), the Agencia Estatal de Investigación from Spanish Government (PID2020-119350RA-I00, MICROBIO project) and project EUR2020-112082 under the Dynamization Actions "Europa Excelencia 2020" funded by the NextGenerationEU Instrument. In addition, this work also received support by Generalitat de Catalunya-AGAUR (2021 SGR 00497). This work has been carried out in collaboration with ENERGIOT DEVICES SL (www.energiot.com) and in

the framework of the doctoral program in Electronic and Telecommunication Engineering of the Autonomous University of Barcelona.

Conflicts of Interest: The authors declare no conflict of interest.

3.3 Piezoelectric MEMS resonator with magnetic tip mass for energy harvesting from ultra-low intensity magnetic field

Piezoelectric MEMS resonator with magnetic tip mass for energy harvesting from ultra-low intensity magnetic fields

Marcos Duque[1] and Gonzalo Murillo[1*]

[1]Instituto de Microelectrónica de Barcelona, IMB-CNM (CSIC), Til·lers s/n, Campus UAB, Bellaterra, 08193, Spain;

Abstract

This article addresses the limitation in the implementation of the Internet of Things (IoT) due to its energy dependence on batteries. The central focus of this work is the development and characterization of a magnetoelectric (ME) energy generator for IoT, which combines a piezoelectric microelectromechanical system (MEMS) with a magnetic mass to interact with ambient magnetic fields (MFs). The device's efficiency is validated through finite element modelling (FEM) simulations and electrical characterization. Its applicability in environments with residual magnetic fields, such as near common household appliances, highlights its viability. Specific results, such as a maximum generated power of 0.55 µW, corresponding to a power density of 9.19 µW/cm^3, for a magnetic field strength of 5 µT, emphasize its ability to address energy challenges and promote the sustainable autonomy of IoT.

1. Introduction

In the recent decades, Internet of Things (IoT) has experienced an extraordinary growth, emerging as a revolutionary interconnected network spanning from household devices to complex industrial infrastructures [1, 6, 211–213]. However, as the IoT has become more deeply integrated into our daily lives and various industrial sectors, the attention has been focused on crucial challenges threatening its sustainable expansion. One of the most prominent obstacles is the energy dependence on batteries in IoT devices, leading to significant limitations in terms of lifespan, maintenance, and associated costs. This issue in the context of IoT has prompted an active search for innovative solutions, and in this context, energy harvesting (EH) has emerged as a promising field. EH offers the possibility of freeing IoT from its reliance on traditional energy sources, providing a sustainable and autonomous power source. This approach, leveraging various ambient energy sources, presents a paradigm shift in how we conceive the powering of IoT devices and, therefore, has the potential to catalyze a new era of expansion and efficiency in this interconnected network [21–23, 214].

Various environmental energy sources, such as thermal, light, electromagnetic (EM), radiofrequency (RF), mechanical, and chemical energy, can be harnessed for energy harvesting and IoT implementation [*142*]. EM energy harvesting is attractive for most IoT applications due to the ubiquitous availability of EM radiations and wireless communications. Depending on the size and scope of the application, near-field or far-field radiations are used. In the near field, magnetic fields (MF) and EM are induced to generate electrical power and wirelessly power devices [215–217].

Research in the field of piezoelectric materials has been fundamental for the advancement of various technologies in disciplines ranging from electronics to medicine. These materials exhibit the unique property of generating an electric field in response to mechanical stress and, in the other way around, a deformation is created when applied an electric potential. This dual functionality, known as the piezoelectric effect, has driven a wide range of innovative applications and led to the design and development of highly efficient electromechanical devices. The convergence of piezoelectric and magnetic materials has generated a promising research area in the EH domain. In this context, the

fundamental concept lies in applying mechanical stresses to piezoelectric materials through interaction with magnetic fields. The ability of these materials to respond to magnetic forces coupled with their inherent ability to convert that response into electrical energy, represents a promising approach to addressing power challenges in autonomous devices and distributed sensor systems.

In ME energy harvesting with piezoelectric materials, most applications rely on the use of MF with magnitudes on the order of militeslas. These MFs, essential for power generation, are commonly found in environments where a significant current flows through conductors, such as in transmission and distribution lines and associated transformer stations [218–221]. However, when venturing into more everyday environments, such as homes, offices, or industries, a significant reduction in the intensity of magnetic fields is encountered. In these places, MF typically decreases by approximately an order of magnitude, reaching microteslas levels [222–224]. This decrease poses a significant challenge when seeking to harness this weaker MF for energy harvesting intended for use in IoT sensor applications. While applications in environments with more intense currents offer promising opportunities, a more innovative and efficient approach is needed to harness microteslas present in everyday environments. This technical challenge represents an active research area, as overcoming these limitations would enable the more widespread implementation of EM energy harvesting technologies in a variety of contexts.

This work focuses on the development of a piezoelectric generator designed to capture residual EM energy from the environment, specifically in the microteslas range, and convert it into usable energy. To achieve this purpose, a piezoelectric MEMS is employed as a transducer, and a magnetic tip mass is integrated for interaction with magnetic fields. The first phase of the work concentrates on the fabrication of the MEMS resonator and the integration of the magnetic mass. The second part of the study focuses on the electromechanical characterization of the device. Additionally, a specific application example is presented to illustrate the potential and practical viability of this device in the real world.

2. Experimental Section

2.1. Finite Element Simulation

In this study, COMSOL Multiphysics® software is employed to investigate the electromechanical behavior of a MEMS resonator and the impact of adding a magnetic tip mass. COMSOL Multiphysics®, a versatile simulation software, utilizes the finite element modelling (FEM) to solve partial differential equations in scientific and engineering systems. A 3D model of the different layers with the specific layout used for the fabrication was created. The sparse direct massively parallel multifrontal solver (MUMPS) was chosen to obtain the numerical solution in the stationary solver. Then a thin mesh with anisotropic density was utilized to model the mechanical structure. For the piezoelectric material, a sweep meshing was specifically performed, with more than 45,000 elements for the piezoelectric material and a tetrahedral meshing for the rest of the structure, consisting of more than 209,000 elements. The structural mechanics and electrostatic physics were employed, together with the piezoelectric module. For the piezoelectric material, AlN, a density of 3300 Kg/m3, a relative permittivity of 9, and a piezoelectric coefficient of 4.96 pC/N were used. In order to evaluate the resonance motion and the piezoelectric potential generated, the MEMS Module, which allows to predict the structural, electrical, and thermal performance of MEMS devices, was used.

2.2. MEMS Manufacturing Process

The functional schematic of our MEMS piezoelectric energy harvester is depicted in Figure 1a. The construction of our energy harvesting devices is based on a silicon-on-insulator (SOI) substrate with the following thicknesses of the different layers: silicon: 15 µm — SiO2: 1 µm — bulk silicon: 500 µm [225–228]. The device layer is utilized to define the cantilever beam, while the bulk layer is employed for the inertial mass (Figure 1b). On the cantilever beam, a 1 µm-thick layer of aluminum nitride (AlN) serves as the piezoelectric transducer. This piezoelectric layer is sandwiched between two identical bilayered metallic electrodes of Ti/Pt with thicknesses of 20 nm and 200 nm, respectively. Since, in most applications, the frequency of ambient vibrations is below 1 kHz, an inertial tip mass has been integrated to reduce the natural resonance frequency of the structure.

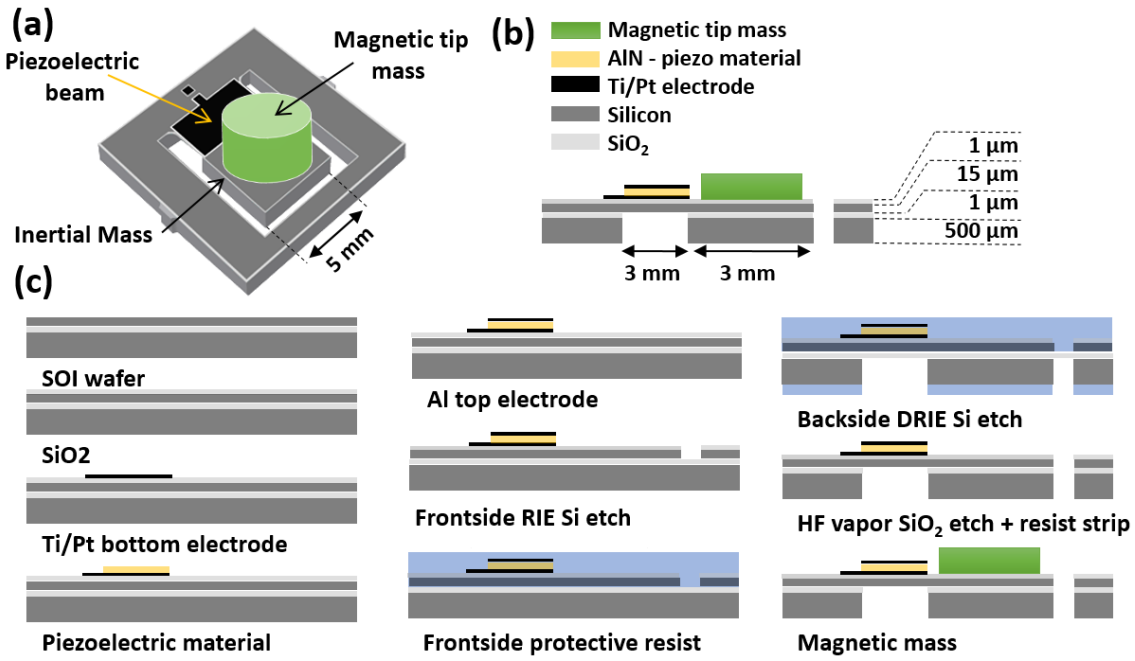


Figure 1: *(a) Schematic of the functional configuration of the device with a cantilever structure and a magnetic tip mass, (b) cross-sectional diagram of the cantilever structure, and (c) different stages of the manufacturing process are included.*

The fabrication process of our device is outlined in Figure 1c. Both Ti/Pt layers are deposited through RF reactive sputtering to define the two electrodes of the device. The same technique is employed to deposit the 1 µm-thick AlN layer. The device structure is configured through several photolithography steps and deep reactive ion etching (DRIE). Upon completion, a wet etching process based on hydrofluoric acid (HF) is employed to remove part of the buried oxide layer, subsequently releasing the cantilever beam. In this study, our focus is on the PEH-B3X5M3X5 device, presented in Figure 1a, with a tip mass area of 3 mm × 5 mm and a cantilever area of 3 mm × 5 mm.

Following the completion of the microfabrication process, a neodymium magnetic mass with a diameter of 3 mm and a thickness of 2 mm is inserted. Initially, an epoxy layer is applied to one face of the magnet, and then it is precisely positioned on top of the silicon tip mass, using a pick-and-place machine.

2.3. Electrical characterization

The electrical characterization was conducted with an experimental setup including an electrodynamic shaker (VR9500 Vibration Test Controller) to emulate ambient vibrations

with different acceleration magnitudes. A high-impedance acquisition system (National Instruments PCI-6132 and BNC-2110) with an input impedance of 100 MΩ was used to measure the generated voltage. The device under test (DUT) was connected and mounted through a pick-and-place machine onto a specifically designed PCB, providing physical support and electrical connection.

2.4. Characterization under controlled magnetic fields

The characterization under controlled magnetic fields was conducted with a pair of Helmholtz coils designed to emulate linear alternate-current (AC) magnetic fields (MF) of up to 1 mT. An ad hoc program developed in MATLAB® controlled a function generator (Tabor® electronics WW1071), allowing the adjustment of the frequency and amplitude of the EM field. The same acquisition system as in the previous section was used to measure the generated voltage. An EM field meter (LUTRON® EMF-827) was used to verify the magnetic field strength, and a digital microscope was employed to capture the movement of the resonator (Figure 4f).

For the application example using magnetic fields, a high-voltage line conductor is used (ACSR 1/0 AWG Raven). This conductor is composed of an aluminum wire (H1350-H19) wound around a Class A galvanized steel core, with a total diameter of 10.1 mm and capable of supporting currents of up to 242 A.

3. Results and Discussions

3.1. Finite Element Simulation

Various structural configurations are utilized for piezoelectric energy harvesting devices, with the cantilever, circular diaphragm, and cymbal being the most prevalent. Among these options, the cantilever stands out for its ability to provide the highest energy output as a piezoelectric harvester. Moreover, the cantilever structure achieves a lower resonance frequency for a given size. Consequently, the cantilever structure was chosen for this work.

The initial study focuses on comparing the MEMS resonator with and without a magnetic tip mass to observe how its behavior changes in terms of resonance frequency and optimal impedance of the piezoelectric resonator. This tip mass plays a crucial role in

adjusting the resonance frequency to the standard frequency of 50 Hz of European AC electric grid (60 Hz in USA). Additionally, it will be utilized for the mentioned ability to interact and harness the ambient magnetic field, inducing a resonance motion in the device.

The resonance frequency (f_r) and optimal impedance (Z_{opt}) of a piezoelectric resonator are influenced by various parameters, including the resonator mass (m). These parameters are interrelated and can be described by specific equations. The resonance frequency f_r of a piezoelectric resonator can be described by the following equation, following a simple spring-mass model:

$$f_r = 2\pi \sqrt{\frac{k}{m}}$$

Where *k* is the effective stiffness constant of the cantilever materials and *m* is the equivalent mass.

On the other hand, the optimal impedance (Z_{opt}) connected to a cantilever for maximum power transfer is related to the resonance frequency (f_r) and the internal capacitance (C_p) of the piezoelectric material by the equation [229]:

$$Z_{Opt} = \frac{1}{2\pi f_r C_p}$$

From the previous equations, it can be concluded that as the mass m increases, the resonance frequency f_r tends to decrease. Additionally, the optimal impedance Z_{opt} will also be affected by the increase in mass, as it is directly related to it.

The same MEMS device is simulated with and without a magnetic mass to compare the changes in resonance frequency f_r and optimal resistance Z_{opt}, yielding the following results shown in Figure 2 a-d.

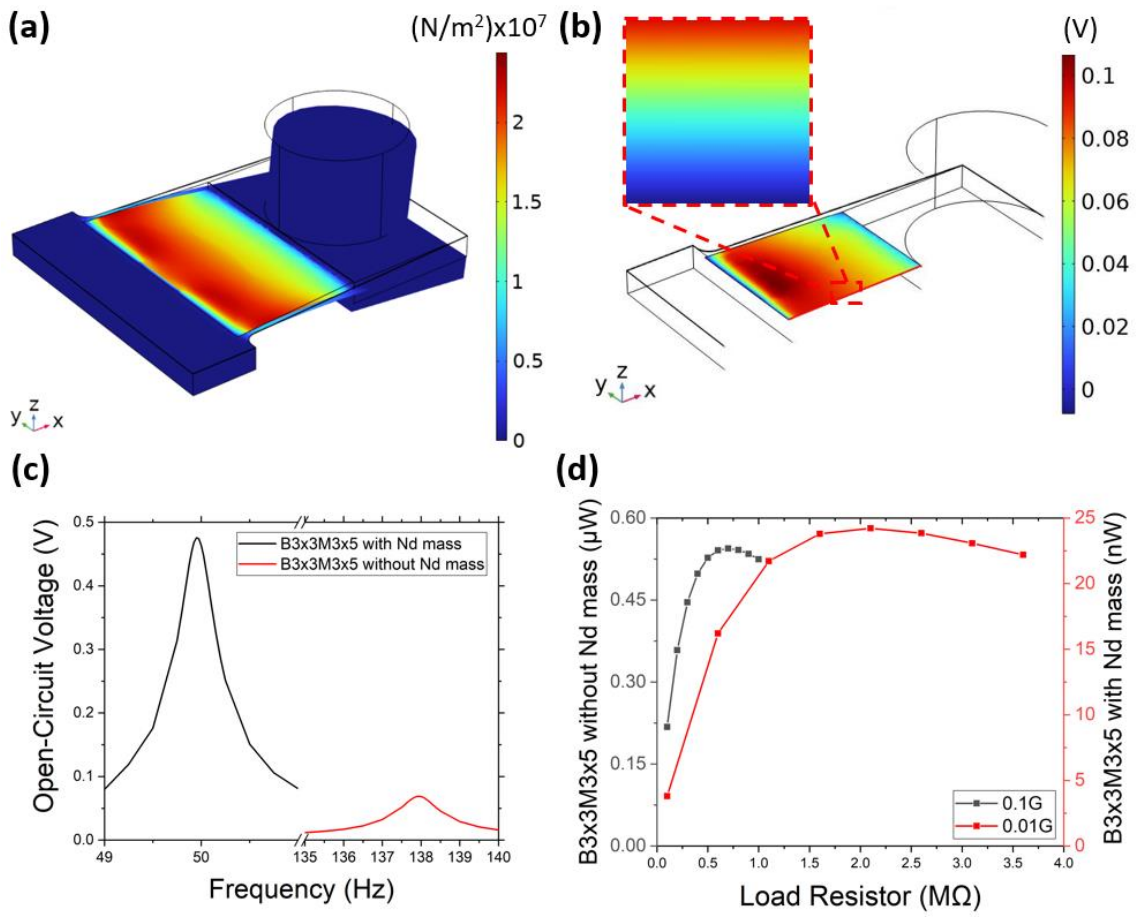


Figure 2: *Model of the simulated piezoelectric resonator using COMSOL Multiphysics® to assess the resonance frequency and displacement both without (a) and with mass (b). The graphical representation displays the simulation results of the tip displacement and the open-circuit voltage (c), as well as the maximum generated power with the optimal load impedance of the simulated structures.*

From the simulations conducted previously using COMSOL Multiphysics, as shown in Figure 2b, the frequency of the first resonance mode shifts from 138 Hz to 50 Hz upon adding a cylindrical neodymium mass with a diameter of 3 mm and a thickness of 2 mm. The second, third, and fourth modes of resonance are at 285 Hz, 496 Hz and 13353 Hz, respectively. As mentioned earlier and as shown in Figure 2c, increasing the mass decreases the resonance frequency and, in turn, increases the displacement amplitude. Additionally, as shown in Figure 2d, its optimal impedance increases from 500 KΩ to 2 MΩ. The maximum generated power, for an acceleration magnitude of 0.2 G at 50 Hz, shows a decrease, which was an expected outcome due to its inversely proportional dependence on the optimal load impedance. In this case, a greater importance is given

to the resonance frequency, as the primary goal of this work is to adjust it to the 50 Hz of the ambient magnetic fields.

3.2. Structural and compositional analysis

An inspection was conducted using scanning electron microscopy (SEM), as shown in Figure 3a, to examine the piezoelectric layer of AlN. The results revealed that AlN exhibits a columnar structure, with a layer thickness of 994 nm. Additionally, it can be observed the top electrode composed of two adjacent layers, made of Ti and Pt, with thicknesses of 20 nm and 200 nm, respectively.

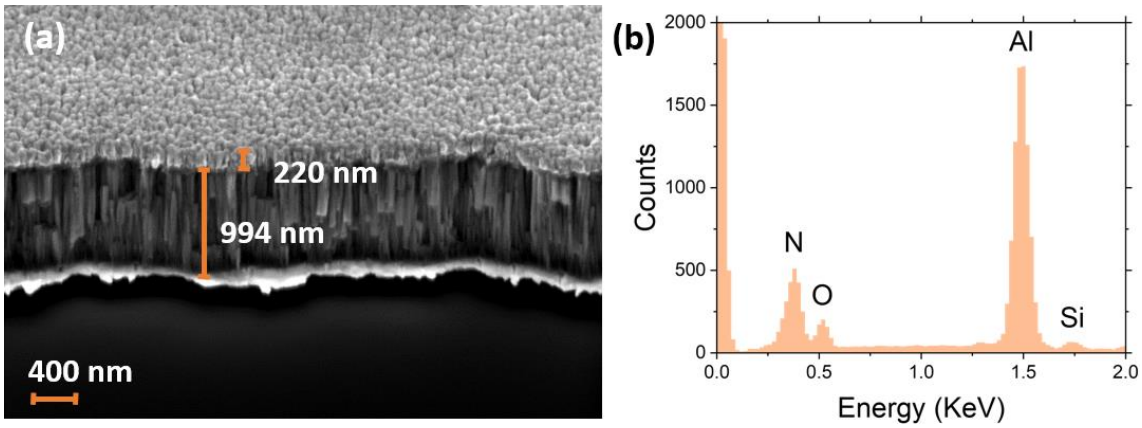


Figure 3: (a) SEM Inspection and (b) EDX Analysis Results of Aluminum Nitride (AlN) Piezoelectric Material and Electrode Composition.

To complement this analysis, energy-dispersive X-ray spectroscopy (EDX) was performed. Figure 3b indicates the presence of characteristic peaks of aluminum and nitrogen. Peaks corresponding to Pt and Ti from the electrodes were also identified. Furthermore, the presence of silicon and oxygen was detected, indicating the existence of a layer of silicon dioxide under the bottom electrode, as expected from fabrication process. These results provide valuable information about the composition and structure of the piezoelectric device under test.

3.3. Electrodynamic characterization

To validate the operation of the piezoelectric resonator, two electrical characterizations are performed using two different types of ambient sources. Firstly, by emulating ambient vibrations using an electrodynamic shaker (Figure 4a).

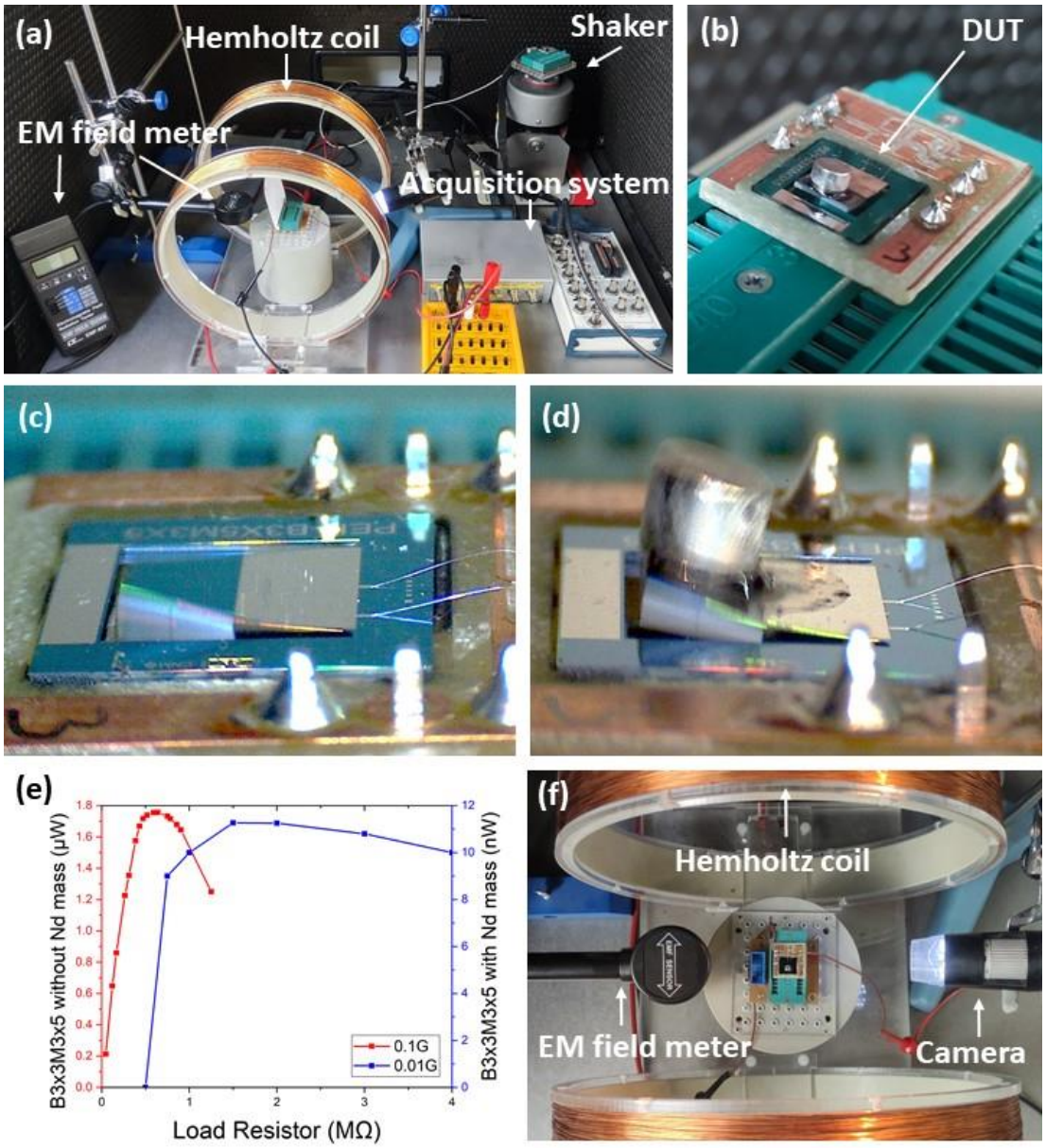


Figure 4: *(a) Electrical characterization setup used for ambient vibration emulations with the shaker and for magnetic field emulations with the Helmholtz coils. (b) Image of the device mounted on the PCB designed specifically to serve as mechanical support and electrical connection. Devices at resonance for an acceleration of 0.1 G in the case without magnetic tip mass (c) and 0.01 G in the case with magnetic tip mass (d). (e) Graph of the maximum power generated for devices at resonance with the optimal load impedance of the device. (f) Top view image of the device mounted between both Helmholtz coils during the characterization using magnetic fields.*

To perform the characterization, a frequency sweep is carried out to identify the resonance frequency of the resonator. Once the resonance frequency is determined, a load resistance sweep is performed to find the optimal impedance and maximum power

that the piezoelectric resonator can generate. To compare the data obtained in simulations with the results measured in the laboratory, the electrical characterization of the resonator is initially conducted before incorporating the magnetic mass. Then, the neodymium magnetic mass is attached, and the measurements are repeated. Figure 4c and d show the device resonating at its resonance frequency before and after adding the magnetic tip mass. These frequencies are 134 Hz and 50 Hz, respectively.

As observed in the graph of Figure 4e and confirmed by the results of simulations with COMSOL Multiphysics®, when the resonator does not have the neodymium mass, its optimal impedance is much lower, 500 kΩ, and its maximum generated power is 1.73 µW compared to the later obtained 2 MΩ, with a power of 11.5 nW. Therefore, the final power generated for the same displacement amplitude is lower. It is important to highlight again that, for our application, it is crucial that the device operates at 50 Hz, as this is the predominant frequency in many of the MFs present in the environment.

3.4. Characterization under controlled magnetic fields

For this measurement, the device was mounted between the two coils, using a specifically designed PCB that provided physical support and electrical connection, as shown in Figure 4b. A load resistance sweep at the resonance frequency of the device was carried out to measure the maximum power generated in MF ranging from 2.5 µT to 5 µT. With 5 µT, a maximum voltage of 1.51 V was obtained, corresponding to a maximum power of 0.55 µW with an optimal load impedance of 2 MΩ. Due to the compact size of our device, the possibility of placing several of these devices in parallel as an array would allow multiplying the power by a factor depending on the number of devices used. Additionally, by using a charge pump, it would be feasible to increase the maximum generated voltage if the final application requires it [230].

3.5. Example application

In the literature, various examples can be found where low intensity residual MFs are exploitable by our energy harvester. Beneath high-voltage power lines, on the walls of transformer buildings, and in the vicinity of transformer substations, values of up to 20-80 µT can be reached [231]. Underground cables of 400 kV can produce a magnetic field

intensity of over 30 µT at ground level, decreasing to 10 µT at 2 meters above the ground [232]. In public transportation such as metro stations, trains, and high-distance trains, values between 5.4 µT and 7.9 µT are obtained [233, 234]. Additionally, most household appliances generate MFs that are usable for our device. According to the literature, fields ranging from 2.5 µT to 1500 µT can be found at a distance of 3 cm [235].

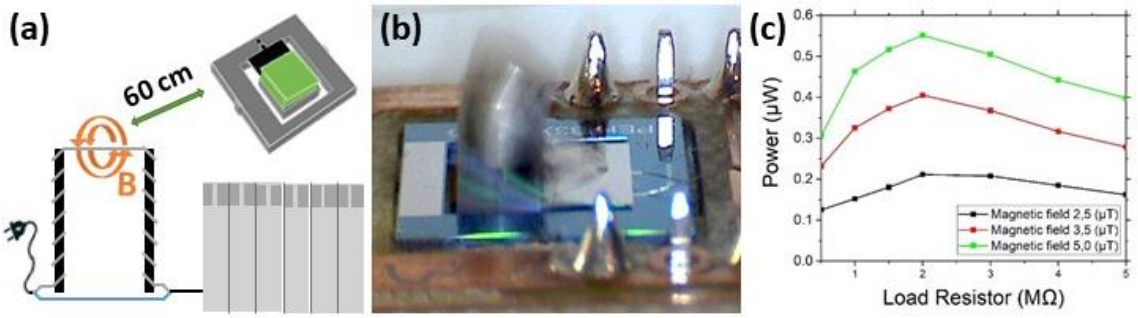


Figure 5: *(a) Diagram of the measurement of the application example involving two stoves and using the magnetic field generated by the current passing through the cable to magnetically stimulate the piezoelectric resonator. (b) Maximum power obtained for magnetic fields ranging from 2.5 µT to 5 µT.*

To validate the proper operation of our device in any of the cases mentioned above, we implemented a setup for MF generation shown in Figure 5a. This setup essentially consists of a conductor used on high-voltage towers to carry high intensity currents and is suspended between two poles. We connected two oil-filled radiator heaters as electric load to the circuit. By turning on these radiators, the conductor manages to carry 15 A, generating a MF of 5 µT at a distance of 60 cm. Figure 5b shows the device resonating under this MF. As shown in Figure 5c, we measured a maximum output voltage of 1.51 V and a maximum power of 0.55 µW. It is important to note that, thanks to its small dimensions of less than 60 mm³, we achieved a power density of 9.19 µW/cm³. This value is considerably higher than similar applications using larger devices, reaching a power density between 0.53 µW/cm³ and 1.86 µW/cm³ for slightly higher MFs of around 7 µT. Furthermore, when compared with MEMS resonators from the literature [*81*], normalized power density values for KNN are found to be 0.08 µW/G·Hz·cm³, for AlN ranging from 0.84 to 5.8 µW/ G·Hz·cm³, and for PZT ranging from 0.25 to 56 0.08 µW/ G·Hz·cm³. Our resonator achieves a normalized power density of 9.19 µW/ G·Hz·cm³, which is higher than the values reported for AlN in the literature and within the ranges of

those using PZT. Therefore, this device would be functional in proximity to a wide variety of household appliances used daily and would be able to capture ambient MFs to supply a low-power IoT sensors for the monitoring of, for example, environmental conditions.

4. Conclusions

The article addresses the battery dependency of the IoT, which is a major barrier for its global deployment. We propose an innovative solution through the collection of low-intensity MFs, specifically in the microteslas range. The research is justified in the context of the IoT scalability, and the associated challenges related to the limited lifespan, maintenance, and cost of conventional batteries.

The study focuses on the manufacturing of a MEMS piezoelectric device with the integration of a magnetic tip mass designed to interact with ambient MFs.

The experimental section details the use of COMSOL Multiphysics® software to simulate the electromechanical behavior of the MEMS resonator and examines the impact of the magnetic tip mass on the resonance frequency and optimal impedance of the piezoelectric material.

The MEMS manufacturing process is presented clearly, highlighting the choice of a cantilever structure to provide maximum energy output.

The electrical characterizations were performed using a shaker to emulate ambient vibrations and a pair of Helmholtz coils to emulate MFs. The results are compared before and after adding the magnetic tip mass, revealing changes in the resonance frequency, optimal impedance, and generated power.

Finally, a specific application of the device in environments with residual MFs, such as high-voltage lines and homes, is presented. The device's functionality is validated through a setup generating MFs, emphasizing the efficiency of the device in capturing energy even under microtesla fields.

In summary, this work makes a valuable contribution addressing energy challenges in the IoT through ME energy harvesting. Experimental results and simulations support the viability and efficiency of the proposed approach, suggesting a significant potential for

the widespread implementation of ME energy harvesting technologies in various practical contexts.

Acknowledgments

G. Murillo thanks the financial support from the La Caixa Foundation under the Junior Leader Retaining Fellowship (LCF/BQ/PR19/11700010), the national projects PID2020-119350RA-I00, EUR2020-112082 and CNS2022-136065, under the Dynamization Actions "Europa Excelencia 2020" and the Consolidation Actions funded by the NextGenerationEU Instrument and Ramon y Cajal Fellowship 2020 (RYC2020-030501-I). This work has been carried out in collaboration with ENERGIOT DEVICES SL (www.energiot.com), who holds part of the intellectual property, and in the framework of the doctoral program in Electronic and Telecommunication Engineering of the Autonomous University of Barcelona.

3.4 Integration of ZnO nanostructures in MEMS devices using inkjet printing for energy harvesting

Integration of ZnO nanostructures in MEMS devices using inkjet printing for energy harvesting

Abstract

This work describes a process to integrate piezoelectric nanostructures with microelectromechanical systems (MEMS), combining inkjet printing and a mild hydrothermal growth technique to create energy harvesters driven by ambient vibrations. The process includes plasma treatment, material printing, and efficient and affordable growth of nanowires (NWs) through a hydrothermal method. Finite element method (FEM) is employed to validate the electromechanical behavior of the MEMS resonator. Additionally, electromechanical and physical characterization of the device is conducted to validate its functionality. This promising approach offers future perspectives for the use of MEMS devices and nanostructures in sensing or energy harvesting, standing out for its non-contact integration technology, cost-effectiveness, and environmental friendliness by eliminating the use of lead-based piezoelectric materials.

1. Introduction

In the last years, technology has evolved exponentially, and we are increasingly interconnected. The Internet of Things (IoT) has emerged in various applications, from sensors in agriculture to smart medical devices. However, one of the major drawback of the IoT is its dependence on the power supply of its devices, as many of them operate in remote locations or have limited size, making conventional supply challenging. Therefore, the effectiveness of the IoT largely depends on the ability of these devices to operate autonomously and sustainably [1, 6, 211–213]. To solve this issue, energy harvesting (EH) has gained prominence as a crucial solution, enabling harvesting energy from the surrounding environment, such as solar, thermal, vibrational, or electromagnetic energy [21–23, 214].

MEMS technology merges mechanical and electronic capabilities on a tiny scale, typically ranging from micrometers to millimeters. They use semiconductor-manufacturing technologies to integrate movable electromechanical structures into a single device. Their versatility is reflected in applications ranging from consumer devices, such as mobile phones, to industrial, medical, and automotive fields. Their impact on the technological industry is notable due to the introduction of new functionalities and system properties through changes in size scale, along with cost-effective mass production capabilities through microfabrication processes. MEMS devices find applications in various fields, including healthcare, mobile devices, environmental monitoring, smart homes, and food control [*56*, *236–239*].

There are several methods for transforming environmental energy into electrical energy. Piezoelectric transduction is one of the most commonly used techniques to convert mechanical or kinetic energy from environmental vibrations. Piezoelectric materials generate an electric charge in response to the application of mechanical force or deformation. Zinc oxide (ZnO), known for its wurtzite crystal structure, is particularly prominent due to its piezoelectric properties, wide bandgap, and suitability for optoelectronic applications. The ability to grow ZnO in various nanostructures, such as nanorods, NWs, nanosheets, nanobelts and nanospirals, provides versatility and potentially enhances properties like the Young's modulus. Furthermore, the

biocompatibility of ZnO nanostructures makes it a safer and more environmentally friendly piezoelectric material than other alternatives, such as lead-based lead zirconate titanate (PZT) [240–242].

Inkjet printing has emerged as a standout technique, facilitating the precise deposition of diverse liquid materials onto different substrates. Piezoelectric materials have further extended their capabilities for printing electronic devices in the last decades. Preferred for its non-contact nature, minimal ink wastage, and production of thin films, inkjet printing stands out in applications such as organic transistors, LEDs, solar cells, and sensors [46, 47, 51, 243, 244]. These piezoelectric inks are deposited through an inkjet print head in specific patterns, enabling the creation of electronic components, sensors, and actuators precisely and efficiently. This technique offers advantages in terms of flexibility, costs, and scalability in the production of piezoelectric devices, expanding its application in fields such as MEMS manufacturing, flexible sensors, and printed electronic devices [48–50, 245, 246].

The foundation of inkjet printing technology lies in the selective application of ink to specific areas of a substrate, presenting a rapid, reproducible, economical, and high-resolution alternative for material deposition. The non-contact nature of this technology positions it as a significant option to replace conventional material deposition techniques. Piezoelectric inks, widely employed in actuators or sensors due to their piezoelectric response, encompass various formulations, including both polymeric and ceramic options. Notably, ceramic materials such as ZnO, barium titanate ($BaTiO_3$), or PZT are favored for their heightened piezoelectric response, contributing to the overall effectiveness of the inkjet printing process in electronic device manufacturing.

This article focuses on the integration of piezoelectric nanostructures with MEMS through the combination of inkjet printing and a mild hydrothermal growth. The first part focuses on integrating ZnO nanostructures into MEMS devices using inkjet printing. The second part involves electromechanical and physical characterization, demonstrating the functionality of the devices. This integration of nanostructures, MEMS technology, and inkjet printing lays the foundation for innovative solutions, such as flexible energy harvesters and advanced sensors.

2. Experimental Section

2.1. Finite elements simulations

In this work, COMSOL Multiphysics software is employed to investigate the electromechanical behavior of a MEMS resonator and the impact of the SU-8 dielectric polymer on ZnO NWs. COMSOL Multiphysics, a versatile simulation software, utilizes the FEM to solve partial differential equations in scientific and engineering systems. The AC/DC (Electrostatics, Electrical Circuits, and Piezoelectricity) modules, as well as the Structural Mechanics (Solid Mechanics and Piezoelectricity) module, were employed for the simulations in this work.

2.2. MEMS Platforms Fabrication Process

The functional scheme of our piezoelectric MEMS platform is shown in Figure 1a. Our EH platform is based on a silicon-on-insulator (SOI) wafer (silicon: 15 µm—SiO2: 1 µm—silicon: 500 µm) [225, 227, 228, 230, 247]. The device layer is used to define the cantilever, and the bulk layer is used for the inertial mass (Figure 1b). Above the cantilever, a 200 nm titanium and platinum (Ti/Pt) layer is used as the bottom electrode. In most applications, the frequency of ambient vibrations is below 1 kHz [248]. For this reason, an inertial tip mass is used to decrease the natural frequency of the structure. The fabrication process of our devices is represented in Figure 1c. The thin Ti/Pt layer of the bottom electrode is deposited using radiofrequency reactive sputtering. The device structure is defined through multiple photolithography steps and deep reactive ion etching (DRIE). Finally, wet etching based on hydrofluoric acid (HF) is used to remove part of the buried oxide layer and consequently release the cantilever. In this work, we focus on the PEH-B1X1M1X1 device, shown in Figure 1a-c, with a mass area of 1 mm^2 and a cantilever area of 1 mm^2.

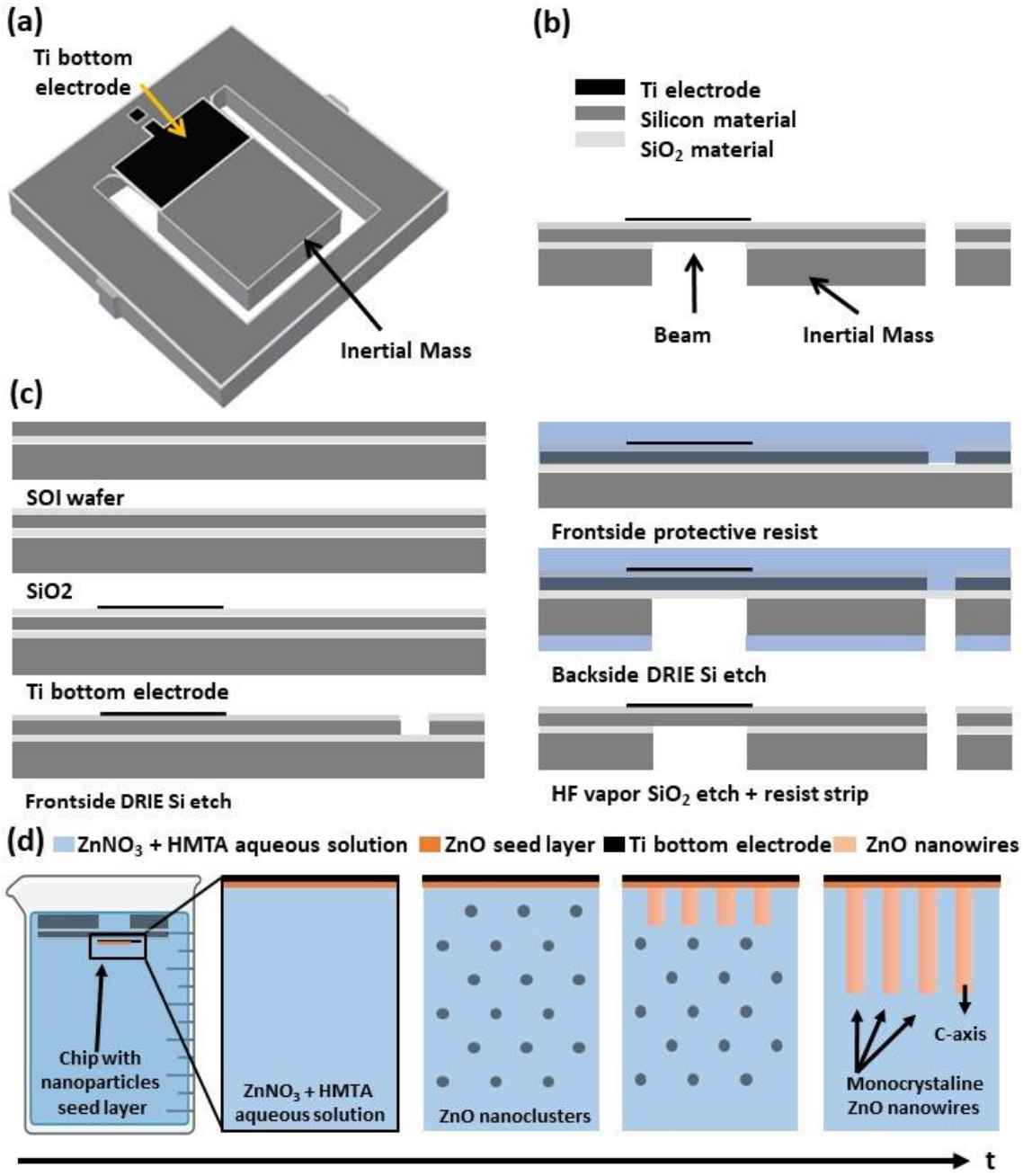


Figure 1: *(a) Schematic of the functional device configuration of the cantilever structure with a tip mass and a platinum bottom electrode on top of the beam; (b) cross-section sketch of the cantilever structure; (c) different steps of the fabrication process; (d) Representation of the performed hydrothermal method to grow ZnO NWs.*

2.3. ZnO Nanostructures

The MEMS EH device utilizes ZnO nanostructures, specifically NWs, which grow through an inexpensive and efficient hydrothermal method shown in Figure 1d [*249–251*]. The growth process of high-quality ZnO NWs involves the deposition of a seed layer using

inkjet printing with ZnO nanoparticles of approximately 8-16 nm, acting as nucleation centers on the substrate. Subsequently, a hydrothermal method at 80°C is employed with an aqueous solution of Zn(NO3)2 (Sigma Aldrich) and HMTA (Sigma Aldrich). Hexamethylenetetramine (HMTA) is a non-ionic organic heterocyclic compound ((CH2)6N4) entirely indispensable for the growth of ZnO NWs.

The method is carried out in a glass container, whose size varies according to the substrate, and is placed in a preheated oven at 80°C for 15 hours with the seed layer pointing towards the bottom of the container. Preheating the oven accelerates the increase in the temperature of the aqueous solution to 80°C, avoiding prolonged times at lower temperatures. This prevents premature precipitation of ZnO in the container before reaching 80°C, ensuring proper growth of ZnO NWs. After growth, the substrate is cleaned with water, followed by ethanol or isopropanol, to prevent NW aggregation due to surface tension.

2.4. Printable Materials

This work involves the use of three commercially available inks: a conductive, a dielectric, and a piezoelectric ink. The conductive ink used is the DryCure Au-J from C-INK Japan, composed of gold nanoparticles with an average size of 30 nm. The main solvent is water, containing a metallic content of around 10%, and a viscosity of 4 cP. For the dielectric material, PriElex® SU-8 ink from MICROCHEM is employed to encapsulate ZnO NWs. This ink is an epoxy-based photoresist that requires curing at 365 nm. It has a viscosity of 9.33 cP and a dielectric constant of 3.2 at 1 MHz. The ZnO ink used to create the seed layer is a the Sigma Aldrich's ZnO nanoparticle ink, composed of crystalline ZnO particles of 8 to 16 nm, dispersed in isopropanol and propylene glycol. It contains a solid content of around 2.5 % and exhibits a viscosity between 8 and 14 cP.

2.5. Inkjet Printing process

The printer used for printing the layers is the FUJIFILM Dimatrix Materials Printer DMP-2831, classified as Drop on Demand (DOD) and piezoelectric, as it uses a piezoelectric ceramic plate to control the ejection of ink droplets. The piezoelectric ejection system has 16 nozzles, and the droplet volume can vary between one and ten picoliters. Each

combination of ink and substrate has specific printing conditions, and key parameters to adjust include the stage and nozzles temperature, waveform, drop spacing (DS), and printing pattern. It is essential to perform pre-printing and post-printing processes to achieve satisfactory results. The pre-printing process involves oxygen plasma treatment to change the substrate's surface energy and modify the affinity of the ink solvents toward the substrate. The substrate is introduced into the Smart Plasma from Plasma Technology GmbH before printing, where O_2 plasma treatment takes place. The duration of exposure to O_2 plasma varies depending on the ink to be printed and the substrate to be used. After plasma treatment, the contact angle of the drop with respect to the substrate undergoes changes. The effect is also significant on ZnO NWs, which contain oxygen vacancies (charged electron donors) that can neutralize the potential generated by the piezoelectric effect. By applying O_2 plasma, oxygen radicals and ions reach the surface of the NWs and diffuse into their volume to fill and eliminate the oxygen vacancies. As a result, the potential generated in the NWs increases [*252*, *253*].

On the other hand, the post-printing treatment involves evaporating the solvents from the ink or sintering the metal nanoparticles. Since SU-8 is an epoxy polymer, it requires UV radiation curing to strengthen and acquire dielectric properties.

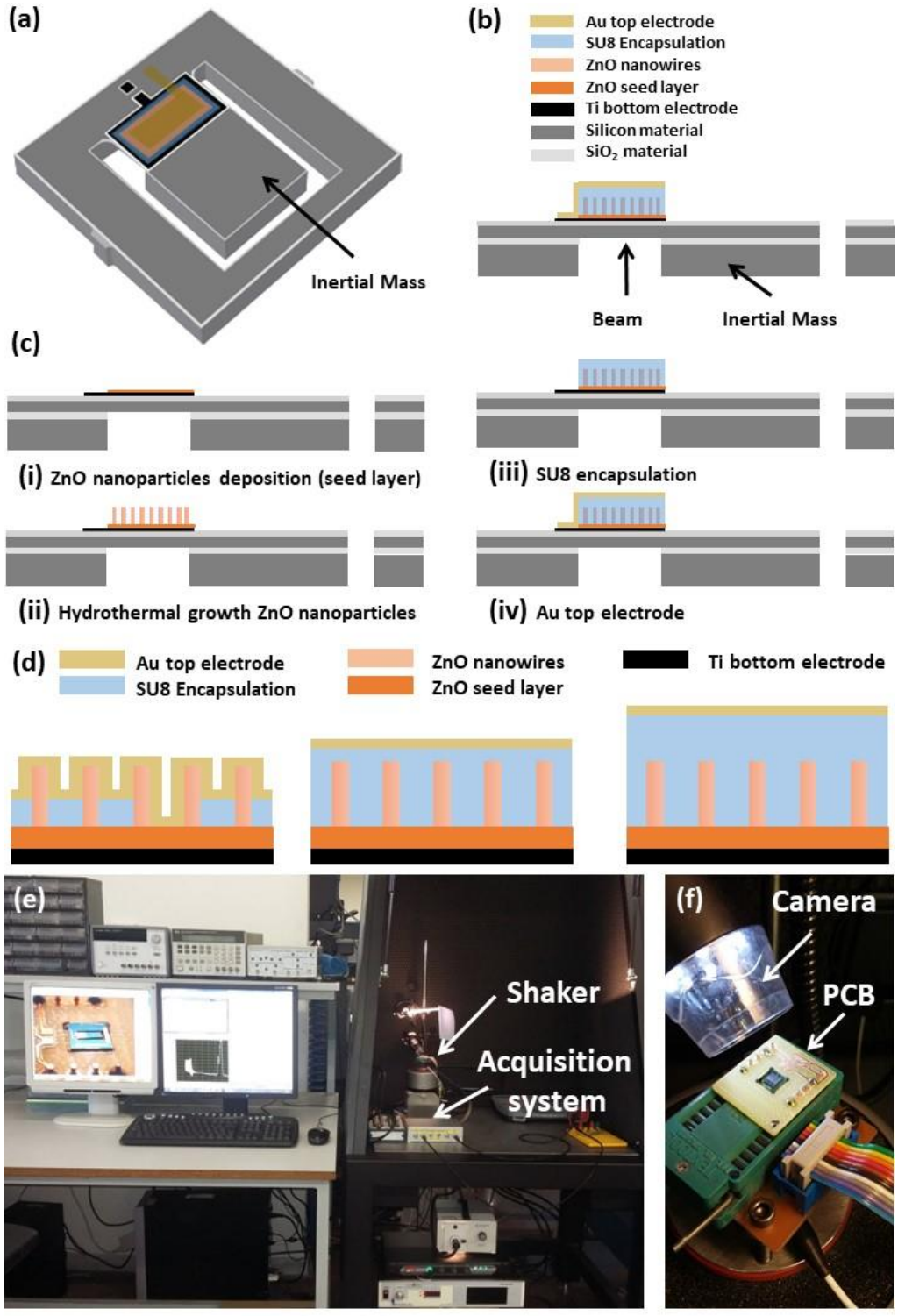


Figure 2: (a) Schematic of the functional device configuration of the cantilever structure with a mass at the tip and a piezoelectric material deposited on top of the beam; (b) cross-sectional sketch of the cantilever structure; (c) different stages of the fabrication process; (d) Schematic representation of three possible cases with respect to the SU-8 DS: (1) High DS (2) Optimized DS (3) Low DS. Measurement setup configuration used to perform the electromechanical characterization: (e) General view and (f) Close-up view of the shaker.

To achieve complete functionalization of the nanogenerator shown in Figure 2a-b and fully integrate ZnO nanostructures with the MEMS structure, three printing steps are carried out.

ZnO printing

In the initial step, a layer of ZnO nanoparticle seed is printed on the bottom Ti/Pt electrode.

The precise printing of the ZnO nanoparticle as seed layer, shown in Figure 2c i, is crucial due to the critical dependence of NW characteristics on the seed layer. A key parameter is DS, with three possibilities observed in Figure 2d. Too high DS results in separate drops, too low DS causes drop overlap and variations for nanoparticles depending on the thickness of each zone, while an optimal DS results in a continuous line.

The optimized printing conditions for this layer were specifically established. The DS was set at 60 µm, ensuring adequate distribution of nanoparticles. The substrate temperature was maintained at 50°C to facilitate optimal ink distribution. A 40 W plasma treatment was applied for 30 seconds to improve adhesion of nanoparticles to the substrate. Subsequently, a post-processing step at 80 °C for 5 minutes was crucial for the effective evaporation of solvents used in the printing ink. These optimized conditions are fundamental to ensure the successful and uniform growth of ZnO NWs in the next stage of the process.

SU8 printing

Following the growth of ZnO NWs through the hydrothermal method, described in Section 2.3, the insulating polymer SU-8 is printed, as illustrated in Figure 2c iii, which functions to encapsulate the NWs and provide robustness to the structure.

The optimization of printing parameters proved crucial for the nanogenerator's performance. The height of the SU-8 layer, inversely proportional to DS, was decisive in three possible scenarios shown in Figure 2d: high DS, proning to short circuits; low DS, affecting the efficiency of the nanogenerator; and optimized DS, achieving maximum voltages without short circuits [*254–256*]. Different DS values were explored, identifying

two as the most suitable. Specific printing conditions included a DS of 40-45 µm, a substrate temperature of 40°C, 24W plasma treatment for 30 seconds, and UV (365 nm) post-processing for 30 seconds. These conditions were meticulously adjusted to try to ensure optimal performance and structural integrity of the nanogenerator in the final stage of the process.

Gold printing

Finally, as shown in Figure 2c iv, an ink containing gold nanoparticles is printed to create the top gold contact. The main goal is to print these layers on the beam of the structures, given that this is the region subjected to the most significant mechanical strain during cantilever vibrations. The stress from the cantilever is transferred to the integrated printed structure and, consequently, to the NWs. When the NWs are compressed or stretched, an electric potential is generated along them, and the printed top gold contact becomes electrically charged. As a result, an electric potential difference is established between the bottom and top electrodes.

The gold electrode layer, in the final stage of the process shown in Figure 2c iv, was printed to establish the top contact of the nanogenerator. Printing was carried out on the SU-8 layer. Since it is a conductive ink, heat was applied not only to evaporate the solvent but also to sinter the nanoparticles. In this case, they were heated to 140°C for 20 minutes in an oven.

2.6. Electrical measurements

The electrical characterization was conducted using an electrodynamic shaker VR9500 from Vibration Testing Controller to simulate environmental vibrations at various input acceleration magnitudes (Figure 2e). This process is controlled by an “ad hoc” MATLAB program, enabling automation, acquisition, and processing of voltage measurements. All data were acquired using a high-impedance National Instruments PCI-6132 acquisition system and a BNC-2110 terminal block. The device was connected through a specifically designed PCB (Figure 2f), providing physical support and electrical connection.

2.7. Physical characterization

The physical inspections of the manufactured NWs were carried out using a scanning electron microscope (SEM) Auriga-40 (Carl Zeiss). Cross-sectional cuts of the device surfaces to examine the thicknesses of different material layers were performed using a Cross Beam focused ion beam (FIB), specifically the Carl Zeiss Crossbeam 550LB.

3. Results and Discussions

3.1. Finite elements simulation

There are many available structural configurations for piezoelectric EH devices, with the cantilever, circular diaphragm, and cymbal being the most common. The cantilever produces the highest energy output when used as a piezoelectric energy harvester. Additionally, the cantilever structure achieves a lower resonance frequency for a given size. For this reason, the cantilever structure has been chosen. As illustrated in Figure 3a-b, the first study focuses on a MEMS platform resonator to determine its resonance frequency, stress in the piezoelectric beam, and displacement of the inertial mass. The natural frequency is approximately 1045.5 Hz, with a maximum stress of $5x10^7$ N/m² and a maximum displacement of 230 µm for an acceleration of 0.1 G.

The second examined model, as shown in Figure 3c-d consists of a set of ZnO NWs embedded in an SU-8 layer, aiming to determine the theoretically optimal thickness of the SU-8 layer between the top of the NWs and the top electrode. This structure comprises a 3x3 array of ZnO NWs embedded in SU-8, with a top gold electrode and a Pt electrode grounded, used for measuring electrical potential. ZnO NWs are modeled as cylinders with a height of 1000 nm and a diameter of 90 nm, experiencing deformation under the application of a vertical displacement on the surface structure. The optimal height of SU-8 is sought to avoid short circuits, prevent electrical leaks, and maximize the transfer of mechanical energy. Maximizing the transfer of mechanical energy is crucial due to the relationship between the height of SU-8 and the deformation of the ZnO NW, which influence the electrical potential along the NW. As the structure contains two electrodes and a dielectric material between them, it can be considered a capacitor.

The equation for a capacitor is expressed as follows:

$$C = \frac{Q}{V}$$

Where Q represents the charge stored in the capacitor (in coulombs), C is the capacitance of the capacitor (in farads), and V is the potential difference (voltage) across the capacitor terminals (in volts). Capacitance is also related to the capacitor's geometry and the properties of the dielectric material between its plates:

$$C = \varepsilon \frac{A}{d}$$

Where ε represents the permittivity of the dielectric material, A is the area of the capacitor plates, and d is the distance between the plates.

Consequently, any variation in the thickness of the dielectric material will affect the voltage between both electrodes. Since developing a precise mathematical model would be extremely laborious due to the numerous variables comprising the system, a FEM simulation is conducted to determine the optimal height of SU-8 corresponding to the maximum voltage obtained on the gold electrode.

Figure 3c presents the cross-sectional views of the different 3D models, each corresponding to the set of nas encapsulated with different thicknesses of SU-8, alongside the electric potential distribution throughout the structure under an applied compressing displacement on the top layer. This displacement has a mean value of 2.4 x 10^{-4} µm, with the bottom electrode held fixed, resulting in a vertical deformation across the entire structure. For the sake of simplicity, the free-carriers in the ZnO that could lead to a potential screening effect are not taken into account. of the Furthermore, Figure 3d illustrates the relationship between the voltage between the electrodes and the SU-8 layer's thickness with respect to the NW top. It is evident that the displacement-induced voltage across the piezoelectric structure decreases as the SU-8 thickness increases. However, it is crucial to note that physical contact between the ZnO NWs and the gold electrode would result in a metal-semiconductor-metal junction[*257*], likely forming an ohmic contact that significantly diminishes the generated voltage. Therefore, to prevent

this, the SU-8 layer must extend slightly beyond the NWs, ensuring there is no direct contact with the top electrode.

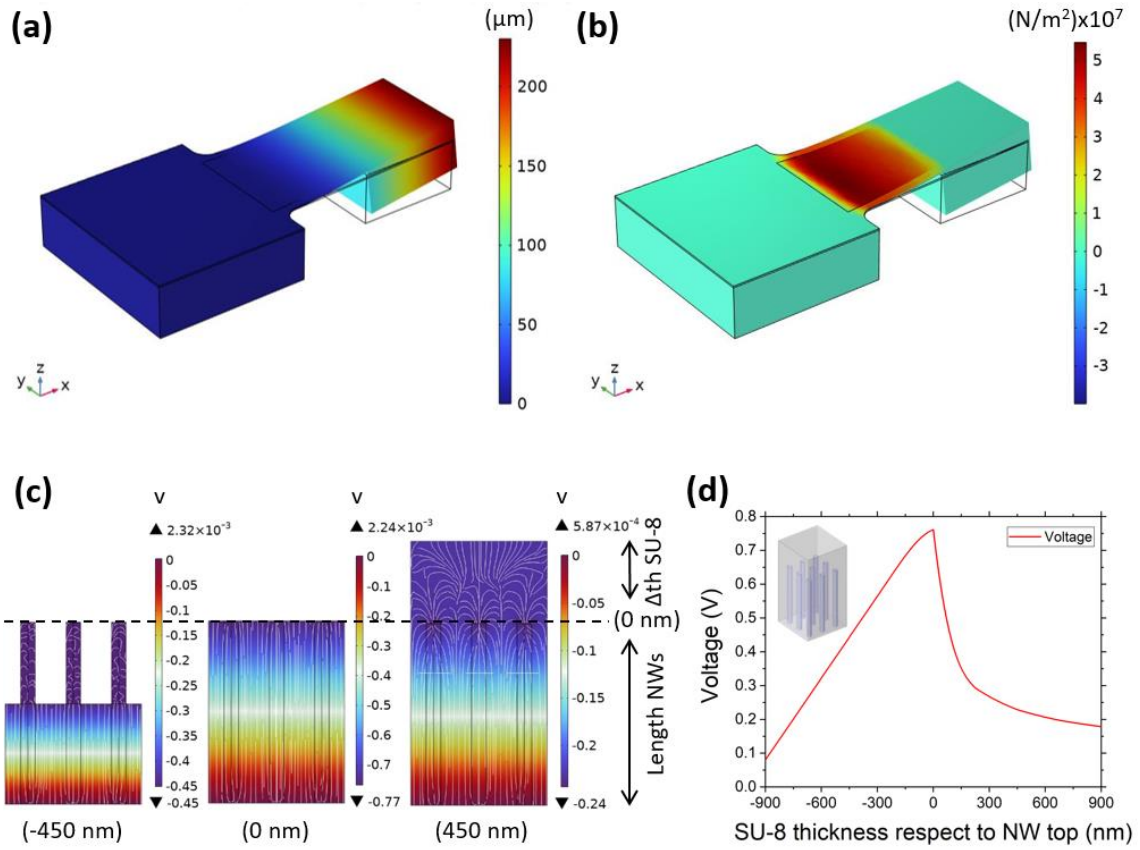


Figure 3: 3D model of the simulated piezoelectric resonator structure with COMSOL Multiphysics. (a) Von Mises stress; (b) total displacement amplitude. 3D model of a set of NWs encapsulated with SU-8 simulated with COMSOL Multiphysics. (c) Structures with different thicknesses of the SU-8 layer, and the electric potential generated when strained; (d) Relationship between SU-8 thickness and the voltage generated between the electrodes.

3.2. Electrical Characterization

Electromechanical characterization of the resonators based on MEMS technology was conducted. As mentioned above, the device was connected through an ad-hoc designed PCB, providing physical support and electrical connection.

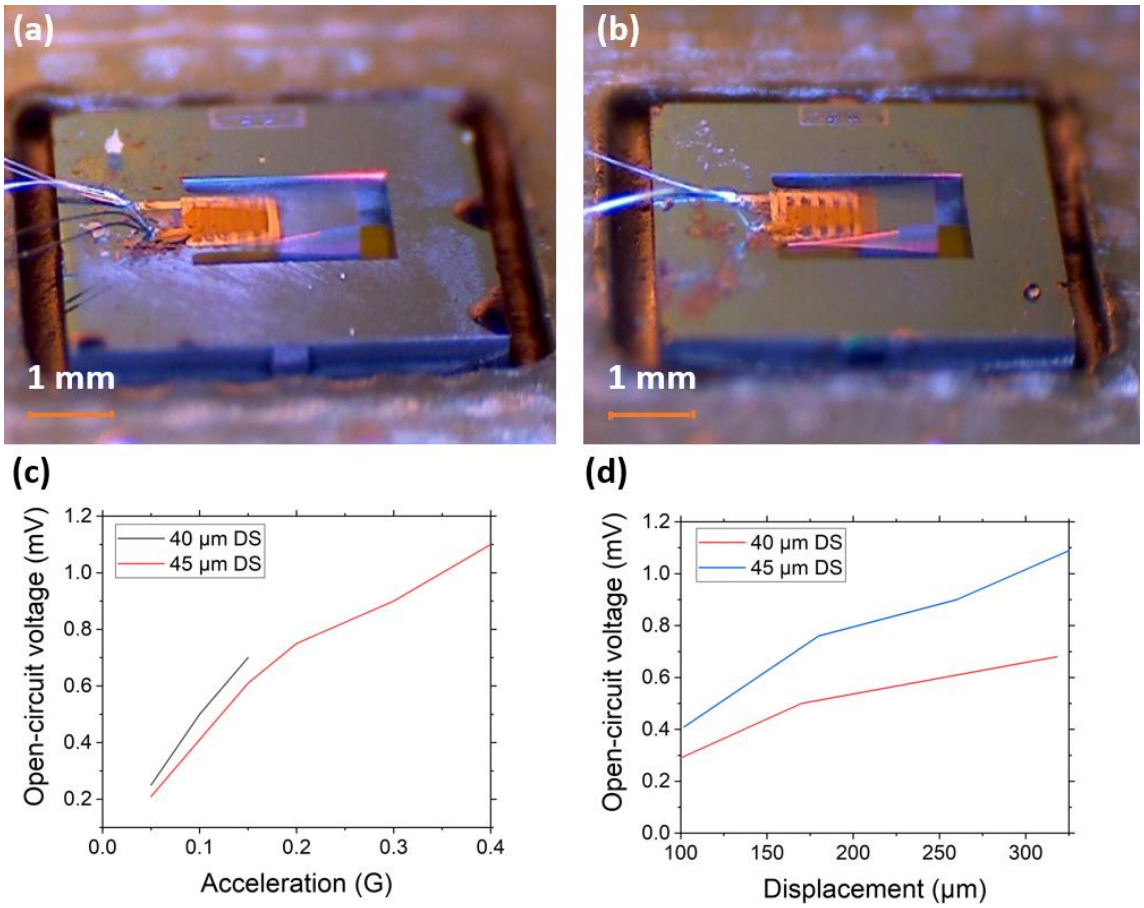


***Figure 4**: Close-up view of the MEMS device with (a) SU-8 DS of 40 µm and (b) SU-8 DS of 45 µm; (c) Comparative graph of the open-circuit voltage of devices with DS of 40 µm and 45 µm for various given accelerations; (d) Comparative graph of the open-circuit voltage of devices with DS of 40 µm and 45 µm for the same displacement.*

Both devices exhibit different voltages under the same applied acceleration. As depicted in Figure 4a, the device with an SU-8 layer printed with a DS of 45 µm has a resonance frequency of 1105.5 Hz. In contrast, the device with a DS of 40 µm, shown in Figure 4b, resonates at 1056.5 Hz, which is 49 Hz lower.

For a better comparison between the two devices, it is suggested to compare the voltage outputs at the same vibration amplitude. It is important to highlight that, in both cases, a maximum amplitude of 325 µm has been maintained to prevent the damage of the resonator. In the case of the device with a DS of 40 µm, this maximum amplitude was achieved with an acceleration of 0.15 G, while for the device with a DS of 45 µm, it is required an acceleration of 0.4 G.

Observing Figure 4c, it is evident that when the devices are at resonance for a given acceleration, the device with DS 40 µm obtains a slightly higher voltage than the device with DS 45 µm. However, when comparing the voltage obtained when reaching an equal vibration amplitude, shown in Figure 4d, it is observed that the voltages obtained by the device with DS 45 µm are higher, suggesting greater efficiency in this case.

This higher efficiency validates the optimization process, discussed in previous sections, of the SU-8 layer printed on ZnO NWs. By increasing the DS and, i.e. reducing the dielectric layer between the NW top and the electrode, a higher voltage is generated, and thus, a greater amount of power is obtained.

3.3. Physical Characterization

Firstly, an inspection is carried out through SEM. As evidenced in Figure 5a-b and d, the NWs display excellent vertical alignment and high density, with hexagonal morphologies typical of wurtzite crystal configurations, covering almost the entire bottom surface of the Pt substrate.

During the hydrothermal growth of ZnO NWs, there are two growth modes: heterogeneous nucleation and homogeneous nucleation. NWs undergoing heterogeneous nucleation use the seed layer as the starting point for their growth. In contrast, NWs following homogeneous nucleation can use impurities in the solution or in the container, as well as small aggregations of ZnO particles, as starting centers to develop into ZnO NWs. Figure 5b shows an example of both growth modes. These NWs, although not of the same size and not aligned perpendicularly to the substrate, are also grown on the chip's surface, resulting in a decrease in the efficiency of the nanogenerator. The need to avoid homogeneous nucleation is emphasized, as heterogeneous nucleation requires less activation energy. The use of high temperatures is discouraged to prevent homogeneous nucleation and the importance of keeping the container clean and the solution free of impurities that may act as nucleation centers is emphasized.

In Figure 5c, an SEM image is shown representing a line pattern, a sequence of lines with variable DS used to find the optimum value. The three possible cases mentioned earlier

are shown depending on the DS used (separate drops, drop overlap, and continuous line). In this case, the first continuously printed line is clearly observable, which has a DS of 60 µm, used for our prints.

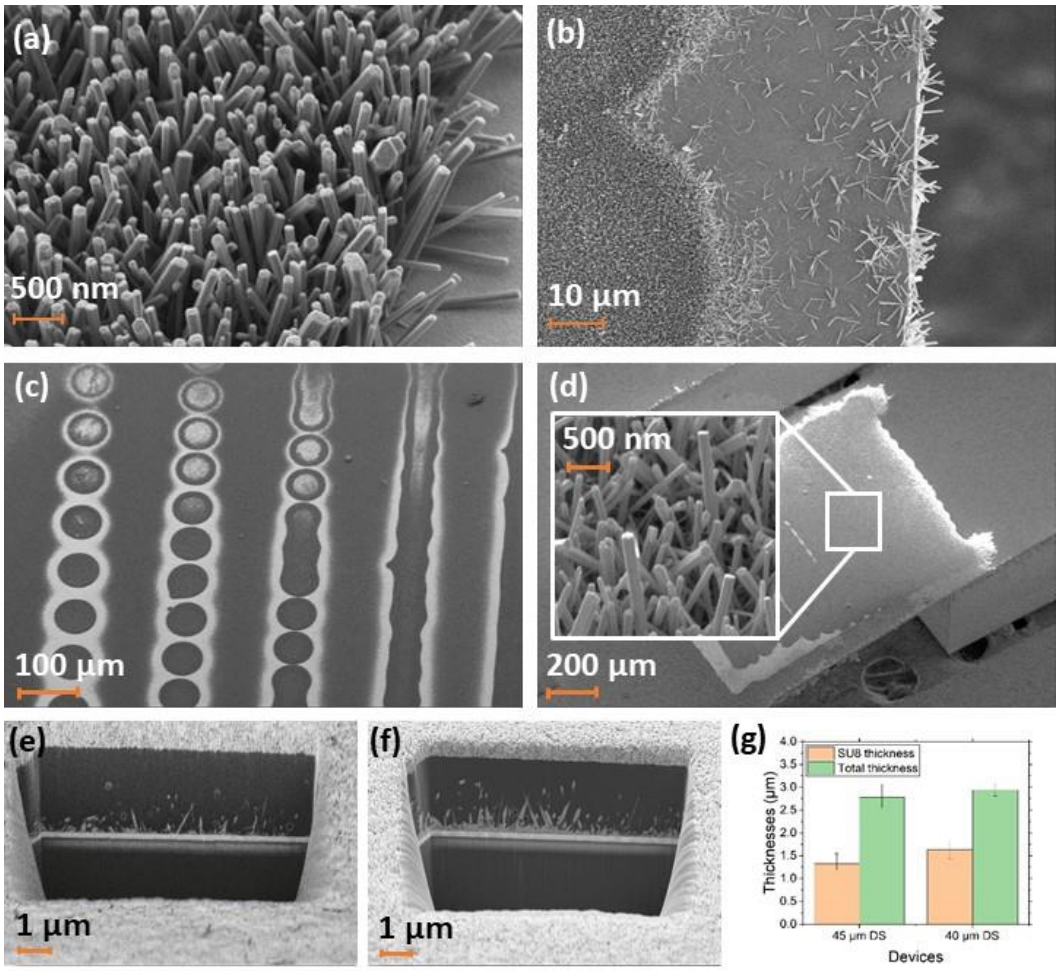


Figure 5: *(a) ZnO NWs grown on the Pt bottom electrode of the MEMS device; (b) NWs grown from the ZnO nanoparticles seed layer (left) and residual NWs grown around ZnO seed layer (right); (c) ZnO NWs forming a line pattern with several DSs; (d) ZnO NWs grown on the Pt bottom contact of the MEMS device; Cross-section obtained with FIB of the MEMS device with (e) SU-8 DS of 40 µm and (f) SU-8 DS of 45 µm; (g) Graph of the average thickness of the SU-8 layer between the NWs and the upper gold electrode and the average thickness of the total layer between the two electrodes.*

To check the integration of the NWs in the SU-8 layer and measure the thicknesses of different layers, a cross-sectional analysis of the top device layers has be carried out. As seen in Figure 5 e-g, the combined thickness of both layers (i.e. NWs and SU-8) is 2.94 $\pm$ 0.13 µm for the device with a DS of 40 µm. The average thickness of the SU-8 layer is

1.63 ± 0.23 µm. Meanwhile, for the device with DS of 45 µm, the total thickness is 2.76 ± 0.26 µm, and the average thickness of the SU-8 layer is 1.32 ± 0.20 µm.

Therefore, these measurements allow validating again that by reducing the dielectric layer thickness on top of the NWS, the generated power is higher. It is important to note that although there is margin for efficiency improvement by reducing the SU-8 thickness bellow 1 µm, this is not a straightforward task due to the inhomogeneity of the ZnO and SU-8 layer thicknesses and the variable length of the NW length. For this reason, the maximum reduction in the dielectric layer thickness achieved in this study, without causing shortcut between the electrode was the case with a DS of 45 µm.

In the future perspective, the possibility of depositing a thin oxide layer, with atomic layer deposition (ALD) or other technique, over the ZnO NWs grown on the bottom electrode could be considered to prevent shortcuts between the two electrodes. Consequently, the thickness of SU-8 layer could be reduced to improve the generated voltage. After this optimization, the proposed devices could be employed in applications such as self-powered accelerometers, mass or force sensors, etc.

4. Conclusions

This work has successfully achieved the two proposed objectives. Firstly, the integration of ZnO piezoelectric nanostructures with MEMS devices has been successfully carried out using inkjet printing technology, and the integrated MEMS resonators have been electromechanically characterized to validate their functionality.

During the integration process, the ZnO seed layer was printed onto a Pt electrode, vertical ZnO NWs were grown on the structure, and they were encapsulated with SU-8. Subsequently, a gold contact was added to form the top electrode of the device. The nanostructures were visualized with a SEM, confirming good verticality and quality. Additionally, the gold and SU-8 layers were also observed with the SEM, highlighting the importance of the latter in the outcome of the nanogenerators, as evidenced in computer simulations.

The electromechanical characterization of manufactured MEMS resonators has also been successfully conducted. Two MEMS devices with a similar structure but with different DS

of the printed SU-8 layer (40 µm and 45 µm) generated approximately 0.7 mV and 1.1 mV, respectively, for the same vibration amplitude.

Although the generated voltage is still relatively low, it is expected to increase in the future with the continued optimization of integration. The combination of its low cost, the ease of integration of ZnO piezoelectric nanostructures with inkjet printing on resonators, and its ability to generate electricity through EH make these MEMS resonators a viable future alternative for low-power devices. Furthermore, the electricity collection from ambient energy and the elimination of lead-based piezoelectric nanostructures usage also contribute to making the nanogenerators environmentally friendly.

Inkjet printing has proven to be a useful bottom-up technology, enabling rapid prototyping. The successful deposition of three materials with this technique has simplified the integration process. Moreover, being a non-contact technology, inkjet printing has been particularly useful in applications involving MEMS resonators, avoiding the risk of damaging the structure. Undoubtedly, inkjet printing should be considered as a possible alternative for depositing materials in MEMS applications.

The theoretical analysis of resonance frequency, represented by the equation of a harmonic oscillator, supported the idea that the structure with a SU-8 DS of 45 µm was stiffer. The importance of comparing the voltage obtained when the vibration amplitude is the same rather than simply comparing accelerations was emphasized.

The images captured during resonance revealed that, at an acceleration of 0.2 G, the device with a DS of 40 µm and, at an acceleration of 0.4 G, the resonant with a DS of 45 µm attained comparable vibration amplitudes (318 µm and 329 µm, respectively). However, the maximum voltage recorded for the 45 µm device was greater (1.1 mV) in contrast to the 40 µm device (0.6 mV). In summary, it was concluded that the MEMS resonator with a SU-8 DS of 45 µm generated a higher voltage with a comparable vibration amplitude and, therefore, was more efficient.

4 DISCUSSION

The research has addressed on two fundamental areas: one dedicated to explore and compare triboelectric materials, and the other focused on piezoelectric materials. These materials and manufacturing methods have been selected according to the requirements that best suit each application and its associated manufacturing cost, with the main consideration of obtaining low-cost devices and using lead-free materials.

4.1 Triboelectric materials

The research conducted on triboelectric materials has been a fundamental component within the scope of this doctoral thesis. The study began with the need to deeply understand the fundamental principles of contact electrification, which required a comprehensive review of scientific literature and the implementation of a specific characterization setup. This setup, designed to measure the current or voltage generated by materials as a function of a given force (more information in the annex), has been crucial for evaluating the potential of different triboelectric materials in energy generation. The manufacturing of EH devices based on these materials has been significantly facilitated and enhanced through the use of RPTs, such as plotter cutting, laser cutting, and 3D printing. These techniques have allowed for agile iteration and rapid adaptation of the devices to meet specific application requirements. However, challenges have been identified in certain manufacturing methods, such as in the case of laser etching the surface of triboelectric materials to maximize the contact area. Although this method has been successfully used in the literature through standard microelectronics etching processes like RIE, limitations were encountered in this case due to resolution and material degradation during the etching process, preventing its use for maximizing the contact surface. The most significant achievement of this research has been the validation of TENG devices as a viable solution for EH. These devices were designed, manufactured, and spacer optimization was carried out to improve efficiency and reduce manufacturing costs. Additional techniques, such as charge injection, were explored to increase surface charge density, and comprehensive tests were conducted to validate device performance under various conditions, resulting in a 1116% increase in generated voltage. Furthermore, by using only two devices connected in parallel, 30 LEDs were illuminated every 12 seconds. This achievement was made possible by the generation of

10 μW of energy produced by manual pulsation of the palm of the hand with an average of 8 N of force. The research carried out in triboelectric materials has been a fundamental component within the scope of this doctoral thesis.

4.2 Piezoelectric materials

The research conducted on piezoelectric materials in this doctoral thesis constitutes the majority of it, focusing on the study and application of materials such as PVDF, AlN, and ZnO, thus avoiding the use of lead-based piezoelectric materials, such as PZT. In this context, two fundamental approaches have been addressed: one macroscopic, using 3D printing technology for EH structure generation, and another microscopic, through the implementation of MEMS devices. Regarding the macroscopic approach, 3D printing has been employed for manufacturing EH structures, primarily using commercial PVDF as the piezoelectric material. On the other hand, in the microscopic approach, the potential of MEMS devices has been explored. Within this framework, two prominent research lines have been developed. Firstly, the utilization of ultra-low-intensity MFs as a mechanism for energy generation was investigated, employing microelectronics manufacturing technology. This strategy involved the design and fabrication of MEMS structures, as well as the use of "pick and place" machines, to achieve functional devices. Secondly, the possibility of using IJP to deposit thin layers of ZnO as piezoelectric material, structural dielectrics, and metal electrodes, onto silicon substrates, was explored to develop MEMS devices for vibrational harvesting.

Use of 3D printing for EH

The research using 3D printing for EH in this doctoral thesis begins with the optimization of the design of a piezoelectric harvester, considering multiple parameters such as beam dimensions, inertial mass and piezoelectric material arrangement. To achieve this purpose, parametric simulations and theoretical calculations are carried out to determine optimal combinations of dimensions that maximize energy generation at the desired resonance frequency, set at 50 Hz. Regarding the harvester manufacturing, 3D printing is used for structure creation and plotter cutting for shaping the piezoelectric material. FDM printing technology is selected due to its versatility and the possibility of pausing the

process to insert the piezoelectric material during fabrication. High-quality layering in printing is crucial to ensure optimal harvester performance, so procedures for integrating the piezoelectric material into the printed structure are described in detail, ensuring proper encapsulation and solid electrical connection. Subsequently, thorough electrical and physical characterization of the harvester is conducted, including voltage and power generated tests. Results show a maximum power of 1.46 mW with an optimal impedance of 5 MΩ and a power density of 290.84 μW/cm^3, considering the volume of the inertial mass, with an acceleration of 1 G, confirming the effectiveness of the proposed design. In comparison with powers and power densities reported in the literature for piezoelectric EH devices using PVDF as the material, with values ranging between 100-2000 μW/cm^3 [*258–260*], it can be concluded that, in terms of power density, our device does not reach the maximum efficiency observed in previous studies. However, it is important to consider that this device constitutes a first proof of concept version intended to validate its operation and integration. This initial version presents room for improvement, which could be achieved through a material replacement, the adjustment of printing layers, and the cantilever shape optimization, among other aspects. It is expected that these modifications will lead to a significant improvement in energy generation in future design iterations. It is relevant to highlight that generally, all these devices in the literature use more expensive manufacturing techniques, implying that although our device may be less efficient in terms of generated energy, it would be much less expensive to manufacture compared to those existing devices. Furthermore, as an extension of its functionality, the harvester is validated as a sensor, developing a device capable of measuring the current flowing through a wire, based on the output voltage generated by the resonator. This comprehensive research not only contributes to the advancement in optimization and manufacturing of piezoelectric harvesters but also extends their application, as both energy generators and sensors, in various engineering and technology fields.

Use of MEMS as technological platform

The first research line with MEMS proposes a solution to harness ultra-low-intensity MFs for EH. The work focuses on manufacturing a MEMS device using microelectronics

manufacturing technology and the subsequent assembly of a magnetic mass using a pick-and-place machine. Thanks to the magnetic mass, the device interacts with MFs and get into resonance. Finite element simulations are conducted to analyze MEMS behavior, such as resonance frequency change, optimal load impedance, and generated power when adding a magnetic tip mass. Functionality is validated and electromechanically characterized, achieving a maximum voltage of 1.51 V, a generated power of 0.55 µW at an optimal impedance of 2 MΩ, and a power density of 9.19 µW/cm^3, with an alternate MF of 5 µT at 50 Hz. The power density obtained is higher than the claimed by other devices described in the literature for harvesting energy with MF intensities below 7 µT. Additionally, the functional validation is done with an application example where the device manages to operate at a distance of 60 cm from a cable carrying a current of 15 A, which is comparable to the typical power consumption of the majority of the household appliances, such as an oven, washing machine, dryer, air conditioner, or ceramic hob. Due to the compact size of our device, the possibility of placing several of these devices in parallel, as an array, to multiply the generated power is also proposed. Furthermore, by using a charge pump, it would be feasible to increase the output voltage, if required by the final application.

The second article focuses on the integration of ZnO piezoelectric nanostructures with MEMS devices using IJP technology. The integration was successfully carried out, demonstrating that IJP is a very useful technology that allowed successful deposition of three materials with the same technique, simplifying the integration process. Furthermore, being a contactless technology, IJP has been particularly useful when working with MEMS, avoiding the risk of damaging the mechanical structures. Finite element simulations were performed for the study of the resonance frequency and the validation of the optimization process of the inkjet printing. After manufacturing MEMS resonators, the electromechanical characterization was performed to validate their functionality. MEMS devices with a similar structure but with different thicknesses of the printed SU-8 layer (40 µm and 45 µm) generated approximately 0.7 mV and 1.1 mV, respectively, for the same vibration amplitude, using accelerations of 0.2 G and 0.4 G, respectively. Although the generated voltage remains relatively low, it is expected to be increased in the future with a continuous integration optimization. Thanks to the

combination of the low-cost and straightforward integration of piezoelectric nanostructures with MEMS by means of IJP, the presented hybrid technology represent an interesting future alternative to be further investigated.

4.3 Estimated cost of harvesting devices

An estimation of the manufacturing cost associated with the four devices developed within the scope of this doctoral research has been conducted, as shown in Table 2. It is important to note that labor costs have not been considered in the overall calculation, except for the MEMS manufacturing process, where they are conducted in a cleanroom environment and billed collectively.

Table 2: *Table of the cost of the four EH devices manufactured within this thesis*

Device type	Components	Cost
Triboelectric	2 x Mylar 50 mm x 50mm	0.86 €
	4 x Copper 50 mm x 50mm	1.64 €
	3 x PET 70 mm x 70 mm	0.79 €
	3D support	0.72 €
	Total Cost	**4.01 €**
3D Printing	6 g PLA structure	0.29 €
	PVDF 38 mm x 14 mm	1.83 €
	2 x Spring load	1.23 €
	2 x Galvanized iron mass 30 mm x 40 mm	0.12 €
	Total Cost	**3.47 €**
MEMS with Magnetic Mass	1 x Device	4.59 €
	1 x Magnet mass (3 mm diameter x 2 mm height)	0.22 €
	Total Cost	**4.81 €**
MEMS with IJP and ZnO nanostructures	1 x Device	1.20 €
	4 µL Au ink	0.20 €
	4 µL ZnO ink	0.05 €
	10 µL Au ink	0.10 €
	Total Cost	**1.55 €**

The triboelectric device is comprised of two Mylar sheets, measuring 50 mm by 50 mm, four copper sheets of the same size, three PET sheets, measuring 70 mm by 70 mm, and a 3D support structure where the PET sheets are assembled. A detailed breakdown of the

components reveals a total cost of 4.01 €. Conversely, the 3D printing device features a simplified structure, with a total cost of 3.47 €, including 6 g of PLA for the structure, a PVDF sheet measuring 38 mm by 14 mm, two spring loads, and two galvanized iron masses measuring 30 mm by 40 mm.

The MEMS device with magnetic mass stands out for its higher total cost of 4.81 €, primarily composed of the device itself and a magnetic mass measuring 3 mm in diameter and 2 mm in height. In contrast, the device based on MEMS with additional IJP layers and hydrothermally grown ZnO nanostructures, with a total cost of 1.55 €, presents a relatively simple MEMS structure, with small quantities of gold, SU-8, and ZnO inks.

It is important to consider that all costs were calculated based on orders placed during the thesis in small quantities. However, it is expected that these devices will significantly reduce their final cost when purchased in large-scale quantities for mass production. Specifically for MEMS devices, they were fabricated on 4" wafers and in batches of 2 to 9 wafers. By manufacturing in foundries such as, for example, SilTerra, a company based in Malaysia specialized in semiconductor technology and utilizing AlN manufacturing processes [*261*], it would be possible to produce chips on wafers of up to 8". This would quadruple the number of chips per wafer, significantly reducing the manufacturing costs.

5 CONCLUSIONS

The doctoral thesis extensively investigated into the field of EH, with a focus on leveraging piezoelectric and triboelectric materials for environmental EH. A special emphasis was placed on researching lead-free and cost-effective materials, resulting in the following accomplishments:

1. Through the exploration and utilization of triboelectric materials coupled with enhanced surface charge, a TENG device capable of harvesting mechanical energy from human hand tapping was developed at an approximate cost of 4.01 €, generating a power output of 10 µW.

2. The integration of PVDF piezoelectric material within a PLA structure facilitated the development, validation, and patenting of a vibrational energy harvester using 3D printing technology. With an approximate cost of 3.47 €, this harvester achieves a power density of 290.84 µW/cm³ at 1G acceleration and 50 Hz frequency.

3. Manufacture of a MEMS device employing AlN as the lead-free piezoelectric material, designed for harnessing ultra-low-intensity MFs for EH. This device, costing approximately 4.81 €, produces an output voltage of 1.51 V and a power density of 9.19 µW/cm³ under a 5 µT MF.

4. Successful integration of ZnO piezoelectric nanostructures with MEMS devices via IJP technology, showcasing its viability for material deposition in MEMS applications. This approach allows for RPT and prevents structural damage due to its non-contact nature. Moreover, a device manufactured at an approximate cost of 1.55 € generates a maximum voltage of 1.1 mV, utilizing a 45 µm DS for the printed SU-8 layer.

These achievements culminated in the publication of four scientific articles presented in this thesis (two already published, one accepted for publication and one under review), the filling of a European patent application.

6 ANNEX

6.1 Design and manufacture of measurement setups

In the thesis, two customized characterization setups were developed to acquire essential data for the research. In this chapter, we present in detail the process of designing and manufacturing these two characterization setups, highlighting their key components and operation, as well as their importance in obtaining significant results in the context of this thesis.

6.1.1 Design and manufacture of a triboelectric material measurement setup

To perform the proper characterization of triboelectric materials, a measurement setup consisting of a support table (Thorlabs® PBH51501), a custom-made Faraday cage, and a motion part using a stepper linear motor was implemented (Figure 15a-c).

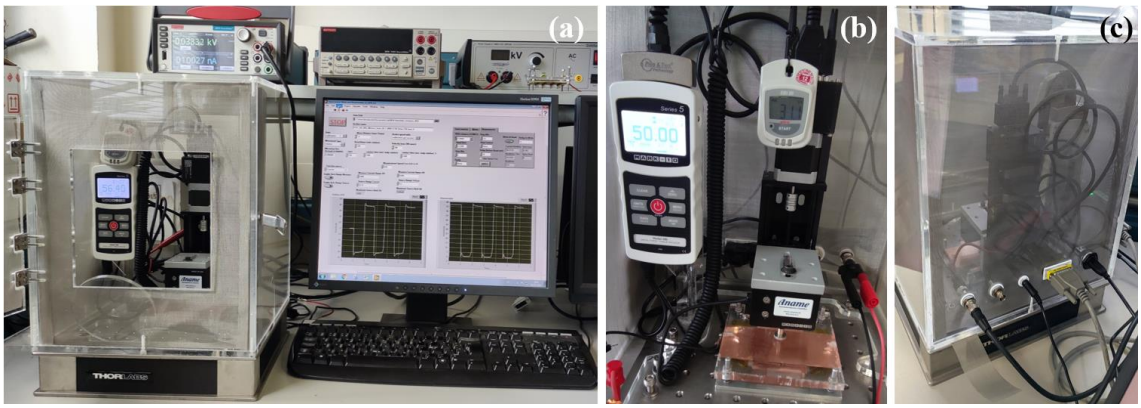


Figure 15: *(a) Measurement system comprised of a support table, Faraday cage, and stepper linear motor. (b) Rear panel of connections of the measurement system. (c) Expanded interior of the measurement system.*

As shown in Figure 15a-b, the system includes a stepper linear motor (Zaber® LSQ075B-T3-MC03 and X-MCB1-KX13B), a dynamometer (Mark M5i with an MR03-20 sensor for measuring up to 100 N of force), a sourcemeter (Keithley® 2470), and LabVIEW® software specifically designed for this purpose, which controls the electrical setup and data acquisition. At the rear of the measurement setup shown in Figure 15c, the connections of the measurement setup are located, where the power and data connectors of the different instruments can be observed, and there are two BNC connectors that can be used to connect the device/material to be measured to the corresponding instrument (in this case, only a single connection to the sourcemeter is needed).

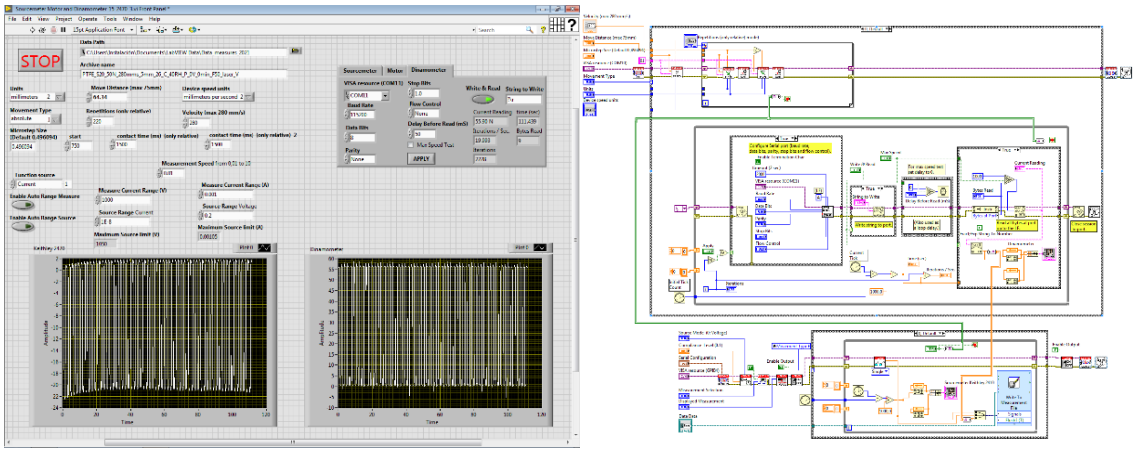


Figure 16: *LabVIEW® program specifically designed for the characterization of triboelectric materials.*

The linear motor is capable of vertically displacing up to 75 mm and bringing the materials into contact with each other by applying a specific force. The LabVIEW® software, shown in Figure 16, allows the configuration of various parameters, such as displacement, speed, contact time, and number of repetitions. Additionally, through the LabVIEW® software, the type of measurement (current or voltage) and the sampling frequency can be selected.

Finally, the design of the box containing the measurement setup is presented in Figure 17. During the manufacturing process, the Epilog Mini 24 laser was used to cut PMMA elements that compose the box.

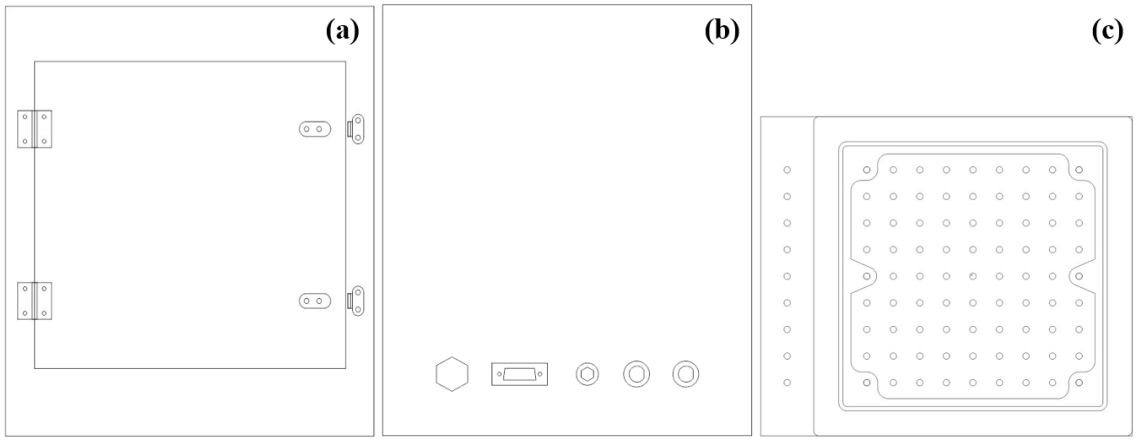


Figure 17: *Design of the box containing all the elements that compose the measurement setup. (a) Front panel, (b) Rear panel, and (c) Base fixed to the support table.*

6.1.2 Design and manufacture of Helmholtz coils for MFs

To characterize an EH device that uses MFs as a residual energy source, a measurement setup that emulates the MF of a possible real-world application must be designed. Helmholtz coils are fundamental tools in research and experimentation involving MFs, as they offer precise control and the necessary stability to obtain reliable and reproducible results. For this reason, the design and manufacture of such a coil for laboratory measurement experiments were decided upon.

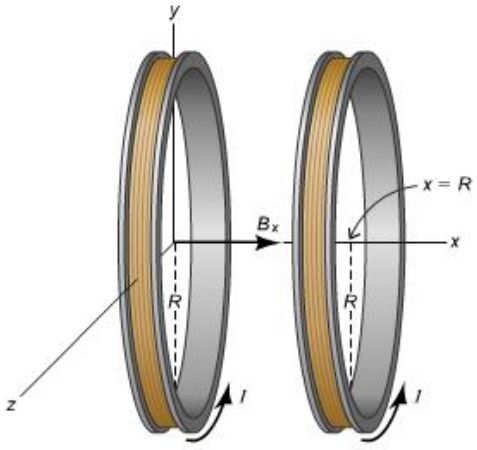


Figure 18: *Configuration diagram of the Helmholtz coils*

To design the Helmholtz coils, a maximum magnetic flux limit of 1000 µT was established to avoid serious interference in the measurements and effects on other laboratory setups. Helmholtz coils are one of the most common configurations for generating a constant and adjustable MF. The expression of the MF in a Helmholtz coils configuration for a point x (axis of Figure 18), with the coils in parallel, is as follows:

$$\vec{B}(x) = \frac{\mu \cdot I \cdot R^2}{2} \cdot \left[\frac{n_1}{((x-\frac{d}{2})^2+R^2)^{3/2}} + \frac{n_2}{((x+\frac{d}{2})^2+R^2)^{3/2}} \right] \hat{x}\ [T] \quad (3)$$

Where $\mu \cong \mu 0 = 4\pi\ 10^{-7}\ N/A^2$ corresponds to the permeability of air, I is the current from the source in amperes (A), R is the radius of the coils of equal size in meters (m), n_1 and n_2 are the number of turns of coils 1 and 2, respectively, and d is the distance between the coils in meters.

To design the Helmholtz coils, different parameters were set based on the available materials. The coil radius was set at R = 12.75 cm from the internal radius of a recycled

polypropylene water pipe. The distance between the coils was commonly designed as d=R to simplify the expressions. For the current I and the number of turns n = n_1 = n_2, a large number of turns were desired to prevent high currents from flowing through the cable. According to Equation 3, the number of turns of the MF was set at 140 to approximately match the equivalence of 1 mA = 1 µT.

An AWG 24 gauge wire, American standard, was selected for the Helmholtz coils. Although the manufacturer specifies a maximum continuous current of 577 mA, this turns out to be a conservative value. Since the coil operates for short periods, it is possible to reach currents of up to 1 A to achieve the desired maximum magnetic flux of 1000 µT without damaging the conductor.

To calculate the temperature rise of the wires, the following Equation 4 relating heat and temperature was used:

$Q = m \cdot c \cdot \Delta T\ [J] \rightarrow \ \Delta T = \frac{Q}{m \cdot c}\ [°C]$ (4)A copper conductor (although galvanized) with a specific heat capacity of c = 0.386 J/°C·g, a density of ρ = 8.89 g/cm³, a diameter of 0.5 mm, and a total length of 112 m per coil was considered. The real impedance per coil was calculated as 9.75 Ω.

From the calculations, it was determined that the temperature rise per minute is approximately 7.75 °C. As a result, for short operating times, it was determined that the coil can operate with a maximum magnetic flux of 1 mT (approximately equivalent to 1 A of current).

Once the configuration to generate the MF was established, the design of the coil structure proceeded. During the manufacturing process, the Epilog Mini 24 laser was used to cut PMMA elements. The Helmholtz coils designs in CorelDRAW are presented in Figure 19a, while Figure 19b shows the final manufactured Helmholtz coils configuration.

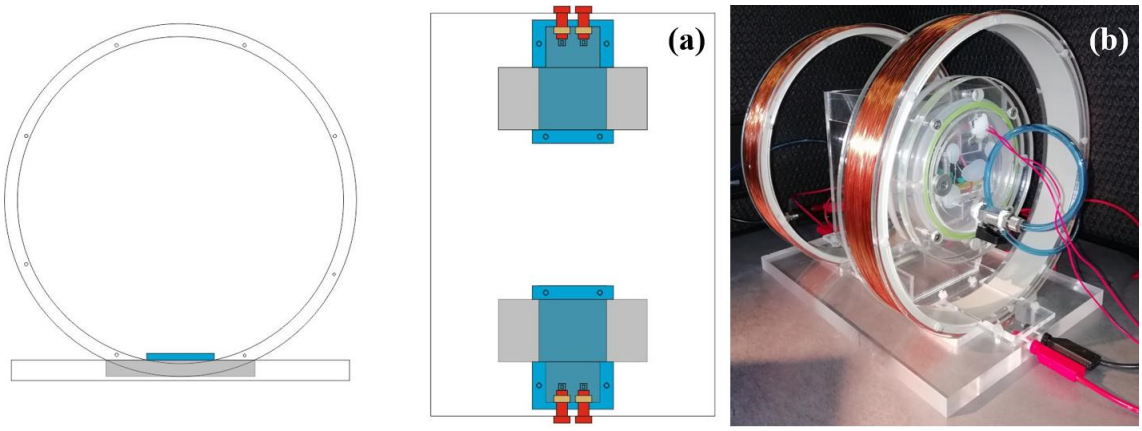


Figure 19: *(a) Design of the Helmholtz coils in CorelDRAW. (b) The final manufactured coils*

.

6.2 Array of nickel mass cantilevers

The previously presented article "Piezoelectric MEMS resonator with magnetic tip mass for EH from ultra-low intensity magnetic field" in this thesis illustrates how, through a standard microelectronics manufacturing process and subsequent assembly by pick-and-place of a neodymium magnetic mass, an EH device capable of harvesting energy from very low MFs for powering ultra-low power sensors can be obtained.

The next step in this research is the utilization of a manufacturing process in which all its fabrication steps are compatible with microelectronics manufacturing techniques. Furthermore, to increase the generated energy, it is also proposed to manufacture an array with 10 of these devices in parallel. By incorporating 10 resonators on the same chip, the power density would be considerably increased.

6.2.1 Manufacturing process

As mentioned previously, the purpose of this process is to achieve complete fabrication using microfabrication techniques commonly employed in cleanroom environments. In the following representation, shown in Figure 20a-b, a schematic configuration and a cross-sectional diagram of a single device are exhibited for clarity.

The fabrication process of this new device is described in Figure 20c. These devices, like their predecessors, will be based on SOI wafers. Initially, a 1 µm SiO_2 thermal growth is carried out to isolate the device from the structural silicon part. Then, a layer of Cr/Pt of 20 nm and 200 nm is deposited by RF reactive sputtering to define the bottom electrode.

The 20 nm Cr layer is used as an adhesion layer for Ti. The same technique is employed to deposit the 1 µm thick AlN layer and the top electrode, again of Cr/Pt of 20 nm and 200 nm.

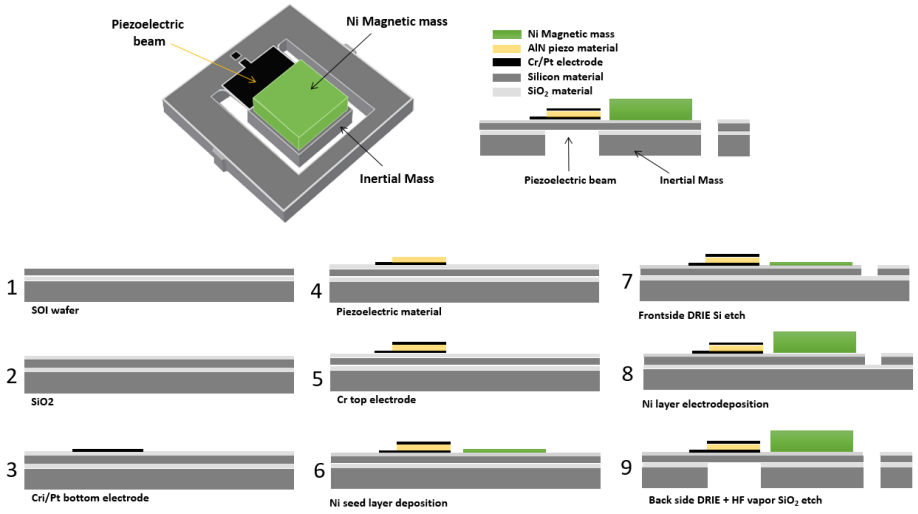


Figure 20: *(a) Schematic of the functional configuration of the device with a cantilever structure and a magnetic tip mass. (b) Cross-sectional diagram of the cantilever structure. (c) Different stages of the fabrication process are included*

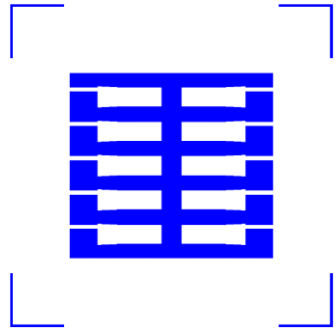
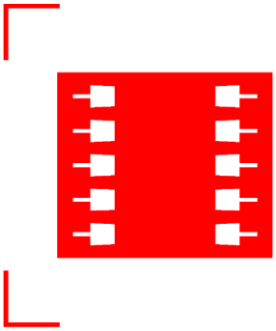
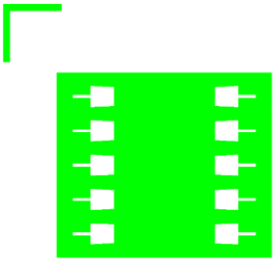
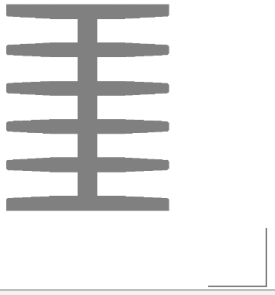
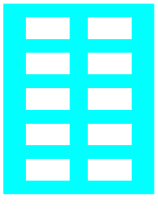
Before proceeding to the structuring of the device, 100 nm of Ni is deposited as a seed layer for subsequent electrodeposition. Then, through RIE, the cantilever part of the device is defined using the silicon component zone. Subsequently, a 50 µm resin is deposited which will serve as a mask for the electrodeposition of 25 µm of Ni at the tip of the cantilever. This Ni tip mass is the one that will interact with the MFs. Finally, through DRIE, the rest of the structure and the silicon mass at the tip of the cantilever are defined. To release the devices, a wet etching process based on HF is used to remove part of the buried oxide layer, subsequently releasing the cantilever beam.

6.2.2 Mask design

For ease and cost reduction, the vast majority of masks for this process will be defined for use through direct laser photolithography (DWL). The only layers that will be designed to use conventional glass masks will be the layer that defines the Ni magnetic mass because we need a resin with a non-standard thickness of 50 µm and the DRIE mask because the front alignment marks need to be aligned with the back of the wafer for

subsequent etching. The Table 3 shows the design of the layers to be used in the different stages of the array device fabrication process.

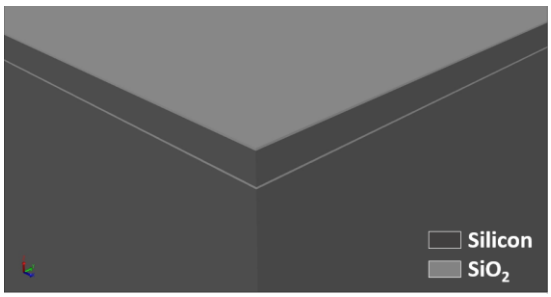
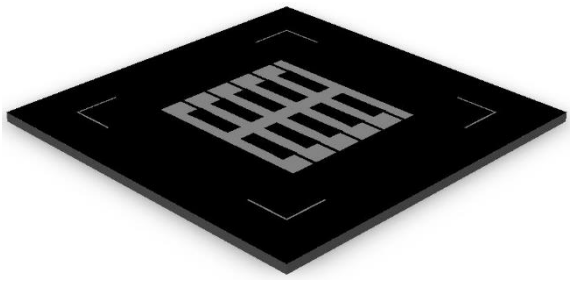
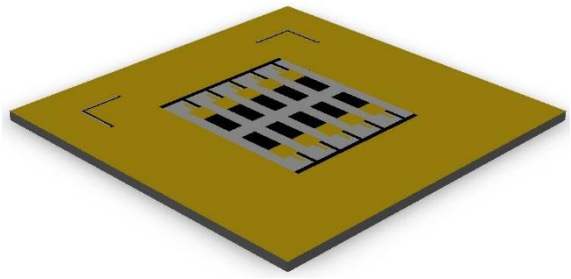
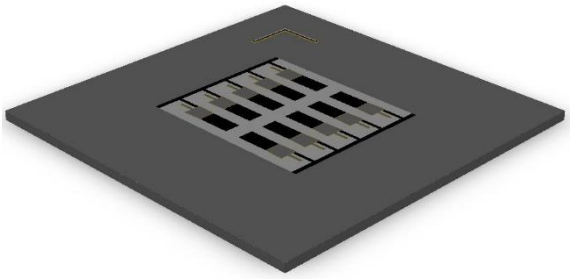
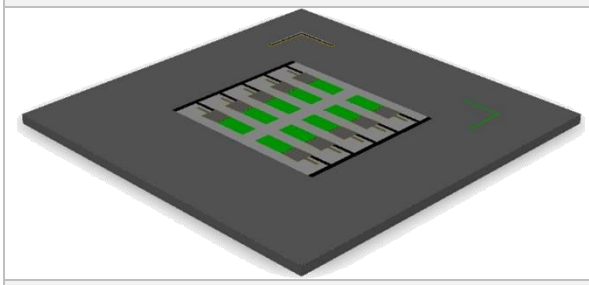
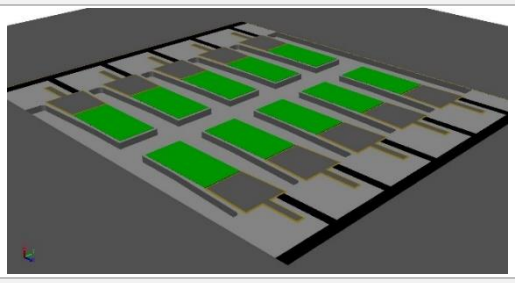
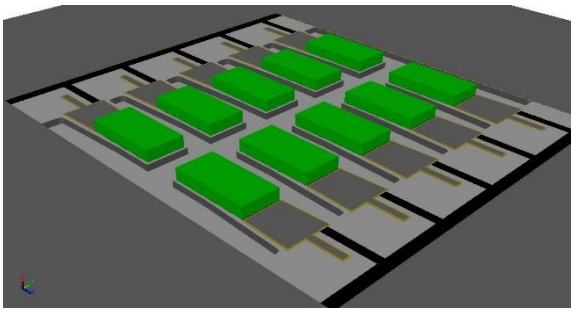
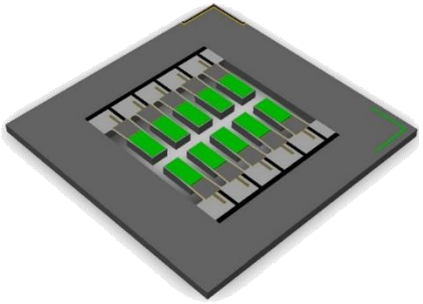
***Table 3**. Table of the different layers designed for a single chip.*

	
Layer 1 - **P**olarity positive	Layer 2 - Polarity negative
	
Layer 3 - **P**olarity positive	Layer 4 - Polarity negative
	
Layer 5 - **P**olarity **negative**	Layer 6 - Polarity negative

6.2.3 Fabrication process simulation

Below is Table 4 with the different simulated manufacturing steps that will be used for the device fabrication. As mentioned earlier, these devices are based on SOI wafers.

Table 3. Table with the different simulated manufacturing steps for a single chip.

	
Thermal SiO_2 growth	Bottom electrode metal deposition
	
AlN deposition	Top electrode metal deposition
	
Ni seed layer deposition	Frontside silicon etching
	
Ni mass electrodeposition	Backside silicon etching

This manufacturing process is already running in the cleanroom of the IMB-CNM (CSIC), as an improvement of the concepts presented in this thesis. Due to the equipment conditioning and cleanroom rearrangements that is facing the institute currently, it is expected to finalize the manufacturing of these devices in six or nine months. Therefore, the analysis of the fabrication results and the performance of these new devices are out of the scope of this thesis.

6.3 Patent: monolithic functional structures and method for their production

DESCRIPTION

Field of the invention

The present invention belongs to the field of electrically-powered functional structures, specifically to monolithic functional structures comprising at least a functional structure (such as a resonator, a sensor, an energy harvester, etc.) and at least a piezoelectric material. The invention refers both to such a monolithic functional structure, and to a method for 3D printing such monolithic functional structure.

Background art

There is a need to provide reliable and non-wasteful electrical energy sources for functional structures (such as resonators, sensors, energy harvesters, etc.) which require the use of electrical energy and are highly dependent on such electrical energy source.

For example, the large increase in the Internet of Things (IoT) has led to a huge growth in the development of very low-power sensors that communicate with each other and form a large wireless network. The greatest difficulty in the expansion of the IoT is the energy dependence of the sensors, limited by the use of their batteries. For this reason, we are facing a great barrier due to the high cost of replacing batteries and the environmental impact that it entails. Other monolithic functional structures (resonators, sensors, energy collectors, etc.) face the same shortcomings due to their dependence on electric energy from batteries.

The current solution is to provide batteries as an electrical power source for these functional structures (such as sensors). However, batteries entail a shortcoming due to their high cost, their need for replacement, and the associated environmental impact.

Hence, an alternative for the supply of electrical energy to such functional structures (such as sensors) is required in the field which overcomes these shortcomings. Such alternative with its corresponding advantages is the object of this patent application and will be made apparent throughout its description.

Summary of the invention

On the one hand, there are materials such as piezoelectric materials, which allow harvesting residual environmental energy (such as movement, vibrations, magnetic fields, light, heat, etc.) and converting it into electrical energy. An example of a device which can convert mechanical energy into electrical energy are piezoelectric transducers. In vibrational energy harvesting, piezoelectric materials are one of the most widely used transducers. An example of such piezoelectric materials are piezoceramics, such as the lead zirconate titanate (PZT). An advantageous piezoelectric material is PVDF and its copolymers since it does not contain toxic materials such as lead.

On the other hand, there exists the technique of three dimensional (3D) printing or additive manufacturing (AM), which is a process of making three-dimensional solid objects from a digital file. This technique allows the production of many custom-designed products, in a wide array of fields including agriculture, healthcare, automotive, aerospace, etc.

Briefly, AM technologies are based on three types of processes:

1. Synthesis, in which the temperature of the material is raised without liquefying it to create high-resolution prototypes,
2. Fusion, in which powders are fused by means of electron beams, and
3. Stereolithography, which uses a method called photopolymerization, which uses an associated ultraviolet laser.

The present invention proposes to integrate together a monolithic functional structure (resonators, sensors, energy harvesters, etc.; preferably a low power sensor) and at least one piezoelectric material (which converts ambient energy into electrical energy usable by the monolithic functional structure), to be produced by 3D printing, in order to create monolithic 3D piezoelectric devices. The functional structure carries out the intended function of the device (that of a resonator, a sensor, an energy harvester, etc.), while the piezoelectric material converts the residual energy of the device and the environment into electrical energy to be used by the functional structure.

The term “functional structure” according to the present invention refers to a mechanical structure capable of exerting a mechanical stress on the piezoelectric layer, typically a resonator or mechanical stressor, which causes a reaction in the electrical device so that the device carries out its corresponding function or purpose of sensor, low-power sensor, energy harvester or actuator device.

The term “low power sensor” is known in the state of the art and refers to sensors that work using little energy or power. When several low power sensors connected in networks they operate as a type of wireless technology. This means that they have the benefits of wide-area mobile networks at a lower cost. They do not allow for large data transfers, so are not used for human communications (voice, video, and other communications that transfer large volumes of data). However, their capacity to connect devices across wide distances makes them useful for Internet of Things (IoT) technologies and other machine-to-machine communications. Long-range, low-power sensor networks can be deployed over large areas to collect data that can be analysed and developed into predictive models to drive strategic decisions. They can also be integrated into existing products to add intelligent features that will make them more appealing to users and to gather usage data to improve their performance over time.

The term “functional structure material” according to the present invention refers to the type of material that is used to fabricate the functional structure.

The term “piezoelectric material” according to the present invention refers to any material which is capable of transforming residual or environmental energy into electrical energy.

The term “monolithic” in “monolithic functional structure” according to the present invention, refers to the fact that components of such structure, including the at least one functional structure and the at least one piezoelectric material, are integrated within a single piece or structure, or are part of a single piece or structure.

The term “compact” according to the present invention refers to the fact that the different components are connected with physical direct contact between them, and without the need for loose parts or assembled part to connect them.

A non-limiting example of such a monolithic piezoelectric device is a sensor functional structure (such as a low power sensor) together with a PVDF piezoelectric material. For example, a compact and electrically bonded sensor and PVDF material, printed as a single piece by 3D printing. Another non-limiting example is a piezoelectric energy harvester, such as an energy harvester together with a PVDF piezoelectric material.

Examples of piezoelectric materials to be used according to the invention are lead zirconate titanate (PZT), Polyvinylidene fluoride (PVDF) or their copolymers, like PVDF-TrFE (copolymer of Polyvinylidene fluoride and trifluoroethylene) and PVDF-TeFE (copolymer of Polyvinylidene fluoride and tetrafluoroethylene), and their combinations thereof.

Therefore, this solution allows, by 3D printing in a single printing step, obtaining a compact part which comprises both components (at least a functional structure and a piezoelectric material) integrated within, which in addition to comprising and performing the function of the functional structure, also allows the collection of environmental energy and its transformation into electrical energy by the piezoelectric material.

The 3D printing method to obtain monolithic functional structures according to the invention, results in the advantages of being an easier, cheaper, and highly customizable method (compared to other fabrication methods of functional structures such as a sensor) and allows simultaneously producing the functional structure and the piezoelectric material in the same printing process and as a single piece, without the need for assembling different parts.

In fact, the 3D printing of monolithic functional structures according to the invention, is simpler since it does not require to further assembly steps or tools and does not require molds. Moreover, it allows rapid and customizable changes of design and the easy fabrication of complex monolithic functional structures. What is more, the 3D printing method according to the invention also allows integrating computer-implemented design software (such as CAD), which allows the full-customization of the monolithic functional structures, for example allowing their full adaptation to the environmental conditions in which such structure is planned to be used.

The obtained monolithic functional structure is compact, is cheaper, and has very low environmental impact since its electrical energy source (the piezoelectric material) does not need to be replaced or disposed of, and the structure is capable of reusing residual energy from the structure or its environment. Moreover, the compactness of the monolithic functional structure is advantageous in making the piezoelectric material contained within more efficient in converting the residual energy of the part (mechanical, light, heat) into electrical energy, due to the fact that its compactness and integration avoid losses due to electrical transmission, because the device itself has its own support and does not need to be externally attached to a support. In other words, the better bonding between the functional structure and the piezoelectric material, helping to convert and transmit more of the residual energy into electrical energy to be used by the functional structure.

Figure 1 illustrates schematically the advantage of integrating piezoelectric materials by 3D printing to create monolithic 3D-printed piezoelectric devices, according to the present invention. In this way, it is possible to adapt the functional structure (such as a resonator, an energy harvester, or a sensor, etc.) to the different needs, and with its own self-integrated electrical energy source, in a fully customizable manner, and without the need for subsequent assembly which entails an easier and cheaper production method, as well as a cheaper final product device.

The invention hence refers to the fabrication of monolithic functional structures (such as resonators, sensors, energy harvesters), by using 3D printing, and by printing in the same process the layers of the functional material and the piezoelectric material.

Preferably, the three-dimensional (3D) printing technique used to produce the monolithic functional structures of the present invention is Fused Deposition Modeling, which is a process of material extrusion used to fabricate thermoplastic pieces by extrusion and deposition of materials layer by layer.

A first aspect of the invention refers to a monolithic functional structure, characterized in that is comprises:

- at least a functional structure made of a functional structure material; and
- at least a piezoelectric material;
- wherein the functional structure and the piezoelectric material are part of a single piece;
- wherein the functional structure and the piezoelectric material are electrically connected; and
- wherein the piezoelectric material is not located along the neutral axis of the monolithic functional structure.

The “neutral axis” in the present invention herein refers to the axis across the monolithic functional structure along which there are no longitudinal stresses or strains.

The functional structure is a mechanical structure capable of mechanically stressing the piezoelectric layer, typically a resonator or a mechanical stressor.

The device, that is the monolithic functional structure, further comprise a substrate (for example a glass substrate) on top of which the functional structure and the piezoelectric material are located. 3D printing of the at least a functional structure and of the at least a piezoelectric material, is carried out on top of the substrate.

The at least one piezoelectric material can collect the residual environmental energy (for example movement, vibrations, magnetic fields, light, heat, etc.) and transform it into electrical energy, which can be used by the functional structure of the monolithic functional structure to power it so that it can carry out its function. This allows the electrical powering of the functional structure which carries out the function of interest of the device (for example a sensor) without the need for batteries or external power sources.

In a preferred embodiment, the functional structure material of the monolithic functional structure is selected from PLA (polylactic acid), ABS (acrylonitrile butadiene styrene), PVA (polyvinyl alcohol), PP (polypropylene), tough PLA (tough polylactic acid), CPE (co-

polyester), PET-G (glycol-modified polyethylene terephthalate), Nylon (polyamide), PC (polycarbonate), and any combination. Preferably the functional structure material is selected from PLA or tough PLA or combinations thereof, more preferably tough PLA.

The term “tough PLA or tough polylactic acid” as used herein refers to a special type of PLA, called Tough PLA, combines the ease of printing with increased mechanical performance. Specifically, tough PLA has increased impact resistance, avoiding the typical brittle failure of normal PLA. Tough PLA is used for functional prototyping tooling and manufacturing aids.

In another preferred embodiment, the functional structure material is a printed material. In another more preferred embodiment, the functional structure material comprising at least one layer of printed structural material. In another even more preferred embodiment, the functional structure material has a region of the said layer of functional structure material is left empty as a depression. In another a most preferred embodiment, the functional structure material comprising more than one layer of printed structural material wherein said left empty region is located on the top and last structural printed layer.

In another preferred embodiment, the piezoelectric material of the monolithic functional structure is zirconate titanate (PZT), Polyvinylidene fluoride (PVDF) or their copolymers, such as PVDF-TrFE (copolymer of Polyvinylidene fluoride and trifluoroethylene), PVDF-TeFE (copolymer of Polyvinylidene fluoride and tetrafluoroethylene), or combinations thereof.

In another preferred embodiment, the substrate material is selected from glass, metal such as gold, silver, copper, aluminum, iron, nickel, titanium, platinum, cobalt, lithium.

Preferably the substrate is glass. Moreover, once the monolithic functional structure is fabricated, the substrate can be either kept as part of the monolithic functional structure or be removed from it.

In another preferred embodiment, the functional structure of the monolithic functional structure is a low-power sensor.

In another preferred embodiment, the monolithic functional structure is a monolithic energy harvester structure with PVDF as the piezoelectric material.

In another preferred embodiment, the at least one functional structure and the at least one piezoelectric material of the monolithic functional structure, are at least in partial physical contact with each other. The advantage of said embodiment is that by being in direct contact, the conversion of residual energy and thus the transformation into electrical energy is more efficient.

In another preferred embodiment, the monolithic functional structure further comprising a conductor material, preferably said conductor material is selected from an electrically conductor wire, a conductive track and a metal layer, such as gold, silver, copper, iron, nickel, titanium, platinum, cobalt; more preferably the conductor material is a metal layer, more preferably is a copper metal layer.

In another more preferred embodiment, the conductor material is located in contact with the functional structure.

In another preferred embodiment, the monolithic functional structure is characterized in that it comprises from bottom to top:

- at least a first layer of functional structure material comprising at least one layer of printed structural material, wherein a region of the said layer of functional structure material is left empty as a depression, wherein a metal layer, preferably copper, applied in such region;
- at least a second layer of functional structure material comprising at least one layer of printed structural material on top of the first layer of functional structure material, wherein at least the top of the metal layer is left uncovered;
- a layer of piezoelectric material on top of the first layer of functional structure material, at least partially in contact with the metal layer;
- at least a third layer of functional structure material comprising at least one layer of printed structural material on top of the piezoelectric material layer and on top of the second layer of functional structure material, wherein at least a region on

the top of the metal layer and a region on the top of the piezoelectric material layer are left uncovered;

- an electrical connector selected from a metal wire or a metal spring load, located in both of the regions left uncovered on top of the metal layer and on top of the piezoelectric material layer.

The electrical connector may be any type of connector which allows a connection between the metal layer and the piezoelectric material layer.

The term “structural layer or first, second, third structural layer” in the present invention refers to a layer that comprising at least one layer of the structural layer material a layer obtained by any method, whether by printing, by the additive method or by any deposition technique known to the state of the art. Evidently, it contains as many layers of material as necessary in any functional structure material layer or in the first, second or third structural layers indicated; and where in the first and second layers, the last layer of material that makes up each structural layer has an area without material leaving a gap to house the metallic layer or the corresponding piezoelectric. The combination of the different layers of structural material together constitutes the functional structure of the device.

The monolithic functional structure may comprise at the bottom a substrate, in the case that the substrate on which the 3D printing of the monolithic functional structure was carried out, is not finally removed from such structure.

A second aspect of the invention refers to a method for the 3D printing of monolithic functional structures, characterized in that it comprises the steps of:

a) providing a substrate, preferably a glass substrate;
b) printing at least one layer of a first functional structure material that comprising at least one layer of printed structural material on the substrate of the step (a), preferably PLA, without applying functional structure material to at least a region of the last printing layer;
c) applying metal in such a region of the step (b), preferably copper,

d) optionally, printing at least one layer of a second functional structure material that comprising at least one layer of printed structural material, preferably PLA, without applying functional structure material at least on top of the region where the metal has been applied in step (c),
e) applying a piezoelectric material, preferably Polyvinylidene fluoride, on top of the layer where the metal has been applied in step (c), preferably at least partially in direct contact with the metal,
f) printing at least one layer of a third functional structure material that comprising at least one layer of printed structural material, preferably PLA, without applying functional structure material on top of at least a region of the metal of step (c) and on top of at least a region of the piezoelectric material of step (e), and
g) placing at least an electrical connector in both of the regions left uncovered on top of the metal and on top of the piezoelectric material of step (f).

In a preferred embodiment according to the second aspect of the invention, the 3D printing is carried out by Fused Deposition Modelling.

In another preferred embodiment according to the second aspect of the invention, the method uses computer-implemented design (CAD) software in order to design the monolithic functional structure to be 3D printed.

In another preferred embodiment according to the second aspect of the invention, a model created by computer-implemented design (CAD) software is sliced into layers using slicing software.

In another preferred embodiment according to the second aspect of the invention, the applied metal in step c) of the method is selected from gold, silver, copper, aluminum, iron, nickel, titanium, platinum, cobalt, lithium, or their alloys; preferably copper.

In another preferred embodiment according to the second aspect of the invention, the at least one electrical connector placed in both of the regions, in step g) of the method, is selected from a metal wire or a metal spring load.

In another preferred embodiment according to the second aspect of the invention, the metal of the metal wire or metal spring load is selected from gold, silver, copper,

aluminum, iron, nickel, titanium, platinum, cobalt, lithium, or their alloys; preferably copper.

In another preferred embodiment according to the second aspect of the invention, the functional structure material is selected from PLA (polylactic acid), ABS (acrylonitrile butadiene styrene), PVA (polyvinyl alcohol), PP (polypropylene), PLA Tough, CPE (co-polyester), PET-G (glycol-modified polyethylene terephthalate), Nylon (polyamide) and PC (polycarbonate) and any combination thereof; preferably PLA, and even more preferably tough PLA.

In another preferred embodiment the substrate is selected from glass, metal such as gold, silver, copper, aluminum, iron, nickel, titanium, platinum, cobalt, lithium. Preferably the substrate is glass.

In another preferred embodiment the process further comprises an additional step of removing the substrate of the monolithic material obtained in step (g).

A third aspect of the invention refers to the use of monolithic functional structure described above as a sensor, low-power sensor, self-powered sensor, energy harvester or actuator.

In another preferred embodiment the use of the monolithic is as a low-power sensor for the creation of a large wireless network wherein the low-power sensors communicate with each other.

In 3D printing, as can be seen in Figure 2 the process begins with designing the desired piece using 3D design software, typically design CAD software (for example Tinkercad®, https://www.tinkercad.com). This design by CAD software allows to optimize both the function of the device as well as the collection and conversion of residual environmental energy into electrical energy by the piezoelectric material. Once the design is completed, the next step is exporting the file in STL (Stereolithography) format. The STL file contains all the necessary information about the 3D object. Subsequently, the CAD model is sliced into layers using slicing software such as “Ultimaker Cura 4.13.1”. Finally, the object is printed by transferring the file, positioning and printing the design layer-by-layer. This process is schematically summarized in Figure 2.

The 3D printing manufacturing process according to the invention process additionally includes two additional steps, in order to introduce the bottom electrode and the piezoelectric material (such as PVDF material).

The piezoelectric material preferably comprises two metallic electrodes, noted in this description as “bottom electrode” and “top electrode”. The bottom electrode and the top electrode may be made of any electrically conducting metal, for example gold, silver, copper, aluminum, iron, nickel, titanium, platinum, cobalt, lithium, etc; preferably copper.

The first step (as shown in Figure 3a), is providing a substrate (for example a glass substrate) onto which to print the monolithic functional structure. First of all, some layers of a “functional structure material” (such as PLA) are printed onto the substrate, layers which will serve as the bottom of the final structure which will encapsulate the piezoelectric material within the structure (Figure 3a). Hence, the material of this encapsulation layer will be referred to as “functional structure material”. It was observed that the thinner the printing layer of functional structural material, the greater the power output from the printed monolithic functional structure. Preferably, the thickness layer to be printed by the nozzle for each printing layer is between 60-150 µm, even more preferably 100 µm, which allows to ensure good quality and avoid pushing the limits of the printer head.

The bottom of the encapsulating layer preferably comprises two to three printed layers. This low number of layers (2-3 layers) will help to maintain the high quality of the encapsulating layer and also increase the stress received by the piezoelectric material, which increases the electricity generated by the piezoelectric material. The more stress is achieved, the more charge is generated in the piezoelectric material. Additionally, a small region (such as a hole) is left uncovered on the material’s surface, at least left unprinted in the last printing layer. In this small region (such as a hole) the metal that will serve as the electrode will be placed (for example a lower copper electrode).

Subsequently, metal or a metal piece (for example a copper piece) is applied inserted to establish the connection with the bottom electrode, in such small region (as shown in Figure 3b).

At this stage, optionally and additionally one or more layers of the encapsulating material (such as PLA) can be applied on top of the previously applied encapsulating material layers, as long as the small region (such as a hole) where the metal for the electrode has been applied, is left uncovered (Figure 3c).

Then, a layer of piezoelectric material is printed by the nozzle and deposited on top of the metal electrode material, such that the piezoelectric material is at least partially in direct contact with the metal electrode material (as shown in Figure 3d). Afterwards, the remainder of the encapsulating layer material (such as PLA) is printed layer by layer, such that the remainder of the monolithic functional structure is printed (as shown in Figure 3e). In the final printing stage, at least a partial area of both the electrode material (for example copper) and the piezoelectric material (for example PVDF) are left uncovered (as shown in Figure 3e). This allows that, upon completing the print, electrical connectors (metal connectors such as metal wires or metal spring loads, preferably gold connectors) are inserted to facilitate the connection between the at least one copper electrode and the piezoelectric material (as shown in Figure 3f).

The material to be printed layer-by-layer for the encapsulating layer according to the invention can be any polymeric material printable by 3D printing. Non-limiting examples of such 3D printing materials are PLA (polylactic acid), ABS (acryloni-trile butadiene styrene), PVA (polyvinyl alcohol), PP (polypropylene), PLA Tough, CPE (co-polyester), PET-G (glycol-modified polyethylene terephthalate), Nylon (polyamide) and PC (polycarbonate); preferably PLA, and even more preferably tough PLA. PLA has the advantages that it is a biodegradable and recyclable polymer that is a reliable and easy-to-print material that can be printed at low temperatures. It has a low shrinkage factor and does not require the use of a heated build plate.

All in all, the present invention entails the 3D printing of 2 pieces (a functional structure, and a piezoelectric material that can be either printed or integrated within the monolithic

functional structure) as a compact single structure, such that the resulting monolithic functional structure can carry out the function of the functional structure (resonator, sensor, energy harvester) while also making use of the residual environmental energy in order to convert it into electrical energy that is transmitted to the functional structure to make use of it, providing the aforementioned advantages, which can be summarized as:

- No need for batteries or other non-renewable and wasteful energy sources.
- Making use of the residual energy of both the monolithic functional structure and its environment.
- Higher conversion efficiency of the residual energy into electric energy (due to the better mechanical and electrical connection between the piezoelectric material and the functional structure)
- Higher compactness and integration of the structure (as compared to the functional structure and the piezoelectric material as two individual components).
- Manufacturing of the whole monolithic functional structure by a single technique (3D printing) and in a single printing process.
- Both structures (functional structure and piezoelectric material) printed as a single structure.
- No need for assembly between both structures (as both structures are printed as a single piece)

This invention represents a contribution to the ongoing trends and future sustainability of self-powered functional structures, such as sensors. By harvesting ambient energy, self-powered sensors have the potential to reduce the environmental impact associated with batteries.

Last but not least, the scope of the present invention is not limited to the embodiments explicitly disclosed in this document, and the person skilled in the art understands that other embodiments which are alternative or equivalent, including modifications which are equivalent or obvious, are within the scope of protection of the present invention.

Description of the Figures

Figure 1. schematically represents the integration of a functional structure and a piezoelectric material as a single monolithic functional structure produced by 3D printing.

Figure 2. schematically represents the basic process of 3D printing carried out by 3D printers and their software, in order to create 3D objects.

Figure 3. schematically represents the different steps a-f of the Fused Deposition Modelling 3D printing process according to the present invention. The sequences of steps to create the a particular embodiment of a monolithic functional structure according to the invention are: (a) PLA base layer printing for encapsulation of the piezoelectric material; (b) placement of copper material to make the connection of the bottom electrode; (c) PLA layer printing for later assembly of the piezoelectric material; (d) placement of the piezoelectric material (PVDF); (e) printing of the rest of the PLA structure leaving two holes for subsequent connections and (f) insertion of gold connectors, for the connection of the two electrodes of the piezoelectric material.

Figure 4. shows pictures of a monolithic energy harvester structure with PVDF as piezoelectric material, manufactured by Fused Modelling 3D printing, according to the invention. In Figure 4 the result of the different steps of the 3D printing process according to the invention to create the monolithic energy harvester structure are shown: (a) PLA printing base layer for encapsulation of the piezoelectric material (also schematically shown in Figure 3a), and placement of copper material to make the connection of the bottom electrode (also schematically shown in Figure 3b); (b) placement of the PVDF piezoelectric material (also schematically shown in Figure 3d); (c) next, PLA layer printed after the placement of the PVDF material, leading to its partial encapsulation (also schematically shown in Figure 3e); and (d) printing of the rest of the PLA structure leaving two small regions uncovered (holes) for subsequent electrical connections (schematically shown in Figure 3e).

Figure 5. schematically shows a) a cross-section of the energy harvester with the specified dimensions; (b) a view of the 3D design used for the energy harvester; and (c) the stress

distribution when the harvester resonates at its resonance frequency, and a detail of the cross-section showing the neutral axis in the software COMSOL Multiphysics®.

Figure 6. represents a graph distribution of the power (in µW) obtained from the energy piezoelectric resonant energy harvester, depending on its dimensions (Figure 6a: dimensions Lb/Lc; Figure 6b: dimensions Tb), and depending on the resistance (in MΩ) from an external circuit than includes a resistor, which allows to determine the optimal load resistor in order to achieve maximum power of the piezoelectric resonant energy harvester.

Figure 7a. represents a graph distribution of the simulation of the power density, power, cost and volume of the piezoelectric resonant energy harvester, depending on its beam thickness (Tb).

Figure 7b. represents a graph distribution of the simulation of the power generated by the piezoelectric resonant energy harvester depending on the depth of the piezoelectric material (Pd) with respect to the surface of the harvester.

Figure 8. represents the first electrical characterization, namely a) the setup for the first electrical characterization using a stepper motor that performs movements of the piezoelectric resonant energy harvester, movements in position from 1mm to 6mm on the Z-axis,; b) graphical representation of the maximum voltage achieved in the setup of Figure 8a. with a displacement of the stepper motor from 1 mm to 6 mm on the Z-axis, with respect to the displacement on the Z-axis, as measured with a Sourcemeter for 6 different 3D printed energy-harvesters, three of these harvesters having their piezoelectric material at 200 µm from the surface of the energy harvester device, while the remaining other three harvesters having their piezoelectrical material at 300 µm. For each from the surface of the energy harvester device; c) Same graphical representation of the same 6 harvesters and displacement from 1-6mm, as those of Figure 8b, but where the Y-axis represents instead the force (N) measured with the displacement by a force sensor attached to the stepper motor, and recorded by means of a dynamometer.

Figure 9. represents the second electrical characterization, namely (a) setup for the second electrical characterization using an electrodynamic shaker at 50 Hz to emulate

environmental vibrations, at different input acceleration levels; (b) Optimal load resistance for maximum power generation with 0.1 G of acceleration; (c,d) Voltage and maximum power for an acceleration sweep from 0.1 G to 1 G and using a frequency of 50 Hz and an optimal load resistance of 4 MΩ.

Figure 10. represents the physical characterization of the piezoelectric PVDF material, namely the thickness and the piezoelectric coefficient, and more precisely a SEM image of the thicknesses of the layers of the piezoelectric material.

Figure 11. graphically represents a simulation of the variation of the output voltage (V) with frequency (Hz), of the resonant piezoelectric energy harvester comprising the piezoelectric material PVDF, by using COMSOL Multiphysics® software, with a set acceleration of 0.5 G. More precisely, Figure 11a represents a comparative of the simulated electrical characterization of the harvesters (curves plotted from 48 to 54 Hz) with the actual electrical characterization of the harvesters (curves plotted from 45 to 55 Hz), for the maximum open-circuit voltage (Y axis) that can be generated by the piezoelectric generator, for the frequency sweep plotted in the figure with an acceleration of 0.5 G. Figure 11b) represents a comparison of the maximum power generated in relation to the depth of the piezoelectric material (200µm and 300µm) and in relation of the load impedance (MΩ).

Figure 12. graphically represents the simulation results for the piezoelectric current sensor by using COMSOL Multiphysics® software: (a) Structure and dimensions used in the simulation; (b) 3D Finite Element modelling (FEM) simulation of the stress distribution in the cantilever beam of the piezoelectric current sensor.

Figure 13. represents a picture (a) and a schematic representation (b) of a piezoelectric current sensor manufactured using 3D printing technology mounted inside a sensor node (current sensor provided by the start-up Energiot); (c) graphical representation of the open-circuit voltage generated by the piezoelectric sensor, depending on the selected power of two heaters, which can obtain up to four different currents (1500 W, 3000 W, 4500 W and 6000 W).

EXAMPLES

A piezoelectric resonant energy harvester has been designed, fabricated, and electrically characterized. In terms of electrical characterization, it was determined that the device can achieve a maximum output power of 1.46 mW when operated with an optimal load impedance of 4 MΩ and subjected to an acceleration of 1 G.

Physical characterization of the piezoelectric material and the final resonator was also performed. In addition, a study and optimization of the device was carried out using finite element modeling (COMSOL Multiphysics®).

Finally, a proof-of-concept device (use-case resonator) was designed and fabricated with the goal of measuring the current passing through a wire.

Material and Methods

1.1. Piezoelectric and Magnetic Materials

The piezoelectric material used in the harvester is a commercially available PVDF film with two parallel electrodes, from TE Connectivity. According to the manufacturer's specification, the PVDF material has a thickness of 110 µm and 6 µm for each silver ink electrode. The piezoelectric coefficient of the commercial PVDF is −33×10−12 m/V, according to the datasheet. The selected material for the structural harvester is "Ultimaker Tough PLA green" from Ultimaker, with a Young's modulus of 2.8 ± 0.15 GPa and a density of 1.22 g/cm^3. A neodymium (Nd) mass with a density of 7 g/cm^3, from the Nd mass provider "Supermagnete", was used as magnet material. Such Nd magnet material can be observed for example in Figure 5a (Nd magnetic mass).

1.2. *Finite Element Modelling*

Finite element modeling (FEM) of the energy harvester was conducted using the software COM-SOL Multiphysics® 6.0. The AC/DC (Electrostatics, Electrical Circuits and Piezoelectricity) and Structural Mechanics (Solid Mechanics and Piezoelectricity) modules of the software, were utilized for the simulation. The model was created using a fine triangular mesh, consisting of over 25,000 elements.

1.3. Manufacturing Process and Characterizations

An “Ultimaker S3 printer” with AA 0.25 mm nozzle was employed for the manufacturing process, allowing printing layers from 60 µm to 150 µm thick. The initial characterization involved a stepper motor from Zaber® Technologies LSQ075B-T3-MC03 (Vancouver, BC, Canada), capable of performing movements from 1 mm to 6 mm on the Z-axis. Concurrently, the voltage generated by the harvester was measured using a Sourcemeter Keithley® 2470 (Cleveland, OH, USA). A force sensor Mark-10® (Copiage, NY, USA) MR03-20 fixed onto the stepper motor recorded the data with the assistance of a dynamometer Mark-10® M5I. An ad-hoc LabVIEW® program controlled the setup comprising the devices.

1.4. Device for electrical characterizations

The electrical characterization was conducted using an electrodynamic shaker VR9500 from Vibration Testing Controller (Jenison, MI, USA) to emulate environmental vibrations at different input acceleration magnitudes. This process was controlled by a customized MATLAB® program, enabling automation, acquisition, and processing of voltage measurements. All data were measured using an acquisition system from National Instruments (Austin, TX, USA) PCI-6132 and a BNC-2110 terminal block.

The piezoelectric coefficient of the material was measured using a Wide-Range d33 piezometer from APC International, Ltd (Mackeyville, PA, USA).

1.5. Design of the Harvester

1.5.1. Definition Fixed Parameters

There are different sources for energy harvesting, such as vibrations, human motion, residual magnetic fields, etc. In this case, we have chosen the magnetic fields generated by a current-carrying conductor. For this reason, the resonance frequency is fixed at 50 Hz (European electric grid frequency).

In order to study structure optimization, an effective area and resonance frequency of the device must be set. In this case, the dimensions are 50 mm × 40 mm (length × width).

1.5.2. Device structure

There are different types of structures for vibrational harvesters, such as cantilevers, doubly-supported beams, or diaphragms. The cantilever results in the highest power

output when used as a piezoelectric energy harvester. Furthermore, the cantilever structure leads to the lowest resonance frequency for a given size. For this reason, the cantilever structure has been chosen.

The resonance frequency of a spring-mass system can be expressed as:

$$f_r = \frac{1}{2\pi}\sqrt{\frac{k_{eff}}{m_{eff}}}, \quad (1)$$

Here, keff and meff represent the effective suspension stiffness and the effective mass values, respectively.

The neutral axis of a beam is the layer in the cross-section of a beam that experiences no longitudinal strain under bending. For composite beam structures, the effect of the different materials of each layer must be summed up to find the neutral axis:

$$Z = \frac{\sum_{i=1}^{n} z_i Y_i h_i}{\sum_{i=1}^{n} Y_i h_i}, \quad (2)$$

where Z is the neutral axis position of the composite beam, Zi is the height of the centroid of layer i, hi is the thickness of layer i, and Yi is Young's modulus of layer i.

1.6. Shape Optimizations and Finite Elements Modeling

1.6.1. Obtaining Resonance Frequency

In addition to the reduction in the manufacturing cost, by having a monolithic device, anchor losses are avoided due to the improved resonator anchor structure. To achieve the desired resonance frequency, a mass with a very large thickness was required due to the low density of the PLA. Furthermore, to achieve actuation with magnetic fields by means of Lorentz's force, a ferromagnetic material is needed as a cantilever tip mass. For this reason, Neodymium (Nd) magnets have been used as an inertial mass.

As shown in Figure 5a, the harvester consists of a PLA cantilever with a length composed of the length of the beam (Lb), the mass (Lm) and the length of the cantilever (Lc).

Moreover, the thickness of the beam has been defined as (Tb), the thickness of the mass as (Tm) and the depth of the piezoelectric material with respect to the surface as (Pd).

The 3D model shown in Figure 5b consists of the energy harvester with the piezoelectric layer inside the structure and an external circuit with a load resistor to calculate the power.

A piezoelectric material produces an electrical charge from mechanical stress. The d33 coefficient represents the piezoelectric charge coefficient along a specific direction, reflecting the material's response to applied stress. It can be expressed as:

$$d33 = \frac{\Delta Q}{\Delta S}, \quad (3)$$

From Equation (2), it can be deduced that the highest stress resulting from a beam deformation in a cantilever is located on the surface. In Figure 5c, the stress distribution is shown when the device resonates at its resonance frequency. It can be observed that the stress on the surface of the material is at its maximum, while it is zero at the center of the beam. Consequently, during the manufacturing process, it is crucial to position the encapsulated piezoelectric material as close to the surface as feasible. However, there is a trade-off, if the piezoelectric layer is too close to the surface, it will not be properly embedded and can get delaminated.

A parametric simulation of Lb and Lm is performed, to find the different combinations to obtain a resonance frequency of 50 Hz. The dimensions of the magnets are more restrictive because they are defined by the manufacturer. A parametric study from 10 mm to 40 mm of Lm is performed. Table 1 shows the different dimension combinations obtained to achieve a resonance frequency of 50 Hz.

L_b (mm)	L_m (mm)	L_c (mm)	Ratio L_b/L_c (%)	Frequency (Hz)
41.20	10.00	51.20	80	50.04
33.10	15.00	48.10	69	49.95
26.80	20.00	46.80	57	50.02
21.60	25.00	46.60	46	50.00
17.15	30.00	47.15	36	50.01
13.35	35.00	45.35	29	50.05
10.20	40.00	50.20	20	49.99

Table 1. Comparative with the different combinations of the parameters to obtain the fixed resonance frequency at 50Hz.

1.6.2. Study of Generated Power

The voltage and power generated by the piezoelectric resonant energy harvester, depending on its different dimensions, are studied using an external circuit that includes a resistor. Performing a sweep of the external resistor, the optimal load resistor can be determined to achieve the maximum power generation for the piezoelectric resonant energy harvester. As shown in Figure 6a, the lower ratio between Lb and Lc, the higher the power output of the piezoelectric resonant energy harvester.

A parametric thickness of the beam under the piezoelectric sheet was simulated to improve the power generated by the piezoelectric generator. Due to the increase in Lb, the natural frequency of the device increases. To compensate for this augment, the density or Tm must be raised. In this occasion, the density of the mass has been augmented to compensate for the frequency. In this way, the dimension of the mass is always the same and simplifies the meshing process during the simulation. As can be seen in Figure 6b, the greater Tb is, the greater the power generated by the harvester.

In the next Table 2, different Tm can be seen to compensate for the increased Tb. In addition, the data of the maximum generated power, volume and power density of each harvester obtained from the simulation are also shown.

T_b (mm)	T_m (mm)	Power (μW)	Volume (cm3)	Power Density (μW/cm³)
1.00	1.00	95	4.10	23.08
1.50	3.48	324	10.20	31.77
2.00	8.13	620	20.80	29.85
2.50	15.46	938	36.80	25.50
3.00	26.12	1261	59.60	21.15
3.50	40.40	1534	89.90	17.06

Table 2. Comparative with the different thicknesses of mass to compensate for the increased thickness of the beam and data of the maximum power generated, volume and power density of each harvester.

With the data obtained in the simulation shown in Table 2, the volume and cost of each harvester are calculated. As seen in Figure 7a, the cost and the volume of the harvester are closely related because most of the volume is mass. Furthermore, it can be seen how the highest power density is obtained for a Tb of 1.5 mm.

Finally, a parametric simulation of the depth of the piezoelectric material from the surface of the harvester has been performed. As can be seen in Figure 7b and as mentioned above in the design section, the closer the material is to the surface, the more power it generates since it is farther from the neutral line of the beam.

With the results obtained from the simulations, it can be concluded that the best specification for the harvester is the design with a dimension of 10.2 mm × 40 mm (Lc x Lm). In addition, to obtain a higher power density, the beam should be 1.5 mm thick and the piezoelectric material should be as close to the surface as possible.

1.7. Characterization

1.7.1. Electrical Characterization

Once the piezoelectric resonant energy harvesters, comprising an energy harvester as a functional structure and PVDF as the piezoelectric material, have been manufactured according to the method for 3D printing of monolithic functional structures according to the present invention, we proceed to the electrical characterization of such 3D-printed devices. Three harvesters were manufactured with the piezoelectric material at 200 μm from the surface, and other three harvesters were manufactured with the piezoelectrical material at 300 μm.

Two different electrical characterizations have been conducted.

The first characterization, shown in Figure 8a, involves a stepper motor that performs movements from 1 mm to 6 mm of distance on the Z-axis. Simultaneously, the voltage generated by the harvester is measured using a Sourcemeter. A force sensor, attached to the stepper motor, records the force data through a dynamometer. An ad-hoc LabVIEW® program controls all the setup comprising these devices. As can be seen in Figure 8b, a displacement of 6 mm along the Z-axis results in an average voltage of 71.7 V for the harvester with the piezoelectric material positioned 300 µm far from the surface. Reducing the distance of the piezoelectric material from 300 µm to 200 µm increases the average voltage to 85.2 V, representing a 19% increment in the maximum voltage generated. According to the force data repre-sented in Figure 8c, the depth of the piezoelectric material does not affect the force needed to achieve 6 mm of travel at the tip of the cantilever.

For the second electrical characterization, as can be shown in Figure 9a, a magnetic mass is attached to adjust the resonance frequency to 50 Hz. An electrodynamic shaker is used to emulate environmental vibrations at different input acceleration levels. This is controlled through an ad-hoc MATLAB® program that allows automatizing, acquiring and processing the voltage measurements. All these data are captured by an acquisition system. Subsequently, fixing a certain acceleration magnitude, a sweep of load resistors values is performed. This allows us to determine the optimal load resistor value for the highest generated power.

Due to the voltage limitations of the acquisition system, which cannot measure voltages exceeding 10 V, the load resistance sweep is initially carried out with a small acceleration of 0.1 G, ensuring that it remains below 10 V. Figure 9b shows that the optimal load resistance for maximum power generation is 4 MΩ, resulting a maximum power of 4.4 µW.

Once the optimal load resistance is known, a voltage divider is used, composed of a set of 500 KΩ and 3.5 MΩ resistors. It is possible to measure the voltages generated by harvesters with accelerations greater than 0.1 G.

The voltage generated by the piezoelectric generator was measured while performing an acceleration sweep ranging from 0.1 G to 1 G, as shown in Figure 9c. For an acceleration of 1 G, the harvester with the piezoelectric material positioned 300 µm from the surface achieved an average voltage of 62.3 V. By reducing the distance of the piezoelectric material to 200 µm, an average voltage of 75.6 V is achieved, resulting in a 21.4% increase in the maximum voltage generated. Using the aforementioned voltage data, the maximum power for the different accelerations was calculated and plotted in Figure 9d. It can be observed that reducing the difference between the two depths of the piezoelectric material resulted in an increase of up to 47.3% in the maximum power generated. This led to a maximum output power of 1.46 mW.

1.7.2. Physical Characterization of the PVDF material

An inspection using a scanning electron microscope (SEM) was performed to validate the thickness of the materials provided by the manufacturer and, as can be seen in Figure 10a, the measured thickness closely matches the manufacturer specifications.

Using a piezometer, we can measure the exact coefficient of our PVDF piece. As shown in Figure 10b, the coefficient is the same as the manufacturer's specifications.

1.7.3. Measurement of Young's modulus of the functional structure material (PLA)

The Young's modulus of the PLA used to 3D print the piezoelectric resonant energy harvesters of the examples is 2.8 ± 0.15 GPa, as stated in the technical datasheet. When introducing a material within the PLA, the overall effective Young's modulus can be changed, depending on the resulting combination of materials. Therefore, the Young's modulus of the harvesters will be calculated based on the force data measured with a stepper motor displacement from the previous section.

displacement of a cantilever beam δ is related to the applied load (P), and the Young modulus (E), according to the next Equation (4):

$$\delta = \frac{1}{3} \frac{PL^3}{EI}, \quad (4)$$

where L is the length of the cantilever, and I the second moment of inertia. The second moment of inertia (I) quantifies the resistance of the transversal section against bending, with respect to that transversal axis.

For a prismatic beam with a rectangular section (depth h and with w) the value of the second moment of inertia of cantilever beam I is given by:

$$I = \frac{wh^3}{12} = \frac{0.04\ m\ x\ 0.0015\ m^3}{12} = 11.25x10^{-12}\ m^4, \quad (5)$$

From Equation (4) and using the force data measured with stepper motor displacement, the Young's modulus of harvesters is calculated:

$$E = \frac{1}{3}\frac{PL^3}{\delta I} = \frac{4.5\ N\ x\ 0.05\ m^3}{3\ x\ 0.006\ m\ x\ 11.25x10^{-12}\ m^4} = 2.78\ GPa, \quad (6)$$

From the Young's modulus obtained from the above Equation (6), it can be seen that the modulus is within the manufacturer's specifications and that the piezoelectric material has little effect on the final Young's modulus of the harvesters.

1.8. Finite Elements Simulation

The energy harvesters were simulated again with COMSOL Multiphysics® to compare the results of the electrical characterization with a theoretical model. Physical parameters such as Young's modulus, thickness, coefficient of the piezoelectric material, and harvester dimensions were included in the simulation to achieve a realistic representation.

A parametric sweep ranging from 48 Hz to 54 Hz was performed to determine the resonance frequency of the resonators with an optimal load resistance of 4 MΩ. In figure 11a a comparative of the simulated electrical characterization of the harvesters (curves plotted from 48 to 54 Hz) with the actual electrical characterization of the harvesters (curves plotted from 45 to 55 Hz), for the maximum open-circuit voltage (Y axis) that can be generated by the piezoelectric generator, for the frequency sweep plotted in the

figure with an acceleration of 0.5 G. The resonance frequency for the simulated harvesters with the software COMSOL Multiphysics® was approximately 50.5 Hz, while the electrical characterization of the manufactured harvesters yielded a resonance frequency of 49.5 Hz. Initially, the harvesters were tuned to resonate at 50 Hz with an acceleration of 0.1 G. However, due to spring softening with increasing acceleration, the resonance frequency is shifted from 0.5 Hz to 49.5 Hz.

As in the electrical characterization with the shaker, a sweep of the load resistance is performed to calculate the maximum power. As shown in the Figure 11b, which graphically represents a comparison of the maximum power generated in relation to the depth of the piezoelectric material (200µm and 300µm) and in relation of the load impedance (MΩ), the maximum power generation is around 5 MΩ, with a maximum power of 283 µW for the harvester with a 300 µm distance of the piezoelectric material and 464 µW for the 200 µm distance. These values are very similar to the maximum powers measured in Figure 9c, with 288 µW and 462 µW, respectively.

1.9. 1.9. Example of Application

As mentioned earlier, the energy harvester can be customized using CAD software (e.g Tinkercard®, https://www.tinkercad.com) to adapt its specifications for various application scenarios. An example application for the monolithic functional structure of the invention, with PVDF as the piezoelectric material, could instead use as the functional structure a sensor (rather than an energy harvester).

In this particular case (using a sensor as the functional structure), the sensor can be employed to measure the current flowing through the wire of a high-voltage tower. When an electric current passes through the wires, it generates a magnetic field that is directly proportional to the current flowing through the wire. Moreover, by using a magnetic mass (for example, two magnetic masses of Neodimium with dimensions 10x10x2.7 mm), the monolithic sensor structure with PVDF as the piezoelectric material, can be made to resonate, and depending on the current it passes, we can measure an instantaneous proportional voltage in our sensor.

In this example of application, the maximum dimensions for the sensor are 30 mm × 20 mm with a height of 10 mm. The resonance frequency for this resonator is the same as the frequency of the current flowing through the wire being measured, which is 50 Hz. The magnets for the magnetic mass have dimensions of 10 mm × 10 mm and a thickness of 2.7 mm. The support will be fixed at dimensions of 20 mm × 10 mm and a height of 10 mm to ensure good anchoring and easy fastening. A simulation is performed to obtain the resonance frequency at 50 Hz. As shown in Figure 12a, measurements of 12 mm × 20 mm and a thickness of 700 µm for the cantilever beam are obtained. Two magnets, for example two magnetic masses of Neodimium with dimensions 10x10x2.7 mm, will be required for the magnetic mass. Figure 12b shows the stress distribution in the beam when the cantilever is resonating at an acceleration of 0.1 G.

As can be shown in Figure 13a and Figure 13b, the simulated sensor is mounted inside a sensor node provided by the startup company "Energiot Devices SL" (www.energiot.com). To test the sensor in the laboratory, two heaters with two power selections have been connected. This setup allows for the generation of four different currents depending on the selected power: 1500 W (6.5 A), 3000 W (13 A), 4500 W (19.5 A) and 6000 W (26 A). As can be seen in Figure 13c, the different current cases passing through the cable can be measured using the corresponding voltage readings, demonstrating a linear response.

Furthermore, the magnetic field can also be used to power wireless sensors that measure various parameters such as magnetic field, ambient and line temperature, acceleration, tilt, humidity and light intensity and transmit the gathered information to the cloud.

Summary of the Example

In this example, a resonant piezoelectric energy harvester by exploiting 3D printing technology and encapsulating PVDF within the structure, resulting in a monolithic harvester, was designed, manufactured, and physically and electrically characterized. With this, an economically viable energy harvester was achieved that mechanically improves the anchoring of the resonator thanks to its structure attached to the fixing

support. The device was optimized through the finite element simulation software COMSOL Multiphysics® 6.0.

Furthermore, an example of the practical application of the resonator by designing and fabricating a specific use case for measuring the current passing through a wire using magnetic fields, was demonstrated. It was shown that 3D printing enabled the manufacturing of a compact monolithic functional structure (i.e. a monolithic harvester, and also facilitated its customization and optimization for specific requirements.

Overall, this example provides a practical approach to designing and manufacturing resonant harvesters using 3D printing. The demonstrated use case application shows the potential to use such devices in a myriad of real-world scenarios.

CLAIMS

1. A monolithic functional structure, characterized in that it comprises:

- at least a functional structure made of a functional structure material; and
- at least a piezoelectric material;
- wherein the functional structure and the piezoelectric material are part of a single piece;
- wherein the functional structure and the piezoelectric material are electrically connected; and
- wherein the piezoelectric material is not located along the neutral axis of the monolithic functional structure.

2. Monolithic functional structure according to claim 1, wherein the functional structure material is selected from PLA, ABS, PVA, PP, Tough PLA, CPE, PET-G, Nylon, PC and any combination thereof.

3. Monolithic functional structure according to claims 1 or 2, wherein the piezoelectric material of the monolithic functional structure is selected from zirconate titanate, Polyvinylidene fluoride or their copolymers, copolymer of Polyvinylidene fluoride and trifluoroethylene (PVDF-TrFE), copolymer of Polyvinylidene fluoride and tetrafluoroethylene (PVDF-TrFE), or combinations thereof.

4. Monolithic functional structure according to any of the previous claims, which additionally comprises at least a substrate on top of which the functional structure and the piezoelectric material are located, wherein the substrate material is selected from glass.

5. Monolithic functional structure according to any of the previous claims, wherein the functional structure of the monolithic functional structure is a low power sensor.

6. Monolithic functional structure according to any of the previous claims, wherein the monolithic functional structure is a monolithic energy harvester structure with PVDF as the piezoelectric material.

7. Monolithic functional structure according to any of the previous claims, wherein the at least one functional structure and the at least one piezoelectric material are at least in partial physical contact with each other.

8. Monolithic functional structure according to any of the previous claims, characterized in that comprises from bottom to top:

- at least a first layer of functional structure material comprising at least one layer of printed structural material, wherein a region of the said layer of functional structure material is left empty as a depression, wherein a metal layer, preferably copper, applied in such region;
- at least a second layer of functional structure material comprising at least one layer of printed structural material on top of the first layer of functional structure material, wherein at least the top of the metal layer is left uncovered;
- a layer of piezoelectric material on top of the first layer of functional structure material, at least partially in contact with the metal layer;
- at least a third layer of functional structure material comprising at least one layer of printed structural material on top of the piezoelectric material layer and on top of the second layer of functional structure material, wherein at least a region on the top of the metal layer and a region on the top of the piezoelectric material layer are left uncovered;
- an electrical connector selected from a metal wire or a metal spring load, located in both of the regions left uncovered on top of the metal layer and on top of the piezoelectric material layer.

9. Method for the 3D printing of monolithic functional structures according to any of the previous claims, characterized in that it comprises the steps of:

a) providing a substrate, preferably a glass substrate;
b) printing at least one layer of a first functional structure material that comprising at least one layer of printed structural material on the substrate of the step (a), preferably PLA, without applying functional structure material to at least a region of the last printing layer;

c) applying metal in such a region of the step (b), preferably copper,
d) optionally, printing at least one layer of a second functional structure material that comprising at least one layer of printed structural material, preferably PLA, without applying functional structure material at least on top of the region where the metal has been applied in step (c);
e) applying a piezoelectric material, preferably Polyvinylidene fluoride, on top of the layer where the metal has been applied in step (c), preferably at least partially in direct contact with the metal;
f) printing at least one layer of a third functional structure material that comprising at least one layer of printed structural material, preferably PLA, without applying functional structure material on top of at least a region of the metal of step (c) and on top of at least a region of the piezoelectric material of step (e), and
g) placing at least an electrical connector in both of the regions left uncovered on top of the metal and on top of the piezoelectric material of step (f).

10. Method according to claim 9, wherein the 3D printing is carried out by Fused Deposition Modelling.

11. Method according to claim 9 or 10, wherein computer-implemented design (CAD) software is used in order to design the monolithic functional structure to be 3D printed.

12. Method according to any of claims 9 to 11, wherein a model created by computer-implemented design (CAD) software is sliced into layers using slicing software.

13. Method according to any of claims 9 to 12, wherein the applied metal in step c) of the method is selected from gold, silver, or copper, preferably copper.

14. Method according to any of claims 9 to 13, wherein the at least one electrical connector placed in both of the regions, in step g) of the method, is selected from a metal wire or a metal spring load.

15. Method according to claim 14, wherein the metal of the metal wire or metal spring load is selected from gold, silver, or copper, preferably copper.

16. Method according to any of claims 9 to 15, wherein the functional structure material is selected from PLA (polylactic acid), ABS (acrylonitrile butadiene styrene), PVA (polyvinyl alcohol), PP (polypropylene), PLA Tough, CPE (co-polyester), PET-G (glycol-modified polyethylene terephthalate), Nylon (polyamide) and PC (polycarbonate); preferably PLA, and even more preferably tough PLA.

17. Use of monolithic functional structure according to any of claims 1 to 5 or 7 to 8, as a sensor, low-power sensor, energy harvester or actuator.

18. Use of the monolithic functional structure according to claim 17 as a low-power sensor for the creation of a large wireless network wherein the low-power sensors communicate with each other.

DRAWINGS

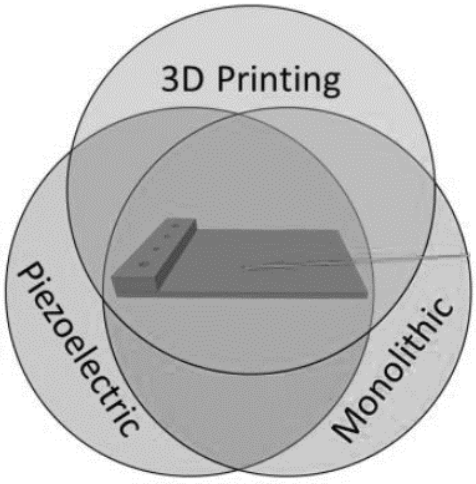


Fig. 1

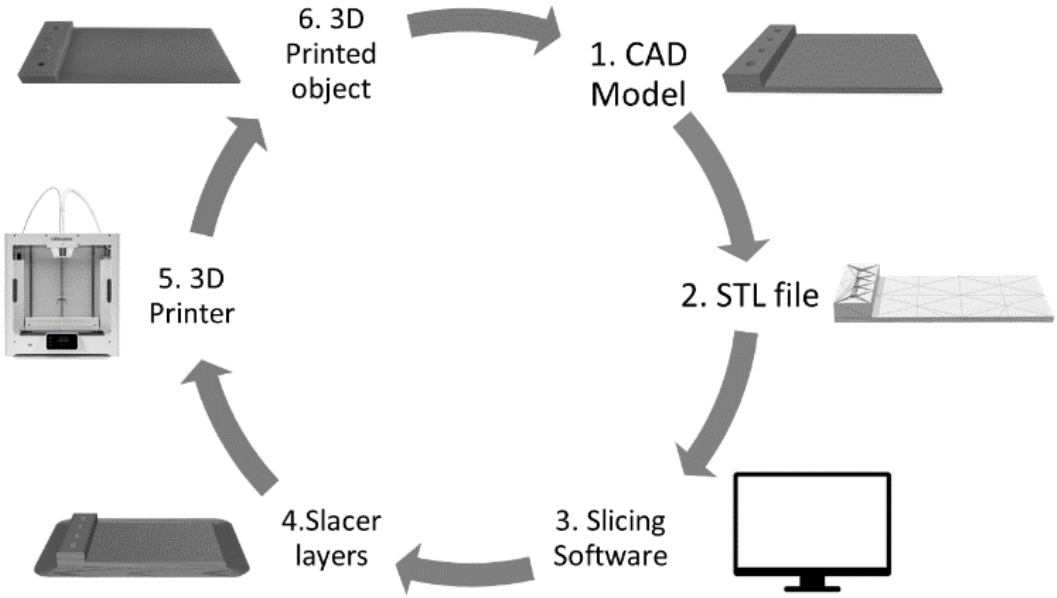


Fig. 2

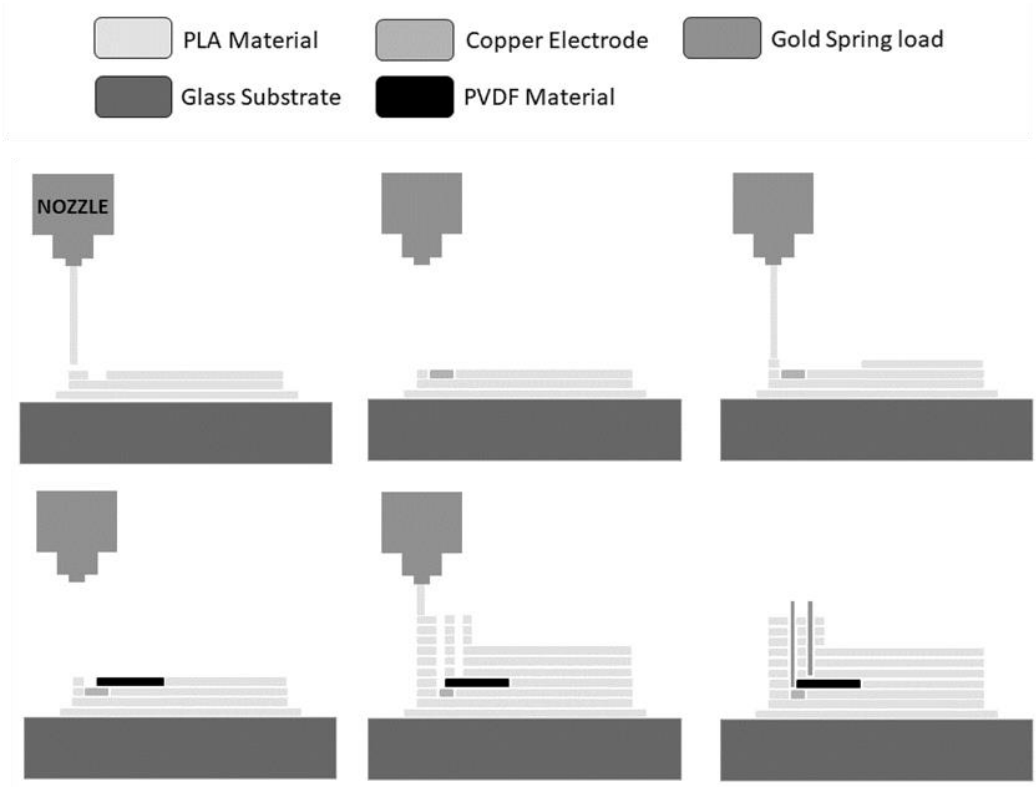

PLA Material
Copper Electrode
Gold Spring load
Glass Substrate
PVDF Material
NOZZLE

Fig. 3

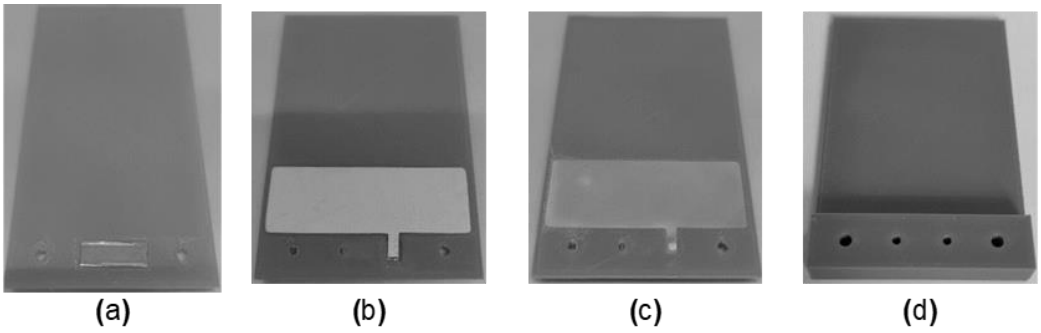

(a)
(b)
(c)
(d)

Fig. 4

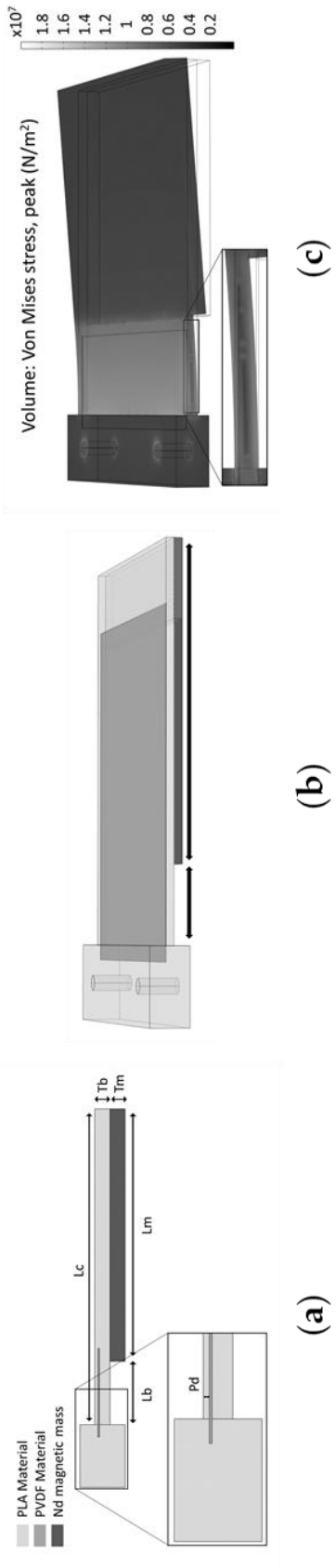

x10^7
1.8
1.6
1.4
1.2
1
0.8
0.6
0.4
0.2
Volume: Von Mises stress, peak (N/m²)
(c)
(b)
Tb
Tm
Lm
Lc
Lb
Pd
PLA Material
PVDF Material
Nd magnetic mass
(a)

Fig. 5

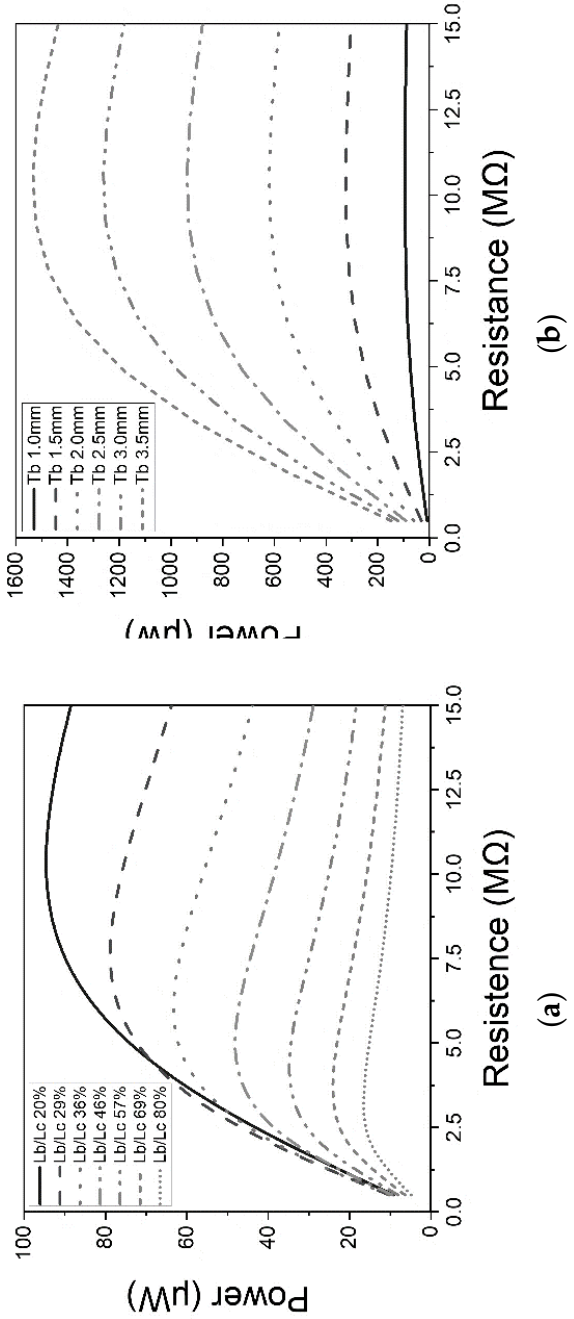

Power (μW)
Resistance (MΩ)
(a)
Lb/Lc 20%
Lb/Lc 29%
Lb/Lc 36%
Lb/Lc 46%
Lb/Lc 57%
Lb/Lc 69%
Lb/Lc 80%
Power (μW)
Resistance (MΩ)
(b)
Tb 1.0mm
Tb 1.5mm
Tb 2.0mm
Tb 2.5mm
Tb 3.0mm
Tb 3.5mm

Fig. 6

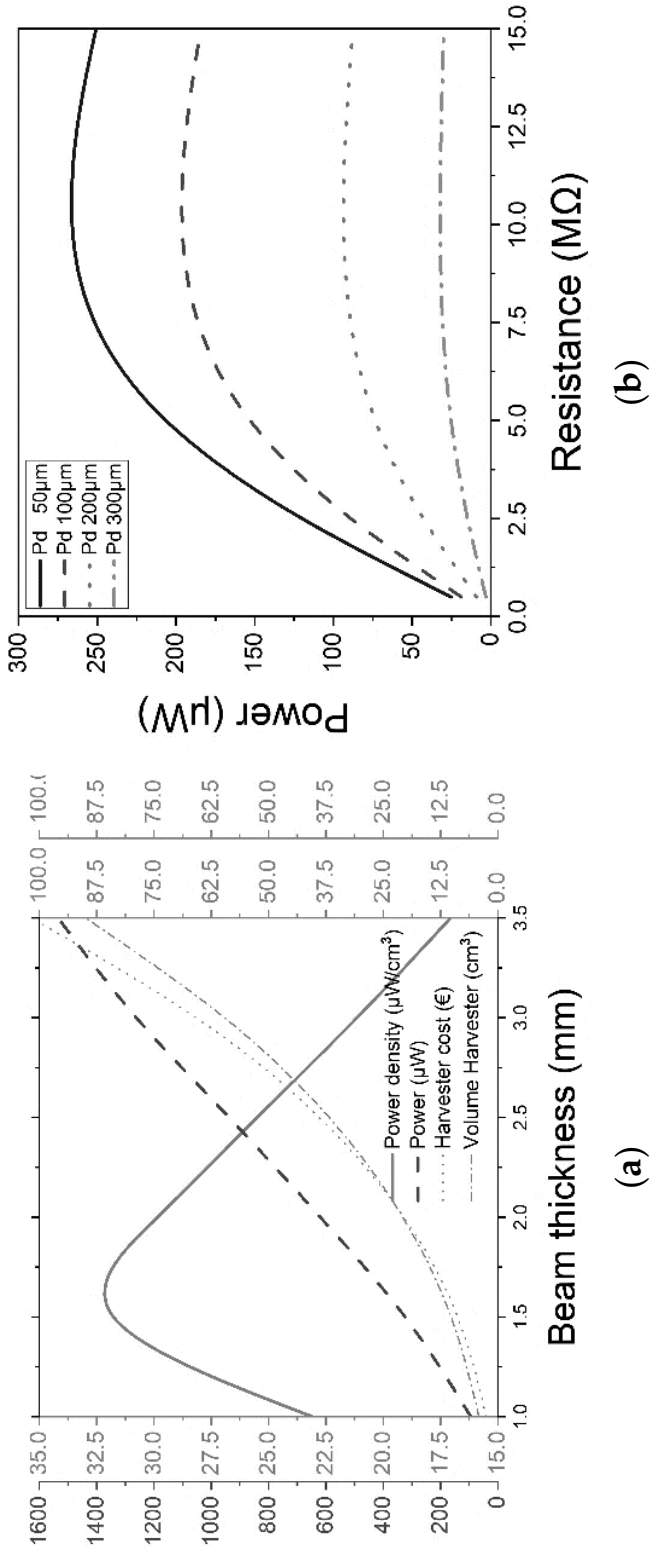
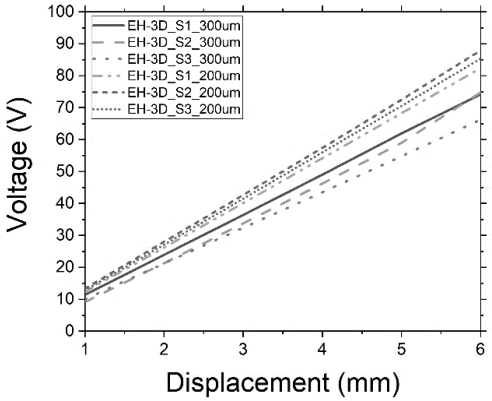

Power (μW)
Resistance (MΩ)
Pd 50μm
Pd 100μm
Pd 200μm
Pd 300μm
(b)
Beam thickness (mm)
Power density (μW/cm³)
Power (μW)
Harvester cost (€)
Volume Harvester (cm³)
(a)

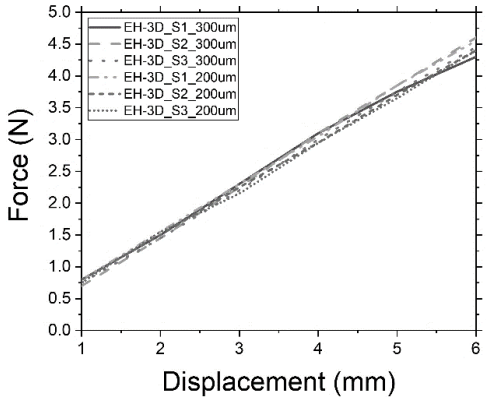
Fig. 7


Aname

(**a**)


EH-3D_S1_300um
EH-3D_S2_300um
EH-3D_S3_300um
EH-3D_S1_200um
EH-3D_S2_200um
EH-3D_S3_200um
Voltage (V)
Displacement (mm)

(**b**)


EH-3D_S1_300um
EH-3D_S2_300um
EH-3D_S3_300um
EH-3D_S1_200um
EH-3D_S2_200um
EH-3D_S3_200um
Force (N)
Displacement (mm)

(**c**)

Fig. 8

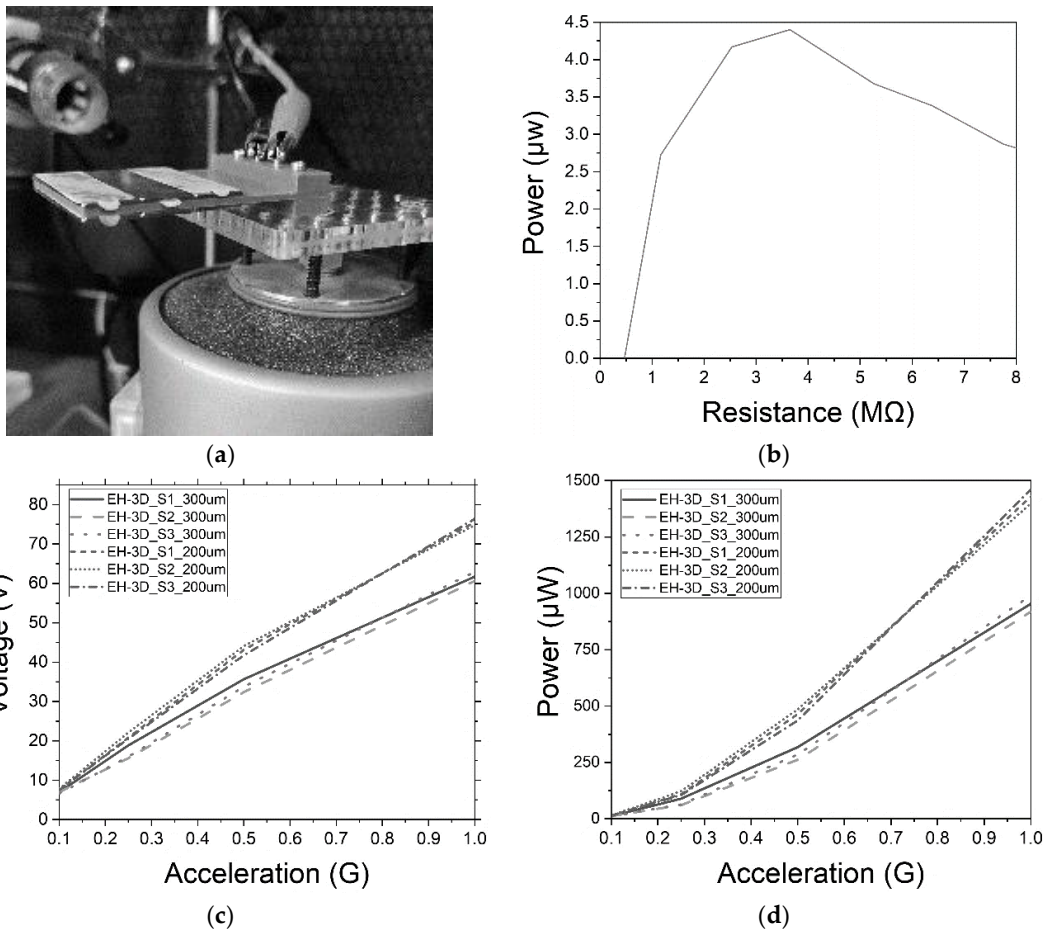

(a)
Power (μw)
Resistance (MΩ)
(b)
Voltage (V)
Acceleration (G)
EH-3D_S1_300um
EH-3D_S2_300um
EH-3D_S3_300um
EH-3D_S1_200um
EH-3D_S2_200um
EH-3D_S3_200um
(c)
Power (μW)
Acceleration (G)
(d)

Fig. 9

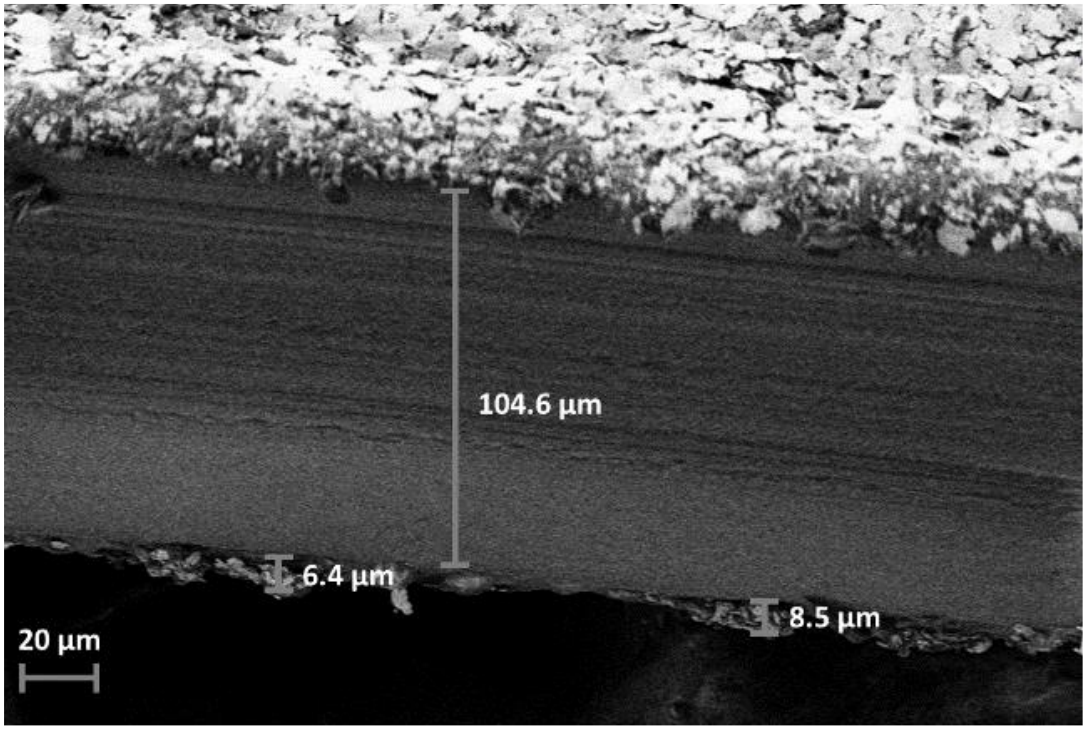


Fig. 10

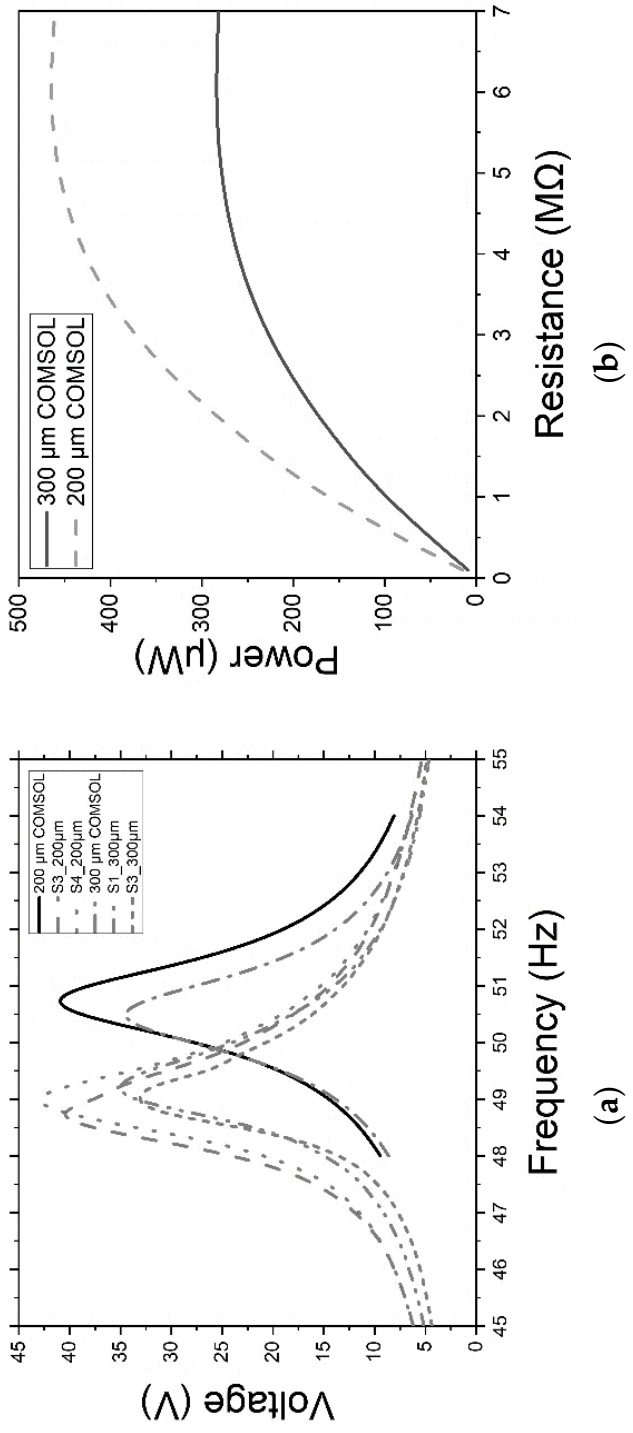

Power (μW)
Resistance (MΩ)
300 μm COMSOL
200 μm COMSOL
(b)
Voltage (V)
Frequency (Hz)
200 μm COMSOL
S3_200μm
S4_200μm
300 μm COMSOL
S1_300μm
S3_300μm
(a)

Fig. 11

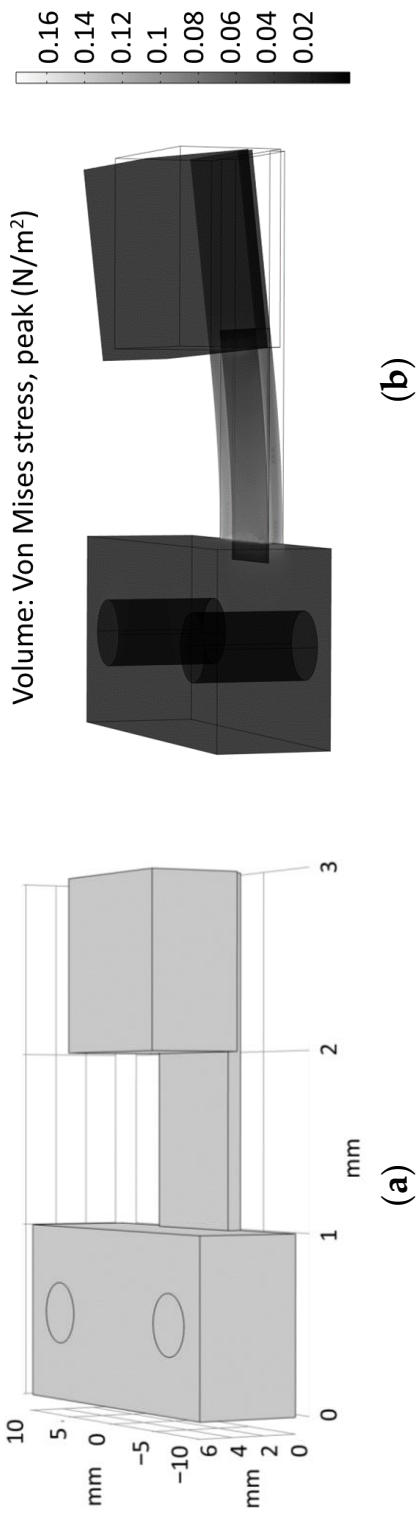
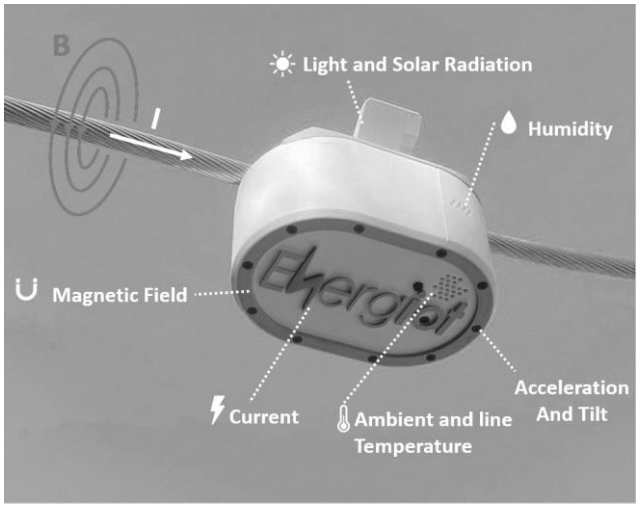

0.16
0.14
0.12
0.1
0.08
0.06
0.04
0.02
Volume: Von Mises stress, peak (N/m²)
(b)
3
2
1
0
mm
(a)
10
5
0
−5
−10
mm
6
4
2
0
mm

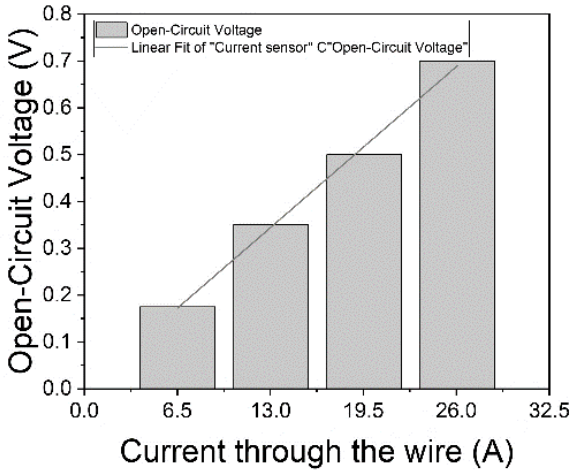
Fig. 12



(a)


B
I
Light and Solar Radiation
Humidity
Magnetic Field
Energisa
Current
Ambient and line Temperature
Acceleration And Tilt

(b)


Open-Circuit Voltage
Linear Fit of "Current sensor" C"Open-Circuit Voltage"
Open-Circuit Voltage (V)
0.0
0.1
0.2
0.3
0.4
0.5
0.6
0.7
0.8
0.0
6.5
13.0
19.5
26.0
32.5
Current through the wire (A)

(c)

Fig. 13

ABSTRACT

Monolithic functional structures and method for their production.

The present invention belongs to the field of electrically-powered functional structures, specifically to monolithic functional structures comprising at least a functional structure (such as a resonator, a sensor, an energy harvester, etc.) and at least a piezoelectric material. Moreover, the at least one functional structure and the at least one piezoelectric material are part of a single piece and are electrically connected between them. The invention refers both to such a monolithic functional structure, and to a method for 3D printing such monolithic functional structure.

7 DISSEMINATION

7.1 List of publications

7.1.1 Directly related to this thesis

1. Duque, M.; Murillo, G. Tapping-Actuated Triboelectric Nanogenerator with Surface Charge Density Optimization for Human Motion Energy Harvesting. *Nanomaterials* **2022**, *12*, 3271. https://doi.org/10.3390/nano12193271

2. Duque, M.; Murillo, G. Low-Cost Manufacturing of Monolithic Resonant Piezoelectric Devices for Energy Harvesting Using 3D Printing. *Nanomaterials* **2023**, *13*, 2334. https://doi.org/10.3390/nano13162334

3. Duque, M.; Murillo, G. Piezoelectric MEMS resonator with magnetic tip mass for energy harvesting from ultra-low intensity magnetic fields. Nano Energy. (*In press*)

4. Duque, M.; Moya, A.; Gomez, M.; Murillo, G.; Integration of ZnO nanostructures in MEMS devices using inkjet printing for energy harvesting. (*Submitte*d).

7.1.2 Additional scientific articles published during the thesis period

1. Marcos Duque, E. Leon-Salguero, J. Sacristán, J. Esteve, G. Murillo. "Optimization of a piezoelectric energy harvester and design of a charge pump converter for CMOS-MEMS monolithic integration," Sensors 19 (8), 1895.

2. Marta Gil, Paris Vélez, Francisco Aznar-Ballesta, Arán Mesegar-Ruiz, Jonatan Muñoz-Enano, Marcos Duque, Ferran Martín. "Electro-inductive Wave Transmission Line based Microfluidic Microwave Sensor," 2020 IEEE MTT-S International Microwave Biomedical Conference (IMBioC), Toulouse, France, 2020, pp. 1-4, doi: 10.1109/IMBIoC47321.2020.9384903.

3. Yiran Zhao, Julie Descamps, Nour al Hoda Al Bast, Marcos Duque, Jaume Esteve, Borja Sepulveda, Gabriel Loget, Neso Sojic. "All-Optical Electrochemiluminescence." Journal of the American Chemical Society 2023 145 (31), 17420-17426. DOI: 10.1021/jacs.3c05856.

4. Yiran Zhao, Julie Descamps, Nour al Hoda Al Bast, Marcos Duque, Jaume Esteve, Borja Sepulveda, Gabriel Loget, Neso Sojic. "Near-IR Photoinduced Electrochemiluminescence Imaging with Structured Silicon Photoanodes." ACS Applied Materials & Interfaces 2024 16 (9), 11722-11729. DOI: 10.1021/acsami.3c19029.

5. Albert Serrà, Elvira Gómez, Nour al Hoda al Bast, Yue Zhang, Marcos Duque, María José Esplandiu, Jaume Esteve, Josep Nogués, Borja Sepúlveda. "Wireless pulsed nanophotoelectrochemical cell for the ultrafast degradation of organic pollutants." Chemical Engineering Journal 2024 Volume 487, 150663, ISSN 1385-8947, https://doi.org/10.1016/j.cej.2024.150663.

7.1.3 Courses and conferences

1. M. Duque, M. Acosta, J. Esteve, G. Murillo. Energy Harvesting Solutions for the implementation of the Internet of Things. The 5th Scientific Meeting of PhD Students at UAB Campus (JPhD2020), Poster presentation, September 17-18, 2020, online.

2. M. Duque, Edgardo Leon, G. Murillo. Multifrequency piezoelectric energy harvesting using a double-mass MEMS cantilever. MNE2021, Poster presentation, September 20-23, 2021 online.

3. M.Duque. Development of novel materials and low-cost devices for mechanical energy harvesting. Young Researcher Day" organized by IMB-CNM, oral presentation, April 20, 2023, Bellaterra.

7.1.4 Patent applications

1. Monolithic functional structures and method for their production.

7.1.5 Supervised projects

1. Bachelor's Thesis: "Smart grid energy harvesting device: Design, fabrication, and characterization" presented by Mario Acosta and supervised by Gonzalo Murillo, Marcos Duque, and Pablo Ortega at the Escola Tècnica d'Enginyeria de Telecomunicació de Barcelona (Universitat Politècnica de Catalunya). July 1st, 2019.

2. Bachelor's Thesis: "Rapid prototyping of piezoelectric micro and nanogenerators based on inkjet printing" presented by Marc Gómez and supervised by Ana Moya, Gonzalo Murillo, and Marcos Duque at the Universitat Autònoma de Barcelona. July 2nd, 2019.

.

8 REFERENCES

[1] G. S. Mishra, A. K. Upadhyay, P. Kaushik, *Green internet of things: Overview* (2020)

[2] Gunneswara VSSS Kalaga Rao, *Design of Internet of Things* (CRC Press, Boca Raton, 2022)

[3] Cisco, Internet of things: How the Next Evolution of the Internet Is Changing Eveything, *Smart Power Distrib. Syst. Control. Commun. Optim.* , 11 (2011)

[4] L. S. Vailshery, Number of Internet of Things (IoT) connected devices worldwide from 2019 to 2030, by vertical (2023) (available at https://www.statista.com/statistics/1194682/iot-connected-devices-vertically/)

[5] Z. Anshul Verma, Pradeepika Verma, Yousef Farhaoui, *Emerging Real-World Applications of Internet of Things* (CRC Press, 2022)

[6] B. Paliwoda, W. Krzysztof, M. Biega, Internet of Things in Industry: Research Profiling, Application, Challenges and Opportunities—A Review, *Energies* **15** (2022)

[7] T. Zheng, M. Ardolino, A. Bacchetti, M. Perona, The applications of Industry 4.0 technologies in manufacturing context: a systematic literature review, *Int. J. Prod. Res.* **59**, 1922–1954 (2021)

[8] J. Qi *et al.*, Advanced internet of things for personalised healthcare systems: A survey, *Pervasive Mob. Comput.* **41**, 132–149 (2017)

[9] Y. YIN, Y. Zeng, X. Chen, Y. Fan, The internet of things in healthcare: An overview, *J. Ind. Inf. Integr.* **1**, 3–13 (2016)

[10] M. A. Omran, B. J. Hamza, W. K. Saad, The design and fulfillment of a Smart Home (SH) material powered by the IoT using the Blynk app, *Mater. Today Proc.* **60**, 1199–1212 (2022)

[11] C. Stolojescu-Crisan, C. Crisan, B. P. Butunoi, An iot-based smart home automation system, *Sensors* **21**, 1–23 (2021)

[12] W. A. Jabbar *et al.*, Design and Fabrication of Smart Home with Internet of Things Enabled Automation System, *IEEE Access* **XX**, 1–9 (2017)

[13] M. U. Sohag, A. K. Podder, Smart garbage management system for a sustainable

urban life: An IoT based application, *Internet of Things (Netherlands)* **11** (2020), doi:10.1016/j.iot.2020.100255

[14] K. Shafique, B. A. Khawaja, F. Sabir, S. Qazi, M. Mustaqim, Internet of things (IoT) for next-generation smart systems: A review of current challenges, future trends and prospects for emerging 5G-IoT Scenarios, *IEEE Access* **8**, 23022–23040 (2020)

[15] J. S. Park, J. H. Park, Future trends of iot, 5G mobile networks, and AI: Challenges, opportunities, and solutions, *J. Inf. Process. Syst.* **16**, 743–749 (2020)

[16] A. Karale, The Challenges of IoT Addressing Security, Ethics, Privacy, and Laws, *Internet of Things (Netherlands)* **15**, 100420 (2021)

[17] K. Sha, T. A. Yang, W. Wei, S. Davari, A survey of edge computing-based designs for IoT security, *Digit. Commun. Networks* **6**, 195–202 (2020)

[18] S. Hamdan, M. Ayyash, S. Almajali, Edge-Computing Architectures for Internet of Things Applications: A Survey, *Sensors 2020, Vol. 20, Page 6441* **20**, 6441 (2020)

[19] E. B. Hansen, S. Bøgh, Artificial intelligence and internet of things in small and medium-sized enterprises: A survey, *J. Manuf. Syst.* **58**, 362–372 (2021)

[20] C. DeFeo, *Energy Harvesting and the Internet of Things* (Elsevier Inc., 2015; http://dx.doi.org/10.1016/B978-0-12-801379-3.00009-7)

[21] C. W. Yau, T. T. O. Kwok, C. U. Lei, Y. K. Kwok, *Energy harvesting in internet of things* (2018)

[22] L. Probst, Pedersen, Bertrand, L. Dakkak-Arnoux, Energy harvesting to power the rise of the Internet of Things, *Digit. Transform. Monit.* , 1–8 (2017)

[23] T. Sanislav, G. D. Mois, S. Zeadally, S. C. Folea, Energy Harvesting Techniques for Internet of Things (IoT), *IEEE Access* **9**, 39530–39549 (2021)

[24] H. Liang, G. Hao, O. Z. Olszewski, A review on vibration-based piezoelectric energy harvesting from the aspect of compliant mechanisms, *Sensors Actuators, A Phys.* **331**, 112743 (2021)

[25] Kenji Uchino, *Advanced Piezoelectric Materials Science and Technology* (2017)

[26] T. Li, P. S. Lee, Piezoelectric Energy Harvesting Technology: From Materials, Structures, to Applications, *Small Struct.* **3** (2022), doi:10.1002/sstr.202100128

[27] D. R. Swetapadma Praharaj, *Piezoelectric Technology: Materials and Applications for Green Energy Harvesting* (CRC Press, 2023)

[28] pp. 0_. vol., no., IEEE Standard on Piezoelectricity (ANSI/IEEE Std 176-1987) (1988), doi:10.1109/IEEESTD.1988.79638

[29] C. H. Nguyen, U. Hanke, E. Halvorsen, Actuation of Piezoelectric Layered Beams with d31 and d33 Coupling, *IEEE Trans. Ultrason. Ferroelectr. Freq. Control* **65**, 815–827 (2018)

[30] Y. K. Zhu *et al.*, Modeling and characterization of multilayered d 15 mode piezoelectric energy harvesters in series and parallel connections, *Smart Mater. Struct.* **25** (2016), doi:10.1088/0964-1726/25/7/075027

[31] C. Covaci, A. Gontean, Piezoelectric energy harvesting solutions: A review, *Sensors (Switzerland)* **20**, 1–37 (2020)

[32] N. Sezer, M. Koç, A comprehensive review on the state-of-the-art of piezoelectric energy harvesting, *Nano Energy* **80**, 105567 (2021)

[33] P. T. Vol, P. O. Box, Electrostatic Discharge (ESD) -Facts Faults-A Review, **8**, 231–247 (1995)

[34] S. Edition, *ESD in Silicon ESD in Silicon Second Edition* (2002)

[35] Z. Su *et al.*, Asymmetrical Triboelectric Nanogenerator with Controllable Direct Electrostatic Discharge, *Adv. Funct. Mater.* **26**, 5524–5533 (2016)

[36] C. Lee *et al.*, Electrostatic discharge prevention system via body potential control based on a triboelectric nanogenerator, *Nano Energy* **103**, 107834 (2022)

[37] Y. S. Zhou *et al.*, In situ quantitative study of nanoscale triboelectrification and patterning, *Nano Lett.* **13**, 2771–2776 (2013)

[38] M. Mirkowska, M. Kratzer, C. Teichert, H. Flachberger, Atomic force microscopy as a tool to explore triboelectrostatic phenomena in mineral processing, *Chemie-*

Ingenieur-Technik **86**, 857–864 (2014)

[39] T. Bu *et al.*, Nanoscale triboelectrification gated transistor, *Nat. Commun.* **11**, 1–8 (2020)

[40] H. Zou *et al.*, Quantifying the triboelectric series, *Nat. Commun.* **10**, 1–9 (2019)

[41] F. R. Fan, Z. Q. Tian, Z. Lin Wang, Flexible triboelectric generator, *Nano Energy* **1**, 328–334 (2012)

[42] Z. L. Wang, Triboelectric nanogenerators as new energy technology and self-powered sensors - Principles, problems and perspectives, *Faraday Discuss.* **176**, 447–458 (2014)

[43] S. Chandrasekaran, A. Jayakumar, R. Velu, A Comprehensive Review on Printed Electronics: A Technology Drift towards a Sustainable Future, *Nanomaterials* **12** (2022), doi:10.3390/nano12234251

[44] N. Zavanelli, W. H. Yeo, Advances in Screen Printing of Conductive Nanomaterials for Stretchable Electronics, *ACS Omega* **6**, 9344–9351 (2021)

[45] J. Chang, X. Zhang, T. Ge, J. Zhou, Fully printed electronics on flexible substrates: High gain amplifiers and DAC, *Org. Electron.* **15**, 701–710 (2014)

[46] A. Sridhar, T. Blaudeck, R. R. Baumann, Inkjet printing as a key enabling technology for printed electronics., *Mater. Matters (Milwaukee, WI, United States)* **6**, 12–17 (2011)

[47] P. Calvert, Inkjet printing for materials and devices, *Chem. Mater.* **13**, 3299–3305 (2001)

[48] N. Komuro, S. Takaki, K. Suzuki, D. Citterio, Inkjet printed (bio)chemical sensing devices, *Anal. Bioanal. Chem.* **405**, 5785–5805 (2013)

[49] A. Moya *et al.*, Online oxygen monitoring using integrated inkjet-printed sensors in a liver-on-a-chip system, *Lab Chip* **18**, 2023–2035 (2018)

[50] A. Moya *et al.*, Inkjet-printed dissolved oxygen and pH sensors on flexible plastic substrates, *Smart Sensors, Actuators, MEMS VIII* **10246**, 102460F (2017)

[51] Z. P. Yin, Y. A. Huang, N. Bin Bu, X. M. Wang, Y. L. Xiong, Inkjet printing for flexible electronics: Materials, processes and equipments, *Chinese Sci. Bull.* **55**, 3383–3407 (2010)

[52] F. Chollet, H. Liu, *A (not so) short introduction to MEMS* (2011)

[53] N. Maluf, *An Introduction to Microelectromechanical* (2004)

[54] M. K. Mishra, V. Dubey, P. M. Mishra, I. Khan, MEMS Technology: A Review, *J. Eng. Res. Reports* **4**, 1–24 (2019)

[55] Sandia National Laboratories (available at https://www.sandia.gov/mesa/mems-video-image-gallery/)

[56] J. W. Judy, Microelectromechanical systems (MEMS): Fabrication, design and applications, *Smart Mater. Struct.* **10**, 1115–1134 (2001)

[57] L. Wei *et al.*, The Recent Progress of MEMS / NEMS Resonators, (2021)

[58] J. J. Yao, RF MEMS from a device perspective, *J. Micromechanics Microengineering* **10** (2000), doi:10.1088/0960-1317/10/4/201

[59] H. Campanella *et al.*, Monolithic Multiband MEMS RF Front-End Module for 5G Mobile, *J. Microelectromechanical Syst.* **30**, 72–80 (2021)

[60] L. Blocher *et al.*, Purely Inertial Navigation with a Low-Cost MEMS Sensor Array, *Inert. 2021 - 8th IEEE Int. Symp. Inert. Sensors Syst. Proc.* , 44–47 (2021)

[61] N. El-Sheimy, A. Youssef, Inertial sensors technologies for navigation applications: state of the art and future trends, *Satell. Navig.* **1**, 1–21 (2020)

[62] M. Barzegar, S. Blanks, B. A. Sainsbury, W. Timms, MEMS technology and applications in geotechnical monitoring: A review, *Meas. Sci. Technol.* **33** (2022), doi:10.1088/1361-6501/ac4f00

[63] A. Biswas, S. S. Roy, A review on multi nozzle electrohydrodynamic inkjet printing system for MEMS applications, *IOP Conf. Ser. Mater. Sci. Eng.* **1136**, 012015 (2021)

[64] T. Mashimo, S. Izuhara, Review: Recent Advances in Micromotors, *IEEE Access* **8**,

213489–213501 (2020)

[65] J. Ramakrishnan, P. T. R. Gaurav, N. S. Chandar, N. M. Sudharsan, Structural design, analysis and DOE of MEMS-based capacitive accelerometer for automotive airbag application, *Microsyst. Technol.* **27**, 763–777 (2021)

[66] F. A. Mohd Ghazali *et al.*, MEMS actuators for biomedical applications: A review, *J. Micromechanics Microengineering* **30** (2020), doi:10.1088/1361-6439/ab8832

[67] N. Vercier, B. Chaumet, B. Leverrier, S. Bouyat, A new Silicon axisymmetric Gyroscope for Aerospace Applications, *2020 DGON Inert. Sensors Syst. ISS 2020 - Proc.* , 1–18 (2020)

[68] Q. Cai, S. Zhu, The nexus between vibration-based energy harvesting and structural vibration control: A comprehensive review, *Renew. Sustain. Energy Rev.* **155**, 111920 (2022)

[69] A. Hosseinkhani, D. Younesian, P. Eghbali, A. Moayedizadeh, A. Fassih, Sound and vibration energy harvesting for railway applications: A review on linear and nonlinear techniques, *Energy Reports* **7**, 852–874 (2021)

[70] T. A. Saleh, Nanomaterials: Classification, properties, and environmental toxicities, *Environ. Technol. Innov.* **20**, 101067 (2020)

[71] E. Pomerantseva, F. Bonaccorso, X. Feng, Y. Cui, Y. Gogotsi, Energy storage: The future enabled by nanomaterials, *Science (80-.).* **366** (2019), doi:10.1126/science.aan8285

[72] N. Han, X. Li, Study of Static and Dynamic Performances of Miniature Savonius-type Wind Energy Harvesters, *Energy Procedia* **105**, 119–124 (2017)

[73] M. Xie, M. Zhu, Z. Yang, S. Okada, S. Kawamura, Flexible self-powered multifunctional sensor for stiffness-tunable soft robotic gripper by multimaterial 3D printing, *Nano Energy* **79** (2021), doi:10.1016/j.nanoen.2020.105438

[74] L. P. Muthe, K. Pickering, C. Gauss, Nano Select - 2021 - Ben Dali - Ferroelectret energy harvesting with 3D-printed air-spaced cantilever design.pdf, *Compos. Part*

C Open Access **8**, 100271 (2022)

[75] X. Zhou *et al.*, All 3D-printed stretchable piezoelectric nanogenerator with non-protruding kirigami structure, *Nano Energy* **72** (2020), doi:10.1016/j.nanoen.2020.104676

[76] X. Yuan *et al.*, A 3D-printed, alternatively tilt-polarized PVDF-TrFE polymer with enhanced piezoelectric effect for self-powered sensor application, *Nano Energy* **85** (2021), doi:10.1016/j.nanoen.2021.105985

[77] Z. Wang *et al.*, 3D-printed flexible, Ag-coated PNN-PZT ceramic-polymer grid-composite for electromechanical energy conversion, *Nano Energy* **73**, 104737 (2020)

[78] H. Feng *et al.*, Multimodal MEMS vibration energy harvester with cascaded flexible and silicon beams for ultralow frequency response, *Microsystems Nanoeng.* **9** (2023), doi:10.1038/s41378-023-00500-8

[79] H. C. Song *et al.*, Ultra-low resonant piezoelectric MEMS energy harvester with high power density, *J. Microelectromechanical Syst.* **26**, 1226–1234 (2017)

[80] G. Tang *et al.*, A piezoelectric micro generator worked at low frequency and high acceleration based on PZT and phosphor bronze bonding, *Sci. Rep.* **6**, 2–11 (2016)

[81] S. C. Lin, W. J. Wu, Fabrication of PZT MEMS energy harvester based on silicon and stainless-steel substrates utilizing an aerosol deposition method, *J. Micromechanics Microengineering* **23** (2013), doi:10.1088/0960-1317/23/12/125028

[82] H. Liu, C. Lee, T. Kobayashi, C. J. Tay, C. Quan, A new S-shaped MEMS PZT cantilever for energy harvesting from low frequency vibrations below 30 Hz, *Microsyst. Technol.* **18**, 497–506 (2012)

[83] H. Liu, C. J. Tay, C. Quan, T. Kobayashi, C. Lee, Piezoelectric MEMS energy harvester for low-frequency vibrations with wideband operation range and steadily increased output power, *J. Microelectromechanical Syst.* **20**, 1131–1142 (2011)

[84] J. C. Park, D. H. Bang, J. Y. Park, Micro-fabricated electromagnetic power generator to scavenge low ambient vibration, *IEEE Trans. Magn.* **46**, 1937–1942 (2010)

[85] P. Wang *et al.*, A micro electromagnetic low level vibration energy harvester based on MEMS technology, *Microsyst. Technol.* **15**, 941–951 (2009)

[86] J. C. Park, J. Y. Park, Y. P. Lee, Modeling and characterization of piezoelectric d33-Mode MEMS energy harvester, *J. Microelectromechanical Syst.* **19**, 1215–1222 (2010)

[87] S. Hasan, A. Z. Kouzani, S. Adams, J. Long, M. A. P. Mahmud, Comparative study on the contact-separation mode triboelectric nanogenerator, *J. Electrostat.* **116**, 103685 (2022)

[88] Theory of Sliding-Mode Triboelectric Nanogenerators.pdf

[89] S. Wang *et al.*, Sliding-triboelectric nanogenerators based on in-plane charge-separation mechanism, *Nano Lett.* **13**, 2226–2233 (2013)

[90] W. Akram, Q. Chen, G. Xia, J. Fang, A review of single electrode triboelectric nanogenerators, *Nano Energy* **106**, 108043 (2023)

[91] S. Niu *et al.*, Theory of freestanding triboelectric-layer-based nanogenerators, *Nano Energy* **12**, 760–774 (2015)

[92] Z. Zhao *et al.*, Selection rules of triboelectric materials for direct-current triboelectric nanogenerator, *Nat. Commun.* **12**, 1–8 (2021)

[93] M. Seol *et al.*, Triboelectric Series of 2D Layered Materials, *Adv. Mater.* **30**, 1–8 (2018)

[94] Z. L. Wang *et al.*, *Triboelectric Nanogenerators* (2018; https://doi.org/10.1016/j.nanoen.2020.105280)

[95] S. Wang, L. Lin, Z. L. Wang, Nanoscale triboelectric-effect-enabled energy conversion for sustainably powering portable electronics, *Nano Lett.* **12**, 6339–6346 (2012)

[96] W. Tang *et al.*, Implantable Self-Powered Low-Level Laser Cure System for Mouse

Embryonic Osteoblasts' Proliferation and Differentiation, *ACS Nano* **9**, 7867–7873 (2015)

[97] F. R. Fan *et al.*, Transparent triboelectric nanogenerators and self-powered pressure sensors based on micropatterned plastic films, *Nano Lett.* **12**, 3109–3114 (2012)

[98] X. S. Zhang *et al.*, Frequency-multiplication high-output triboelectric nanogenerator for sustainably powering biomedical microsystems, *Nano Lett.* **13**, 1168–1172 (2013)

[99] Z. H. Lin *et al.*, Nanopatterned Textile-Based Wearable Triboelectric Nanogenerator, *ACS Nano* **7**, 4554–4560 (2013)

[100] Y. S. Choi, Q. Jing, A. Datta, C. Boughey, S. Kar-Narayan, A triboelectric generator based on self-poled Nylon-11 nanowires fabricated by gas-flow assisted template wetting, *Energy Environ. Sci.* **10**, 2180–2189 (2017)

[101] W. Seung *et al.*, Nanopatterned Textile-Based Wearable Triboelectric Nanogenerator, , 3501–3509 (2015)

[102] G. Zhu *et al.*, Toward large-scale energy harvesting by a nanoparticle-enhanced triboelectric nanogenerator, *Nano Lett.* **13**, 847–853 (2013)

[103] J. Chun *et al.*, Mesoporous pores impregnated with Au nanoparticles as effective dielectrics for enhancing triboelectric nanogenerator performance in harsh environments, *Energy Environ. Sci.* **8**, 3006–3012 (2015)

[104] Y. Zheng *et al.*, An electrospun nanowire-based triboelectric nanogenerator and its application in a fully self-powered UV detector, *Nanoscale* **6**, 7842–7846 (2014)

[105] C. Li *et al.*, Self-Powered Electrospinning System Driven by a Triboelectric Nanogenerator, *ACS Nano* **11**, 10439–10445 (2017)

[106] Y. Li *et al.*, Advances in electrospun nanofibers for triboelectric nanogenerators, *Nano Energy* **104** (2022), doi:10.1016/j.nanoen.2022.107884

[107] C. K. Jeong *et al.*, Topographically-designed triboelectric nanogenerator via block

copolymer self-assembly, *Nano Lett.* **14**, 7031–7038 (2014)

[108] D. Kim *et al.*, High-performance nanopattern triboelectric generator by block copolymer lithography, *Nano Energy* **12**, 331–338 (2015)

[109] H. G. Yoo, M. Byun, C. K. Jeong, K. J. Lee, Performance Enhancement of Electronic and Energy Devices via Block Copolymer Self-Assembly, *Adv. Mater.* **27**, 3982–3998 (2015)

[110] H. Phan, P. N. Hoa, H. A. Tam, P. D. Thang, Q-switched pulsed laser direct writing of aluminum surface micro/nanostructure for triboelectric performance enhancement, *J. Sci. Adv. Mater. Devices* **6**, 84–91 (2021)

[111] J. Huang *et al.*, Micro/nano-structures-enhanced triboelectric nanogenerators by femtosecond laser direct writing, *Nano Energy* **62**, 638–644 (2019)

[112] D. Kim *et al.*, Direct-laser-patterned friction layer for the output enhancement of a triboelectric nanogenerator, *Nano Energy* **35**, 379–386 (2017)

[113] G. Zhu *et al.*, Triboelectric-generator-driven pulse electrodeposition for micropatterning, *Nano Lett.* **12**, 4960–4965 (2012)

[114] X. Sun *et al.*, Controlling the triboelectric properties and tribological behavior of polyimide materials via plasma treatment, *Nano Energy* **102**, 107691 (2022)

[115] W. Shang *et al.*, A Sliding-Mode Triboelectric Nanogenerator with Chemical Group Grated Structure by Shadow Mask Reactive Ion Etching, *ACS Nano* **11**, 8796–8803 (2017)

[116] Z. Wang, Self-Powered High-Resolution and Pressure-Sensitive Triboelectric Sensor Matrix for, *Adv. Mater.* (2016)

[117] P. Bai *et al.*, Integrated multilayered triboelectric nanogenerator for harvesting biomechanical energy from human motions, *ACS Nano* **7**, 3713–3719 (2013)

[118] V. Nguyen, R. Yang, Effect of humidity and pressure on the triboelectric nanogenerator, *Nano Energy* **2**, 604–608 (2013)

[119] H. Chen *et al.*, Crumpled Graphene Triboelectric Nanogenerators: Smaller Devices

with Higher Output Performance, *Adv. Mater. Technol.* **2**, 1–7 (2017)

[120] Advanced Science - 2023 - Son - Recycled Contaminated Crumpled Aluminum Foil-Driven Triboelectric Nanogenerator.pdf

[121] S. H. Shin *et al.*, Triboelectric charging sequence induced by surface functionalization as a method to fabricate high performance triboelectric generators, *ACS Nano* **9**, 4621–4627 (2015)

[122] S. H. Shin *et al.*, Formation of Triboelectric Series via Atomic-Level Surface Functionalization for Triboelectric Energy Harvesting, *ACS Nano* **11**, 6131–6138 (2017)

[123] G. Song *et al.*, Molecularly Engineered Surface Triboelectric Nanogenerator by Self-Assembled Monolayers (METS), *Chem. Mater.* **27**, 4749–4755 (2015)

[124] R. Zhang *et al.*, A review of the advances in composites/nanocomposites for triboelectric nanogenerators, *Nanotechnology* **33** (2022), doi:10.1088/1361-6528/ac4b7b

[125] Z. Zheng, J. Xia, B. Wang, Y. Guo, Hierarchically designed nanocomposites for triboelectric nanogenerator toward biomechanical energy harvester and smart home system, *Nano Energy* **95**, 107047 (2022)

[126] M. Salauddin *et al.*, Laser-carbonized MXene/ZiF-67 nanocomposite as an intermediate layer for boosting the output performance of fabric-based triboelectric nanogenerator, *Nano Energy* **100**, 107462 (2022)

[127] S. Wang *et al.*, Maximum surface charge density for triboelectric nanogenerators achieved by ionized-air injection: Methodology and theoretical understanding, *Adv. Mater.* **26**, 6720–6728 (2014)

[128] J. J. Shao *et al.*, A multi-dielectric-layered triboelectric nanogenerator as energized by corona discharge, *Nanoscale* **9**, 9668–9675 (2017)

[129] T. Zhou *et al.*, Multilayered electret films based triboelectric nanogenerator, *Nano Res.* **9**, 1442–1451 (2016)

[130] G. Zhu, P. Bai, J. Chen, Z. Lin Wang, Power-generating shoe insole based on triboelectric nanogenerators for self-powered consumer electronics, *Nano Energy* **2**, 688–692 (2013)

[131] T. C. Hou *et al.*, Triboelectric nanogenerator built inside shoe insole for harvesting walking energy, *Nano Energy* **2**, 856–862 (2013)

[132] R. Zhang *et al.*, Interaction of the human body with triboelectric nanogenerators, *Nano Energy* **57**, 279–292 (2019)

[133] R. Zhang *et al.*, Human Body Constituted Triboelectric Nanogenerators as Energy Harvesters, Code Transmitters, and Motion Sensors, *ACS Appl. Energy Mater.* **1**, 2955–2960 (2018)

[134] W. Yang *et al.*, 3D stack integrated triboelectric nanogenerator for harvesting vibration energy, *Adv. Funct. Mater.* **24**, 4090–4096 (2014)

[135] J. Yang *et al.*, Broadband vibrational energy harvesting based on a triboelectric nanogenerator, *Adv. Energy Mater.* **4**, 1–9 (2014)

[136] D. Bhatia *et al.*, Continuous scavenging of broadband vibrations via omnipotent tandem triboelectric nanogenerators with cascade impact structure, *Sci. Rep.* **9**, 1–9 (2019)

[137] R. Li, H. Zhang, L. Wang, G. Liu, A contact-mode triboelectric nanogenerator for energy harvesting from marine pipe vibrations, *Sensors* **21**, 1–21 (2021)

[138] H. H. Singh, D. Kumar, N. Khare, A synchronous piezoelectric-triboelectric-electromagnetic hybrid generator for harvesting vibration energy, *Sustain. Energy Fuels* **5**, 212–218 (2021)

[139] L. Liu, Q. Shi, J. S. Ho, C. Lee, Study of thin film blue energy harvester based on triboelectric nanogenerator and seashore IoT applications, *Nano Energy* **66**, 104167 (2019)

[140] H. Yong *et al.*, Highly reliable wind-rolling triboelectric nanogenerator operating in a wide wind speed range, *Sci. Rep.* **6**, 1–11 (2016)

[141] A. Ahmed *et al.*, Farms of triboelectric nanogenerators for harvesting wind energy: A potential approach towards green energy, *Nano Energy* **36**, 21–29 (2017)

[142] M. Prauzek *et al.*, Energy harvesting sources, storage devices and system topologies for environmental wireless sensor networks: A review, *Sensors (Switzerland)* **18** (2018), doi:10.3390/s18082446

[143] B. Kil Yun, H. Soo Kim, Y. Joon Ko, G. Murillo, J. Hoon Jung, Interdigital electrode based triboelectric nanogenerator for effective energy harvesting from water, *Nano Energy* **36**, 233–240 (2017)

[144] S. Chen *et al.*, Self-powered cleaning of air pollution by wind driven triboelectric nanogenerator, *Nano Energy* **14**, 217–225 (2014)

[145] Y. Jiang, X. Liang, T. Jiang, Z. L. Wang, Advances in Triboelectric Nanogenerators for Blue Energy Harvesting and Marine Environmental Monitoring, *Engineering* , 33–36 (2024)

[146] Advanced Energy Materials - 2020 - Jiang - Robust Swing-Structured Triboelectric Nanogenerator for Efficient Blue Energy.pdf

[147] H. Chen, C. Xing, Y. Li, J. Wang, Y. Xu, Triboelectric nanogenerators for a macro-scale blue energy harvesting and self-powered marine environmental monitoring system, *Sustain. Energy Fuels* **4**, 1063–1077 (2020)

[148] Z. L. Wang, T. Jiang, L. Xu, Toward the blue energy dream by triboelectric nanogenerator networks, *Nano Energy* **39**, 9–23 (2017)

[149] C. Xu *et al.*, Contact-electrification between two identical materials: Curvature effect, *ACS Nano* **13**, 2034–2041 (2019)

[150] H. Z. Mengdi Han, Xiaosheng Zhang, *Flexible and Stretchable Triboelectric Nanogenerator Devices: Toward Self-Powered Systems* (Willey, 2019)

[151] Z. Liu *et al.*, Wearable and Implantable Triboelectric Nanogenerators, *Adv. Funct. Mater.* **29**, 1–19 (2019)

[152] K. Rose, S. Eldridge, L. Chapin, The Internet of Things: An Overview Understanding

the Issues and Challenges of a More Connected World, *Internet Soc.* , 80 (2015)

[153] J. Chen *et al.*, Harmonic-resonator-based triboelectric nanogenerator as a sustainable power source and a self-powered active vibration sensor, *Adv. Mater.* **25**, 6094–6099 (2013)

[154] H. Zhang *et al.*, Triboelectric nanogenerator for harvesting vibration energy in full space and as self-powered acceleration sensor, *Adv. Funct. Mater.* **24**, 1401–1407 (2014)

[155] J. Chen, Z. L. Wang, Reviving Vibration Energy Harvesting and Self-Powered Sensing by a Triboelectric Nanogenerator, *Joule* **1**, 480–521 (2017)

[156] J. Zhao *et al.*, Remarkable merits of triboelectric nanogenerator than electromagnetic generator for harvesting small-amplitude mechanical energy, *Nano Energy* **61**, 111–118 (2019)

[157] L. Liu, Q. Shi, Z. Sun, C. Lee, Magnetic-interaction assisted hybridized triboelectric-electromagnetic nanogenerator for advanced human-machine interfaces, *Nano Energy* **86**, 106154 (2021)

[158] Z. Tian *et al.*, Performance-boosted triboelectric textile for harvesting human motion energy, *Nano Energy* **39**, 562–570 (2017)

[159] S. Wang, Y. Xie, S. Niu, L. Lin, Z. L. Wang, Freestanding triboelectric-layer-based nanogenerators for harvesting energy from a moving object or human motion in contact and non-contact modes, *Adv. Mater.* **26**, 2818–2824 (2014)

[160] D. W. Lee *et al.*, Polarization-controlled PVDF-based hybrid nanogenerator for an effective vibrational energy harvesting from human foot, *Nano Energy* **76**, 105066 (2020)

[161] M. He *et al.*, Flexible and stretchable triboelectric nanogenerator fabric for biomechanical energy harvesting and self-powered dual-mode human motion monitoring, *Nano Energy* **86**, 106058 (2021)

[162] Y. Yang *et al.*, Flexible and Extendable Honeycomb-Shaped Triboelectric

Nanogenerator for Effective Human Motion Energy Harvesting and Biomechanical Sensing, *Adv. Mater. Technol.* **7**, 1–9 (2022)

[163] X. Li *et al.*, A Self-Supporting, Conductor-Exposing, Stretchable, Ultrathin, and Recyclable Kirigami-Structured Liquid Metal Paper for Multifunctional E-Skin, *ACS Nano* **16**, 5909–5919 (2022)

[164] J. Luo *et al.*, Rehabilitation of Total Knee Arthroplasty by Integrating Conjoint Isometric Myodynamia and Real-Time Rotation Sensing System, *Adv. Sci.* **9**, 1–10 (2022)

[165] Y. Yang *et al.*, Triboelectric Nanogenerator for Harvesting Wind Energy and as Self- , *ACS Nano* **7**, 9461–9468 (2013)

[166] Y. Xie *et al.*, Rotary triboelectric nanogenerator based on a hybridized mechanism for harvesting wind energy, *ACS Nano* **7**, 7119–7125 (2013)

[167] B. Chen, Y. Yang, Z. L. Wang, Scavenging Wind Energy by Triboelectric Nanogenerators, *Adv. Energy Mater.* **8**, 1–13 (2018)

[168] H. S. Kim *et al.*, Ferroelectric-Polymer-Enabled Contactless Electric Power Generation in Triboelectric Nanogenerators, *Adv. Funct. Mater.* **29**, 1–11 (2019)

[169] D. Y. Kim *et al.*, Floating buoy-based triboelectric nanogenerator for an effective vibrational energy harvesting from irregular and random water waves in wild sea, *Nano Energy* **45**, 247–254 (2018)

[170] S. H. Ju, H. T. Lin, J. Y. Huang, Dominant frequencies of train-induced vibrations, *J. Sound Vib.* **319**, 247–259 (2009)

[171] V. G. Cleante, M. J. Brennan, G. Gatti, D. J. Thompson, Energy harvesting from the vibrations of a passing train: Effect of speed variability, *J. Phys. Conf. Ser.* **744** (2016), doi:10.1088/1742-6596/744/1/012080

[172] G. Yang, B. H. Stark, S. J. Hollis, S. G. Burrow, Challenges for energy harvesting systems under intermittent excitation, *IEEE J. Emerg. Sel. Top. Circuits Syst.* **4**, 364–374 (2014)

[173] M. J. Brennan, G. Gatti, Harvesting Energy from Time-Limited Harmonic Vibrations: Mechanical Considerations, *J. Vib. Acoust. Trans. ASME* **139** (2017), doi:10.1115/1.4036867

[174] Y. Hu *et al.*, A robust hybrid generator for harvesting vehicle suspension vibration energy from random road excitation, *Appl. Energy* **309**, 118506 (2022)

[175] Z. L. Wang, On Maxwell's displacement current for energy and sensors: the origin of nanogenerators, *Mater. Today* **20**, 74–82 (2017)

[176] X. Shen *et al.*, Punching pores on cellulose fiber paper as the spacer of triboelectric nanogenerator for monitoring human motion, *Energy Reports* **6**, 2851–2860 (2020)

[177] M. Zhu *et al.*, 3D spacer fabric based multifunctional triboelectric nanogenerator with great feasibility for mechanized large-scale production, *Nano Energy* **27**, 439–446 (2016)

[178] K. Y. Lee *et al.*, Hydrophobic sponge structure-based triboelectric nanogenerator, *Adv. Mater.* **26**, 5037–5042 (2014)

[179] Y. Lee *et al.*, Cam-based sustainable triboelectric nanogenerators with a resolution-free 3D-printed system, *Nano Energy* **38**, 326–334 (2017)

[180] H. Fang *et al.*, A high performance triboelectric nanogenerator for self-powered non-volatile ferroelectric transistor memory, *Nanoscale* **7**, 17306–17311 (2015)

[181] H. Zhang, Y. Lu, A. Ghaffarinejad, P. Basset, Progressive contact-separate triboelectric nanogenerator based on conductive polyurethane foam regulated with a Bennet doubler conditioning circuit, *Nano Energy* **51**, 10–18 (2018)

[182] W. Zhong, B. Xu, Y. Gao, Engraved pattern spacer triboelectric nanogenerators for mechanical energy harvesting, *Nano Energy* **92**, 106782 (2022)

[183] X. Y. Wei, G. Zhu, Z. L. Wang, Surface-charge engineering for high-performance triboelectric nanogenerator based on identical electrification materials, *Nano Energy* **10**, 83–89 (2014)

[184] A. F. Diaz, R. M. Felix-Navarro, A semi-quantitative tribo-electric series for polymeric materials: The influence of chemical structure and properties, *J. Electrostat.* **62**, 277–290 (2004)

[185] W. Tang, C. Zhang, C. B. Han, Z. L. Wang, Enhancing Output Power of Cylindrical Triboelectric Nanogenerators by Segmentation Design and Multilayer Integration, *Adv. Funct. Mater.* **24**, 6684–6690 (2014)

[186] C. Han, C. Zhang, W. Tang, X. Li, Z. L. Wang, High power triboelectric nanogenerator based on printed circuit board (PCB) technology, *Nano Res.* **8**, 722–730 (2015)

[187] A. Ghaffarinejad *et al.*, Bennet's charge doubler boosting triboelectric kinetic energy harvesters, *J. Phys. Conf. Ser.* **1052** (2018), doi:10.1088/1742-6596/1052/1/012027

[188] J. Nie, X. Chen, Z. L. Wang, Electrically Responsive Materials and Devices Directly Driven by the High Voltage of Triboelectric Nanogenerators, *Adv. Funct. Mater.* **29**, 1–20 (2019)

[189] S. Niu *et al.*, Theoretical study of contact-mode triboelectric nanogenerators as an effective power source, *Energy Environ. Sci.* **6**, 3576–3583 (2013)

[190] H. Peng, X. Sun, W. Weng, X. Fang, *Polymer Materials for Energy and Electronic Applications* (2016)

[191] M. Duque, J. Esteve, G. Murillo, I. D. M. D. B. Imb-cnm, C. Valles, www.enso-ecsel.eu – www.energiot.com – imb-cnm.csic.es, , 8193 (2019)

[192] S. Sharma, R. Kiran, P. Azad, R. Vaish, A review of piezoelectric energy harvesting tiles: Available designs and future perspective, *Energy Convers. Manag.* **254**, 115272 (2022)

[193] M. N. M. Azlin *et al.*, 3D Printing and Shaping Polymers, Composites, and Nanocomposites: A Review, *Polymers (Basel).* **14** (2022), doi:10.3390/polym14010180

[194] N. Shahrubudin, T. C. Lee, R. Ramlan, An overview on 3D printing technology:

Technological, materials, and applications, *Procedia Manuf.* 35, 1286–1296 (2019)

[195] H. Wu *et al.*, Recent developments in polymers/polymer nanocomposites for additive manufacturing, *Prog. Mater. Sci.* 111 (2020), doi:10.1016/j.pmatsci.2020.100638

[196] A. Jandyal, I. Chaturvedi, I. Wazir, A. Raina, M. I. Ul Haq, 3D printing – A review of processes, materials and applications in industry 4.0, *Sustain. Oper. Comput.* 3, 33–42 (2022)

[197] Z. Wu, T. Cheng, Z. L. Wang, Self-powered sensors and systems based on nanogenerators, *Sensors (Switzerland)* 20 (2020), doi:10.3390/s20102925

[198] K. Adamski, J. Adamski, J. A. Dziuban, R. Walczak, in *Inkjet 3D Printed Miniature Water Turbine Energy Harvester-Flow Meter for Distributed Measurement Systems*, (2017), p. 578

[199] M. V. Paranjape, S. A. Graham, H. Patnam, P. Manchi, J. S. Yu, 3D printed bidirectional rotatory hybrid nanogenerator for mechanical energy harvesting, *Nano Energy* 88, 106250 (2021)

[200] N. Han *et al.*, Performance evaluation of 3D printed miniature electromagnetic energy harvesters driven by air flow, *Appl. Energy* 178, 672–680 (2016)

[201] A. Ahmed *et al.*, Additively manufactured nano-mechanical energy harvesting systems: advancements, potential applications, challenges and future perspectives*Nano Converg.* 8 (2021), doi:10.1186/s40580-021-00289-0

[202] J. Bianconi, J. Hallett, J. Pealo, R. Rashidi, in *A Hybrid Piezoelectric and Inductive Rotational Energy Harvester*, (2019), vol. 626

[203] B. Kawa, K. Sliwa, V. C. Lee, Q. Shi, R. Walczak, Inkjet 3D printed MEMS vibrational electromagnetic energy harvester, *Energies* 13, 1–10 (2020)

[204] and A. Z. K. M. A. Parvez Mahmud, Ali Zolfagharian, Saleh Gharaie, Akif Kaynak, Shahjadi Hisan Farjana, Amanda V. Ellis, Jun Chen, 3D-Printed Triboelectric Nanogenerators_ State of the Art, Applications, and Challenges.pdf, 25 (2021)

[205] M. L. Seol *et al.*, All 3D printed energy harvester for autonomous and sustainable resource utilization, *Nano Energy* **52**, 271–278 (2018)

[206] S. Gao *et al.*, Self-power electroreduction of N2 into NH3 by 3D printed triboelectric nanogenerators, *Mater. Today* **28**, 17–24 (2019)

[207] P. Gawron, T. M. Wendt, L. Stiglmeier, N. Hangst, U. B. Himmelsbach, A review on kinetic energy harvesting with focus on 3d printed electromagnetic vibration harvesters*Energies* **14** (2021), doi:10.3390/en14216961

[208] W. Al-Ashtari, M. Hunstig, T. Hemsel, W. Sextro, Analytical determination of characteristic frequencies and equivalent circuit parameters of a piezoelectric bimorph, *J. Intell. Mater. Syst. Struct.* **23**, 15–23 (2012)

[209] T. Eggborn, Analytical Models to Predict Power Harvesting with Piezoelectric Materials, *Masters Thesis, Virginia Polytech. Inst. State Univ. VA Frederick, A. A., Clark, W. W., Hu, H* **5**, 11 (2003)

[210] T. M. Kamel *et al.*, Modeling and characterization of MEMS-based piezoelectric harvesting devices, *J. Micromechanics Microengineering* **20** (2010), doi:10.1088/0960-1317/20/10/105023

[211] A. A. Laghari, K. Wu, R. A. Laghari, M. Ali, A. A. Khan, A Review and State of Art of Internet of Things (IoT), *Arch. Comput. Methods Eng.* **29**, 1395–1413 (2022)

[212] M. A. Jabraeil Jamali, B. Bahrami, A. Heidari, P. Allahverdizadeh, F. Norouzi, *IoT Architecture BT - Towards the Internet of Things: Architectures, Security, and Applications* (2020; https://doi.org/10.1007/978-3-030-18468-1_2)

[213] J. Wang, M. K. Lim, C. Wang, M. L. Tseng, The evolution of the Internet of Things (IoT) over the past 20 years, *Comput. Ind. Eng.* **155**, 107174 (2021)

[214] A. Chatterjee *et al.*, Powering internet-of-things from ambient energy: a review, *JPhys Energy* **5** (2023), doi:10.1088/2515-7655/acb5e6

[215] M. R. Sarker, M. H. M. Saad, J. L. Olazagoitia, J. Vinolas, Review of power converter impact of electromagnetic energy harvesting circuits and devices for autonomous

sensor applications, *Electron.* 10 (2021), doi:10.3390/electronics10091108

[216] P. Carneiro *et al.*, Electromagnetic energy harvesting using magnetic levitation architectures: A review, *Appl. Energy* 260, 114191 (2020)

[217] M. I. | M. M. N. | F. U. K. P. E. A. | Q. C. | A. I. | B. Aissa, Vibration-based piezoelectric, electromagnetic, and hybrid energy harvesters for microsystems applications: A contributed review (2020)

[218] Y. S. Zhihao Yuan, Xu Jin, Ruonan Li, Baocheng Wang, Chengcheng Han, and Z. L. W. Zhiyi Wu, Hybrid Triboelectric-Electromagnetic Magnetic Energy Harvester-Based Sensing for Wireless Monitoring.pdf, *micro nano small* (2022)

[219] X. Jin *et al.*, Triboelectric Nanogenerator Based on a Rotational Magnetic Ball for Harvesting Transmission Line Magnetic Energy, *Adv. Funct. Mater.* 32, 1–7 (2022)

[220] Z. Yuan *et al.*, Magnetic energy harvesting of transmission lines by the swinging triboelectric nanogenerator, *Mater. Today Energy* 22, 100848 (2021)

[221] | A. Y. | C. W. | J. M. | C. F. | P. L., Y. B. | Y. R. | X. W. | H. Y. | M. Rong, Hybrid piezo triboelectric nanogenerator for stray magnetic energy harvesting and self-powered.pdf, *Wiley* (2021)

[222] E. A. Navarro-Camba, J. Segura-García, C. Gomez-Perretta, Exposure to 50 Hz magnetic fields in homes and areas surrounding urban transformer stations in Silla (Spain): Environmental impact assessment, *Sustain.* 10, 1–11 (2018)

[223] F. Abuasbi, A. Lahham, I. R. Abdel-Raziq, Residential exposure to extremely low frequency electric and magnetic fields in the city of Ramallah-Palestine, *Radiat. Prot. Dosimetry* 179, 49–57 (2018)

[224] M. Bonato, E. Chiaramello, M. Parazzini, P. Gajsek, P. Ravazzani, Extremely Low Frequency Electric and Magnetic Fields Exposure: Survey of Recent Findings, *IEEE J. Electromagn. RF Microwaves Med. Biol.* 7, 216–228 (2023)

[225] M. Duque, E. Leon-Salguero, J. Sacristán, J. Esteve, G. Murillo, Towards the Monolithic Integration of Converter Circuitry and Piezoelectric MEMS Energy

Harvesters, *Proceedings* **2**, 1512 (2018)

[226] G. Murillo, H. Campanella, J. Esteve, G. Abadal, Novel optimized design of a piezoelectric energy harvester in a package for low amplitude vibrations, *J. Phys. Conf. Ser.* **476** (2013), doi:10.1088/1742-6596/476/1/012042

[227] L. Fonseca *et al.*, From materials to devices: Bottom-up integration of nanomaterials onto silicon microstructures for thermoelectric and piezoelectric applications, *2017 Spanish Conf. Electron Devices, CDE 2017* , 0–3 (2017)

[228] L. Fonseca *et al.*, SiNERGY, a project on energy harvesting and microstorage empowered by Silicon technologies, *Proc. 2015 10th Spanish Conf. Electron Devices, CDE 2015* , 10–12 (2015)

[229] W. D. Braun *et al.*, Optimized Resonators for Piezoelectric Power Conversion, *IEEE Open J. Power Electron.* **2**, 212–224 (2021)

[230] M. Duque, E. Leon-Salguero, J. Sacristán, J. Esteve, G. Murillo, Optimization of a piezoelectric energy harvester and design of a charge pump converter for CMOS-MEMS monolithic integration, *Sensors (Switzerland)* **19** (2019), doi:10.3390/s19081895

[231] P. Gajšek *et al.*, Review of studies concerning electromagnetic field (EMF) exposure assessment in Europe: Low frequency fields (50 Hz–100 kHz), *Int. J. Environ. Res. Public Health* **13**, 1–14 (2016)

[232] DG TREN/European Commission, ICF Consulting. Overview of the Potential for Undergrounding the Electricity Networks in Europe, 28 February 2003

[233] L. Korpinen, A. Lähdetie, A. Amundin, H. Piippo, L. Sydänheimo, Examples of extremely low-frequency magnetic fields in a Finnish metro station, *Radioprotection* **50**, 229–232 (2015)

[234] H. Jalilian, K. Najafi, M. R. Monazzam, Y. Khosravi, J. Jamali, Occupational Exposure of Train Drivers to Static and Extremely Low Frequency Magnetic Fields in Tehran Subway, *Jundishapur J. Heal. Sci.* **In Press** (2017), doi:10.5812/jjhs.14329

[235] C. Galli, G. Pedrazzi, M. Mattioli-Belmonte, S. Guizzardi, The Use of Pulsed Electromagnetic Fields to Promote Bone Responses to Biomaterials in Vitro and in Vivo, *Int. J. Biomater.* **2018** (2018), doi:10.1155/2018/8935750

[236] S. G. Kim, S. Priya, I. Kanno, Piezoelectric MEMS for energy harvesting, *MRS Bull.* **37**, 1039–1050 (2012)

[237] H. Yu, J. Zhou, L. Deng, Z. Wen, A vibration-based MEMS piezoelectric energy harvester and power conditioning circuit, *Sensors (Switzerland)* **14**, 3323–3341 (2014)

[238] A. Nisanth, K. J. Suja, V. Seena, Design and optimization of MEMS piezoelectric energy harvester for low frequency applications, *Microsyst. Technol.* **27**, 251–261 (2021)

[239] M. Sawane, M. Prasad, MEMS piezoelectric sensor for self-powered devices: A review, *Mater. Sci. Semicond. Process.* **158**, 107324 (2023)

[240] P. P. Deshpande, R. S. Pande, R. M. Patrikar, Fabrication and characterization of zinc oxide piezoelectric MEMS resonator, *Microsyst. Technol.* **26**, 415–423 (2020)

[241] Mark Meschino | Lingyun Wang | Haitong Xu | Rasool Moradi-Dastjerdi Kamran Behdinan, Low-frequency nanocomposite piezoelectric energy harvester with embedded zinc oxide.pdf, *Polym. Compos.* (2021)

[242] K. G. Motora, C. M. Wu, G. M. Rani, W. T. Yen, Effect of ZnO particle size on piezoelectric nanogenerators and mechanical energy harvesting, *Express Polym. Lett.* **16**, 1208–1227 (2022)

[243] X. Lin, J. Kavalakkatt, M. C. Lux-Steiner, A. Ennaoui, Inkjet-Printed Cu2ZnSn(S, Se)4 Solar Cells, *Adv. Sci.* **2**, 2–7 (2015)

[244] G. K. Lau, M. Shrestha, Ink-jet printing of micro-elelectro-mechanical systems (MEMS), *Micromachines* **8**, 1–19 (2017)

[245] A. Cobo, R. Sheybani, E. Meng, MEMS: Enabled Drug Delivery Systems, *Adv. Healthc. Mater.* **4**, 969–982 (2015)

[246] A. Moya, G. Gabriel, R. Villa, F. Javier del Campo, Inkjet-printed electrochemical sensors, *Curr. Opin. Electrochem.* **3**, 29–39 (2017)

[247] G. Murillo, H. Campanella, J. Esteve, G. Abadal, Novel optimized design of a piezoelectric energy harvester in a package for low amplitude vibrations, *J. Phys. Conf. Ser.* **476**, 3–7 (2013)

[248] S. Roundy, P. K. Wright, J. Rabaey, A study of low level vibrations as a power source for wireless sensor nodes, *Comput. Commun.* **26**, 1131–1144 (2003)

[249] G. Murillo, H. Lozano, J. Cases-Utrera, M. Lee, J. Esteve, Improving Morphological Quality and Uniformity of Hydrothermally Grown ZnO Nanowires by Surface Activation of Catalyst Layer, *Nanoscale Res. Lett.* **12**, 4–11 (2017)

[250] G. Murillo, I. Rodríguez-Ruiz, J. Esteve, Selective Area Growth of High-Quality ZnO Nanosheets Assisted by Patternable AlN Seed Layer for Wafer-Level Integration, *Cryst. Growth Des.* **16**, 5059–5066 (2016)

[251] F. Villani *et al.*, Printed ZnO nanoparticle seed layers to grow ZnO nanowires on flexible substrates, , 23 (2023)

[252] R. Tao, M. Mouis, G. Ardila, Unveiling the Influence of Surface Fermi Level Pinning on the Piezoelectric Response of Semiconducting Nanowires, *Adv. Electron. Mater.* **4**, 1–9 (2018)

[253] Y. Hu, L. Lin, Y. Zhang, Z. L. Wang, Replacing a battery by a nanogenerator with 20 v output, *Adv. Mater.* **24**, 110–114 (2012)

[254] R. Hinchet *et al.*, Performance optimization of vertical nanowire-based piezoelectric nanogenerators, *Adv. Funct. Mater.* **24**, 971–977 (2014)

[255] N. Jalali *et al.*, Passivation of zinc oxide nanowires for improved piezoelectric energy harvesting devices, *J. Phys. Conf. Ser.* **476** (2013), doi:10.1088/1742-6596/476/1/012131

[256] C. P. W. Jianwen Xu, High Dielectric Constant SU8 Composite Photoresist for Embedded Capacitors, *J. Appl. Polym. Sci.* (2006), doi:10.1002/app

[257] H. Lozano, G. Catalán, J. Esteve, N. Domingo, G. Murillo, Non-linear nanoscale piezoresponse of single ZnO nanowires affected by piezotronic effect, *Nanotechnology* **32** (2021), doi:10.1088/1361-6528/abb972

[258] A. A. Chlaihawi, S. Emamian, B. B. Narakathu, B. J. Bazuin, M. Z. Atashbar, Novel screen printed and flexible low frequency magneto-electric energy harvester, *Proc. IEEE Sensors* **0**, 13–15 (2016)

[259] J. Song, G. Zhao, B. Li, J. Wang, Design optimization of PVDF-based piezoelectric energy harvesters, *Heliyon* **3** (2017), doi:10.1016/j.heliyon.2017.e00377

[260] J. Fu, Y. Hou, X. Gao, M. Zheng, M. Zhu, Highly durable piezoelectric energy harvester based on a PVDF flexible nanocomposite filled with oriented BaTi2O5 nanorods with high power density, *Nano Energy* **52**, 391–401 (2018)

[261] SilTerra (available at https://www.silterra.com/technology/)